Metasurface antennas for space applications

Mounir Teniou

Université Pierre et Marie Curie

Ecole Doctorale Science Mécanique Acoustique Electronique et Robotique

Laboratoire d'Electronique et Electromagnétisme (L2E)

Metasurface Antennas for Space Applications

Par Mounir Teniou

Thèse de Doctorat en Electronique

Présentée et soutenue publiquement le 27.octobre.2017

Devant un jury composé de :

Pr. Jean-Marc Laheurte	Professeur, Université de Paris-Est Marne-la-valée	Rapporteur
Dr. Jérôme Sokoloff	Maître de Conférences, Université P aul Sabatier	Rapporteur
Pr. Marc Hélier	Professeur, UPMC	Examinateur
Pr. Hélène ROUSSEL	Professeur, UPMC	Directrice de Thèse
Dr. Massimiliano Casaletti	Maître de Conférences, UPMC	Co-Encadrant
Dr. Baptiste Palacin	Résponsable CNES	
Dr. Nicolas Capet	Résponsable CNES	
Dr. Gerard-Pascal Piau	Résponsable Airbus	

Abstract

In this thesis, a method for the implementation of arbitrary aperture field distributions using tensorial metasurfaces is introduced. Sinusoidally modulated metasurfaces are used in order to generate leaky waves with control on both phase and amplitude. The desired aperture phase distribution is obtained using a new local holography formulation. On the other hand, the amplitude distribution is controlled by varying modulation indices and average impedance depending on the position. A separate control of the aperture field components is achieved by modulating the impedance tensor elements independently. The theoretical formulation of the method is presented in details by taking into account the implementation method and antenna adaptation issues. The method is applied to design a wide range of radiation patterns examples both for far-field and near-field applications. The design procedure was first validated with simulations results for a working frequency of 20GHz giving a good agreement with the theoretical results. Several metasurfaces were then manufactured and measured for working frequencies of 10 GHz, 12.25 GHz and 20GHz. The consistency of the measurements and the simulation results proves that a good control of the aperture field phase and amplitude distributions is achieved using the proposed method.

Keywords: Metasurface antenna, leaky-waves, periodic surface, aperture field implementation.

Contents

Contents

List of Tables

List of Figures

Introduction

In recent years, a great interest was given to satellite communication systems as a possible solution to the deployment of high speed agile communication systems and their spreading to non-military applications. This increased the need for low-profile high-performance antennas. In addition, these antennas have to be light, low-cost and easy to manufacture in order to be compatible with mass market production.

In parallel, metamaterials have become an appealing subject of research as they exhibit exotic physical properties that cannot be found in nature such as single or double negative materials [1]-[5]. In the case of 2D structures, the equivalents of metamaterials are called metasurfaces [6]-[26]. They have been used recently in various applications such as frequency selective surfaces [7]-[8], the control surface-wave wave-front [9]-[11], the control of field transmission [12]-[14] and in leaky-wave antennas [15]-[26].

Leaky-wave antennas are based on the propagation properties of surface-waves on sinusoidally modulated metasurfaces. By acting on the modulation parameters, it is possible to control the propagation of the surface waves or to generate radiating modes (leaky-waves) in order to realize antennas [15]-[26].

In previous work, sub-wavelength printed patches over a grounded dielectric slab have been used to implement scalar [16]-[20] and tensor metasurface antennas [22]-[26]. In the scalar case, the direction of the field above the metasurface is dictated by the source [20]. This severely limits the design possibilities. However, a control of the radiated beam polarization, has been achieved in [18]-[20].

Tensor metasurfaces allow higher degrees of freedom for the antenna design, they have been used to generate various types of radiation patterns such as circularly polarized (CP) waves [17],[23] or isoflux shaped beam antennas for space applications [22]-[23]. Recently, metasurface antennas have also been used in order to generate radiation pattern with control over amplitude, phase and polarization [24]-[26].

In this thesis report, we investigate the performances of tensor metasurface antennas as a possible candidate for space applications. We introduce a new approach for the generation of radiating aperture field distributions using modulated tensorial metasurfaces as

a generalization of the solution proposed in [20] for the tensorial case. Our objective is to propose a systematic procedure for the implementation of general aperture field distributions with control of amplitude, phase and polarization [27]-[30]. A separate control of the aperture field components is achieved by modulating the impedance tensor elements independently. A new exact formulation for the first order holography principle is introduced in order to generate the desired aperture phase distribution. On the other hand, the amplitude distribution is controlled using modulation indices and average impedances that vary depending on the position on the metasurface. The proposed method is general and can be applied to any arbitrary aperture field distribution.

This rapport is structured as follows:

Chapter 1- Context and state of the art: In this chapter, the general context if this thesis is presented. In addition, key antennas parameters needed in this study are presented. Finally, an overview of different metasurface examples present in the literature is given.

Chapter 2- Formulation and theoretical background: Theoretical background about scalar and tensor metasurface properties is given. In addition, the formulation of the proposed method is detailed. Our approach is based on a local holographic principle and variable impedance modulation parameters.

Chapter 3- Implementation of the metasurfaces: This chapter gives metasurface implementation considerations such as surface-wave excitation and feeding structure. A step by step algorithm for the implementation of metasurfaces is given, starting from the objective aperture field distribution to the final metasurface structure.

Chapter 4- Numerical Results: In this chapter, numerical results obtained using commercial software are presented. First, the feeding structure parameters are studied in order to obtain the adaptation of the metasurface. Then, examples of metasurface designs with various objective radiation patterns are presented.

Chapter 5- Experimental Results: This chapter gives experimental results obtained from the measurement of manufactured metasurfaces. In addition, constraints related to the manufacturing method (laser etching technique) are presented.

Chapter 6- Conclusions and Prospective: Conclusions and future work are presented

in this chapter.

Chapter 1. Context and state of the art

In this section, we present the context of this PhD thesis and the corresponding state of the art. In order to do that, we develop each term of the thesis title: “Metasurface antennas for space applications”. First, the fundamental parameters used to describe the performance of an antenna are defined. Then, the potential needs to which we try to respond in the space communication systems are introduced. Finally, a state of the art about metasurface antennas is presented.

1.1 Antenna

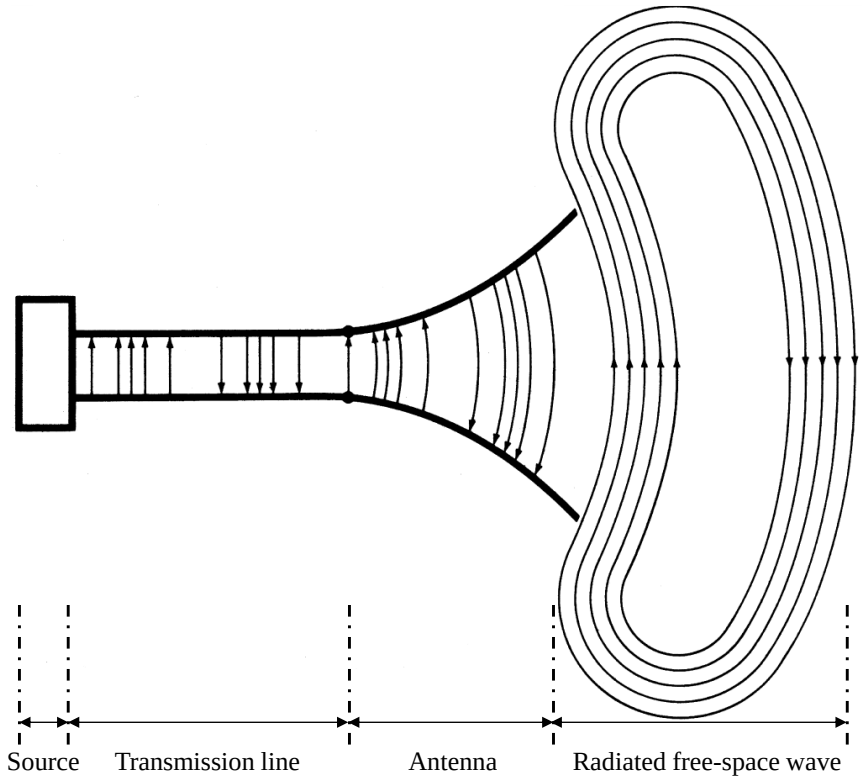

Figure 1: Antenna as a transition device [31].

An antenna is an electrical device that converts electrical power into radiated electromagnetic waves (and vice versa). In other words, the antenna is a transitional structure between free-space and a guiding device as shown in Figure 1 [31].

In order to describe antenna performances, several parameters have been defined. In this section we will present the parameters that are used in this work.

1.1.1 Radiation pattern

The radiation properties of an antenna depend on the distance between the observation point and the antenna. This led to the definition of two main radiation regions. The first region is the *near-field region,* where the angular distribution of the field is dependent upon the distance from the antenna. Then, the *far-field region* is the region where the field angular distribution becomes independent of this distance. In general, the far-field region is considered for distances greater than $2D^2/\lambda$, where D is the largest dimension of the antenna and λ is the wavelength.

An antenna radiation pattern is a graphical representation of the far-field radiation properties of the antenna as a function of space coordinates. It can either represent the intensity of the radiated field, the power density, the directivity, the phase, the polarization or other electromagnetic properties of the radiated field. In general, it is traced in the spherical coordinates and in a logarithmic scale in decibels dB (Figure 2). This logarithmic scale is more used because it accentuates the variations of the radiation pattern in the regions with low values.

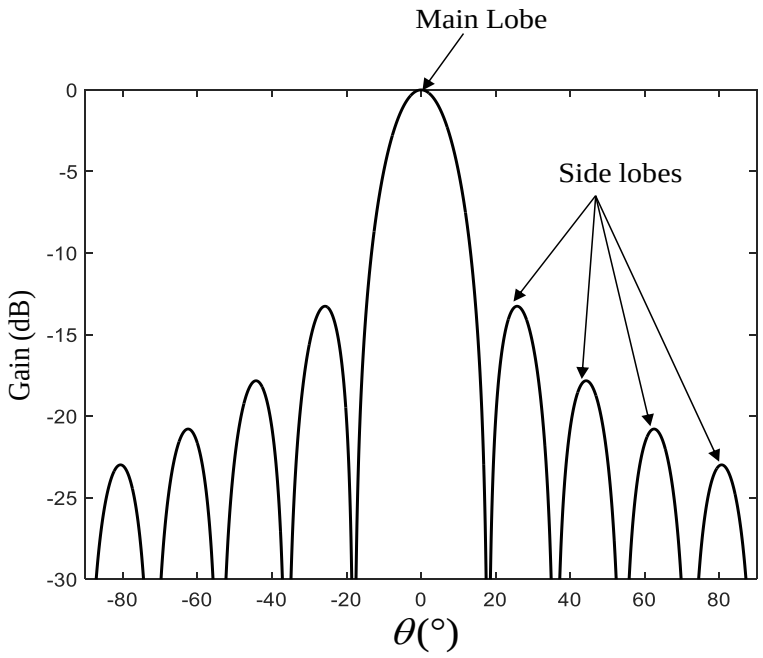

Figure 2: Radiation pattern example in a logarithmic scale.

Local maxima present in an antenna radiation pattern are called lobes. In the case of an antenna designed to radiate in one particular direction, the lobe in that direction is larger than the others and is called the “main lobe”. The remaining lobes are called side lobes. They usually represent radiation in undesired directions and need to be minimized.

1.1.2 Beamwidth

The beamwidth is an antenna parameter related to the radiation pattern. It describes the width of the main lobe in the case of single beam antenna or the width of the desired lobes in the case of multi-beam antenna. The beamwidth is an angular separation between two directions with the same radiation intensity on the opposite sides of the main lobe direction.

There are several definitions of the antenna beamwidth in the literature. The most widely used are

- Half Power Beamwidth (HPBW): It is defined as the angle separating the two directions in which the radiation intensity is equal to half the intensity in the maximum direction.
- First Null Beamwidth (FNBW): It is defined as the angle separating the two directions where there is a first null in the radiation intensity.

Other definitions exist in the literature. However, the term beamwidth usually refers to the Half Power Beamwidth.

The beamwidth is a key parameter of the antenna radiation pattern. It is often used as a trade-off between it and the side lobe level (SLL). In other words, the beamwidth decreases as the side lobe level increases and vice versa [31].

1.1.3 Directivity

The directivity of an antenna is the ratio of the radiation intensity in a given direction to the average radiation intensity in all direction. This average radiation intensity is equal to the total power radiated by the antenna divided by 4π (equation (1)).

$$D = \frac{4\pi U}{P_{rad}} \tag{1}$$

where

D is the directivity

U is the radiation intensity

P_{rad} is the total radiated power

If no direction is specified, the directivity is calculated with respect to the direction of the maximum radiation intensity. The directivity indicates the antenna ability to concentrate power in a desired direction. The bigger is the directivity, the more power is radiated in the maximum direction. It is generally calculated in dB ($D_{dB} = 10\log_{10}(D)$).

For an aperture antenna of surface S_a the directivity is defined as:

$$D = \frac{4\pi}{\lambda^2} \frac{\left| \iint_{S_a} \vec{E}_a \, dS_a \right|^2}{\iint_{S_a} \left| \vec{E}_a \right|^2 dS_a} \tag{2}$$

where

$\vec{E}_a$ is the aperture field distribution.

1.1.4 Gain

Another important antenna parameter is the gain. The gain of an antenna is closely related to the directivity. This parameter describes the losses of the antenna as well as its directional properties (Figure 3). On the other hand, the directivity is only affected by the radiation pattern of the antenna.

The gain is defined as the ratio of the radiation intensity at a certain direction to the radiation intensity obtained if the input power accepted by the antenna was radiated isotropically (equation (3)).

$$G = \frac{4\pi U}{P_{in}} \tag{3}$$

where

P_{in} is the total input power

As in the case of directivity, the direction of maximum radiation is considered when no particular direction is specified.

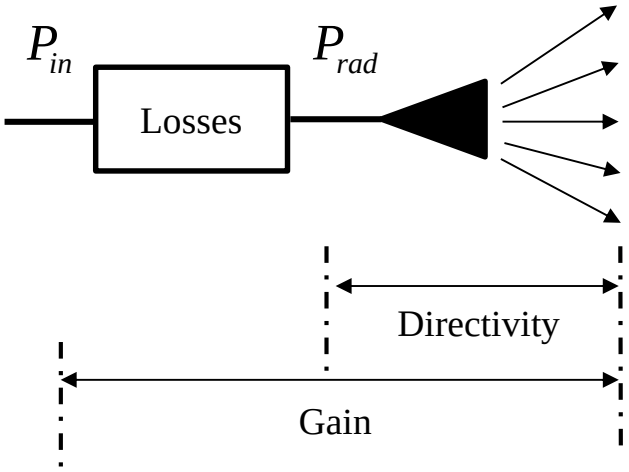

Figure 3: Directivity Vs Gain.

1.1.5 Antenna efficiency

Several efficiencies can be defined for antennas depending on the considered losses. In general, the total efficiency e_0 can be written as [31]:

$$e_0 = e_r e_c e_d \tag{4}$$

where

e_0 is the total efficiency

$e_r = \left(1 - |S_{11}|^2\right)$ is the reflection (mismatch) efficiency

e_c is the conduction efficiency

e_d is the dielectric efficiency

S_{11} is the input port voltage reflection coefficient

The efficiencies e_c and e_d describe the Ohmic losses introduced by the conductors and the dielectric respectively. They are usually determined experimentally but cannot be

separated in general. Thus, they are combined in the radiation efficiency $e_{cd} = e_c e_d$. The latter gives a relation between the gain and the directivity as follows

$$G = e_{cd} D \tag{5}$$

In the case of aperture antennas, an additional important efficiency is defined as follows [31]:

$$e_{ap} = \frac{A_e}{A_p} = \frac{D}{D_u} \tag{6}$$

where

A_p is the physical area of the aperture

A_e is the effective area of the aperture. It corresponds to the area with uniform distribution that gives the same directivity D as the considered aperture.

D_u is the directivity given by an aperture of area A_p with a uniform distribution.

The aperture efficiency is then introduced in the total efficiency, leading to:

$$e_0 = e_r e_{cd} e_{ap} \tag{7}$$

1.1.6 Polarization

The polarization of an antenna in a certain direction is defined as the polarization of the wave transmitted by the antenna [31]. As the variation of the components of the radiated field may vary differently with the direction from the antenna, different parts of the radiation pattern may have different polarizations.

The polarization of electromagnetic waves describes the variation of the direction of the electric-field vector. It can either be linear, circular or elliptical.

Linear polarization: an electromagnetic wave is linearly polarized if the electric field vector is always oriented along the same line. This is accomplished either when the electric field has only one component or two orthogonal linear components that are in time phase or 180° out of phase.

Circular polarization: an electromagnetic wave is circularly polarized if the electric field vector traces a circle as a function of time. This is accomplished when electric field has only two orthogonal linear components, with the same magnitude and that have phase difference that is an odd multiple of 90°. If the rotation of the vector is clockwise (resp counterclockwise), the wave is right-hand (resp left-hand).

Elliptical polarization: an electromagnetic wave is elliptically polarized if the electric field vector traces an ellipse as a function of time. Despite being the general case of electromagnetic wave polarization, it is defined in practice as the case where the polarization of the wave is neither linear nor circular. The same rule as in the circular case is used in order to define the orientation of the elliptical polarization (right-hand or left-hand).

1.1.7 Axial ratio

As stated in the previous subsection, the electric field vector traces an ellipse as a function of time for elliptically polarized antennas. The ratio between the major axis and the minor axis of this ellipse defines the axial ratio of the antenna. The axial ratio is always bigger than one and gives the polarization of an antenna as follows:

- **Linear polarization:** For linearly polarized waves, there is only a major axis in the curve traced by the electric field vector. The minor axis is then equal to 0. As a result, the axial ratio is equal to infinity.
- **Circular polarization:** For circularly polarized waves, the major axis and the minor axis are equal. The axial ratio is then equal to 1 (or 0dB). The more the axial ratio is close to 0dB, the more the polarization is close to a circular polarization.
- **Elliptical polarization:** As in the previous subsection, the elliptical polarization is defined as the case were the polarization is neither linear nor circular. As a result, the polarization is elliptical when the axial ratio is neither equal to 1 (0db) nor to infinity.

1.1.8 Bandwidth

The bandwidth of an antenna is the range of frequencies within which a certain antenna characteristic conforms to some objective performances. As these antenna characteristics doesn’t necessarily have the same frequency dependence, there are multiple charac-

terizations of the bandwidth.

Among the possible definitions of the bandwidth we can distinguish two different groups:

Pattern bandwith: This bandwidth can be defined with respect to several aspects of the radiation pattern of the antenna depending on the application (side lobe level, beam-width, direction of the main lobe, axial ratio …). As an example, we can consider the frequency band where:

- The amplitude of main lobe does not decrease lower than -3dB from its value at the central frequency.
- The axial ratio is smaller than 3dB. This definition is useful for circularly polarized beams.
- The side lobe level is smaller than a certain value (for example -10 or -20dB).
- The radiation characteristics of the antenna are preserved. As for example: an omnidirectional radiation pattern.

It should be noted that there is no clear definition of the pattern bandwidth. Its definition will greatly depend on the needs of the considered application.

Impedance bandwidth: In general case, the impedance bandwidth is defined with respect to the scattering parameter S_{11}. In this case, the bandwidth of the antenna is the region were the S_{11} is smaller than -10dB. This definition is widely used in various antenna applications.

1.2 Antennas for space applications:

Satellite communications and satellite broadcasting have always stimulated antenna development by providing challenging constraints to the researchers. Depending on the applications, several types of performances are expected from satellite antenna systems. For example, one may need an antenna pointing at broadside or with a tilted beam, radiating one beam or multiple beams, with circular or linear polarization or even with a different polarization for each beam.

In recent years, the need for higher speed data links with greatly increased mobility is expanding significantly. This gave interest to the use of Satellite-On-The-Move (SOTM) systems in the Ka frequency band (26.5–40 GHz). SOTM systems are systems able to establish communication with a satellite and maintain it while moving.

These systems need agile beam steering antenna solutions. Among them, the mechanical beam steering solutions are currently the most attractive due to their low cost. However, their large size limits their application to restricted areas such as military systems and large transports.

The need for SOTM systems for the mass market such as plane transportation, trains, or even personal vehicles motivates the need for antenna systems with the following properties:

- Light weight
- Small dimensions
- Low cost
- High performances
- Simplicity of manufacturing

Another challenging problem in satellite communication systems is the radiation of contoured beams. Contoured beams are beams were the radiated power fits a desired coverage that corresponds for example to a country or to a certain territory. In order to obtain this type of radiation patterns, two main approaches involving parabolic reflector antennas are generally used (see Figure 4). A first approach is to produce the shaped contour using a parabolic reflector fed by an array of feeders where each feeder is responsible for a part of the radiated field [32]. Using this type of antennas requires complex feeding networks and may increase the power consumption and the weight of the antenna. The second approach is to shape the surface of the reflector in order to act on the width of the radiated beam to obtain the desired radiation pattern [33]. However, the design of these shaped reflectors can be time-consuming and sometimes very costly. The performances of these methods were further improved in the literature. As an example, the feeder position was optimized in [34]. In [35], a single shaped reflector in conjunction with multiple feeders was used in order to generate a simultaneous contoured and pencil beam. However, the methods are still costly and time consuming.

In general antennas systems for SOTM systems and Contoured beams systems have the following limitations:

- They are bulky and/or heavy.
- They are complex to design and are not suited for a large scale production.
- They are costly (especially for contoured beams systems).

In this work, metasurface antennas performances are investigated as a possible candidate in order to overcome these limitations. Several antennas designs are studied: single beam, multiple beams, beam shaping and near field focusing.

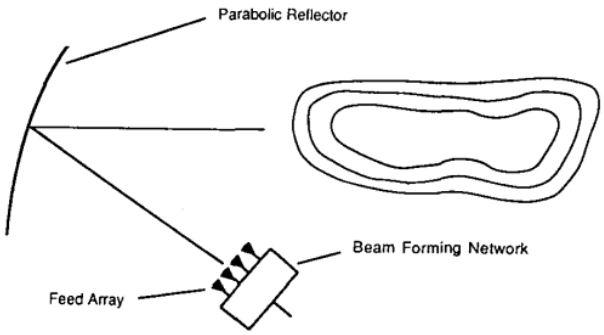

(a)

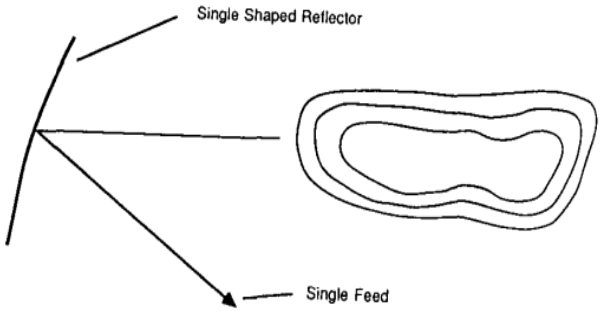

(b)

Figure 4: Contoured beams methods: (a) Using an array of feeders. (b) Using shaped reflectors [33].

1.3 Metasurface antennas

Before introducing metasurfaces, we start by introducing metamaterials. So what are metamaterials?

1.3.1 Metamaterial

The term metamaterial comes from the Greek word *meta* (to go beyond) meaning "to go beyond the material". They consist of materials engineered to have properties that are not found in nature. They are generally composed of repeating patterns with sub-wavelength scale (Figure 5). Their exotic properties come from the arrangement of the repeating pattern (shape, geometry, size, orientation).

Figure 5: Example of a 3D metamaterial structure [36].

Metamaterials can include a lot of different materials depending on the type of the considered exotic property (electromagnetic and optic, mechanic, acoustic…etc). Even if we only consider electromagnetic and optic properties, there is a wide range of material types that fits the definition. As a result, any engineered structure with sub-wavelength dimension that exhibit exotic properties is called metamaterial. As a non-exhaustive list of examples of metamaterials, we can mention:

- **Single Negative Materials (SNG) [1]-[2]:** Materials with negative permittivity (ENG) or negative permeability (MNG).
- **Double Negative Materials (DNG) [3]-[5]:** They are ENG and MNG at the same time. They are materials with negative refractive index (NIM) also called

left-handed metamaterials. As can be seen in Figure 6, a negative refractive index medium bends the light to a negative angle with the surface normal.

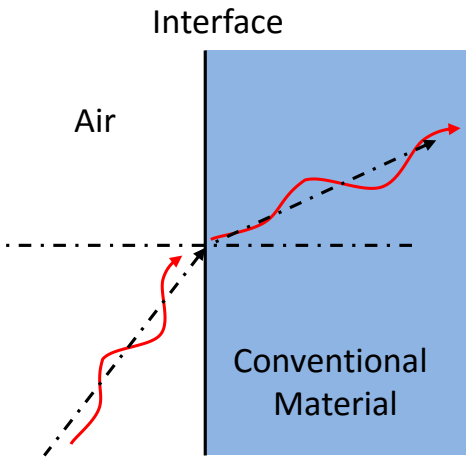

(a)

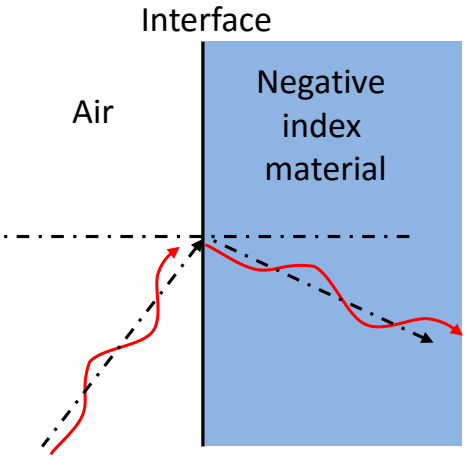

(b)

Figure 6: Comparison of refraction in a left-handed metamaterial with a conventional material.

Two dimensional metamaterials can be realized by arranging electrically small scatterers or holes into a two-dimensional pattern on a surface or interface. These surface versions of metamaterials are called metasurfaces (Figure 7).

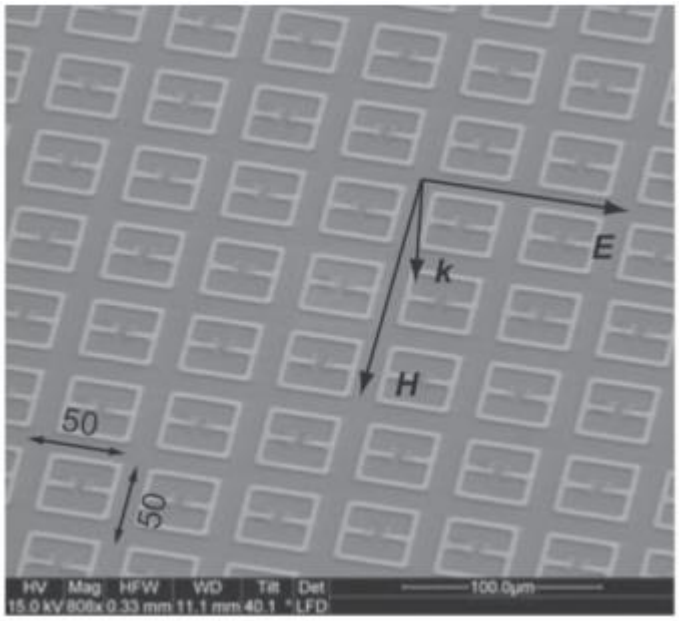

Figure 7: An example of a metasurface consisting of 2D arranged scatterers [6].

1.3.2 Metasurfaces

Metasurfaces are 2D equivalents of metamaterials. As they are 2D structures, this interesting type of metamaterials are thinner than 3D metamaterials. As a result, they offer the possibility of less bulky structures.

As for metamaterials, the word metasurface is not defined clearly, making the term "metasurface" ambiguous. Thus, it can be found in the literature for various types of applications widely discussed in [6]. The article cites papers that use metasurfaces for the achievement of smart antennas, novel wave-guiding structures and absorbers. However, the emphasis of this article focuses on non-modulated metasurfaces which are not the objective of our study.

Metasurfaces offer a lot of possibilities. Among them, we can cite the following classes:

- **Frequency selective surface metamaterials [7]-[8]**
- **Metasurfaces for the control of surface-wave wave-front [9]-[11]**
- **Metasurfaces screens for the control of field transmission [12]-[14]**
- **Metasurfaces for aperture antennas [15]-[26]**

In our work, we are interested in the use of modulated metasurfaces for the design of aperture antennas. This type of metasurfaces is based on leaky wave generation from a surface wave. In what follows, the term “metasurface” will be used to describe this third type only.

1.3.3 Metasurfaces for aperture antennas (Leak-wave antennas)

This type of antennas is based on the use of modulated metasurfaces in order to generate leaky waves. The periodic modulation of metasurfaces produces an infinity of discrete surface wave modes. When the periodicity of the modulation is increased, some of these modes may become propagating. These waves will then propagate away from the metasurface. In [15], Oliner presents a rigorous treatment of propagation on sinusoidally modulated surface impedances. In his paper, the surface under study is a reactance that varies sinusoidally in the direction of propagation. The article discusses the properties of the guided and radiating modes resulting from the impedance modulation. In order to avoid the superposition of multiple radiating modes, the periodicity of the metasurface has to be chosen in order to have only the -1 mode as a propagative mode.

The basic idea of metasurface antenna is then to control the impedance modulation above the metasurface in order to transform a launched surface wave into a local -1 leaky mode able to radiate a desired radiation pattern.

The electromagnetic properties of metasurfaces can be described in terms of surface impedance (analogous to material parameters for volumetric metamaterials). The surface impedance tensor $\underline{\underline{\mathbf{Z}_s}}$ is defined as the ratio of the transverse electric field $\mathbf{E_t}$ and the transverse magnetic field $\mathbf{H_t}$ at the surface S :

$$\mathbf{E_t} = \underline{\underline{\mathbf{Z}_s}}\hat{\mathbf{n}} \times \mathbf{H_t} = \underline{\underline{\mathbf{Z}_s}}\mathbf{J} \tag{8}$$

where

$\hat{\mathbf{n}}$ is the unit vector normal to the surface.

$\mathbf{J} = \hat{\mathbf{n}} \times \mathbf{H_t}$ is the surface current.

In other words, $\underline{\underline{\mathbf{Z}_s}}$ describes the electromagnetic behavior of the complex medium below the surface. It is important to stress the fact that the surface impedance strongly

depends on the considered wave-mode and wavenumber (spatial dispersion). Properties of the impedance tensor are further discussed in the next chapter.

Depending on the nature of $\underline{\underline{\mathbf{Z}}}_s$ (scalar or tensor), metasurface antennas can be divided into two groups: scalar metasurfaces and tensor metasurfaces.

1.3.4 Scalar metasurfaces

Scalar metasurfaces are metasurfaces that have scalar surface impedance. In this case equation (8) reduces to: $\mathbf{E}_t = Z_s \hat{\mathbf{n}} \times \mathbf{H}_t$. The main challenge in this kind of metasurface is the control of the generated leaky wave in order to produce the desired radiation pattern.

In [16], a design procedure of a sinusoidally modulated scalar metasurface is presented. The designed metasurface is used in order to generate a tilted beam radiation pattern. It is implemented using printed metallic strips over dielectric substrate (Figure 8.(a)). Using the relation between the direction of the radiated beam and the modulation periodicity, a metasurface radiating a tilted beam was implemented. The corresponding radiation pattern is represented in Figure.8.(b).

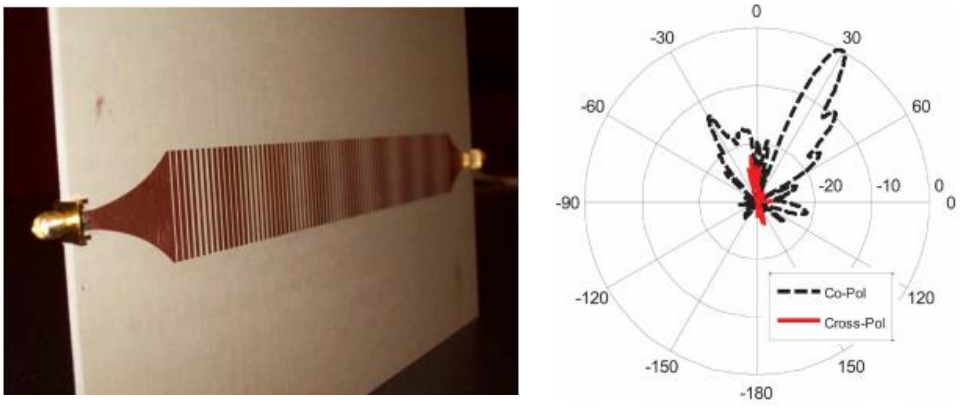

Figure 8: Metasurface antenna designed in [16]. (a) Photograph of fabricated antenna (b) Measured co-polarization and cross-polarization E-plane radiation

Another interesting solution is proposed in [17] to obtain a tilted beam radiation

pattern using scalar metasurfaces. The proposed solution is based on the holography principle. In this approach, an objective phase wave ψ_{obj} and an incident phase wave ψ_{surf} are introduced. The idea is to produce a term proportional to $\psi_{obj}\psi_{surf}^{*}$ so that the interaction between the metasurface and the incident wave produces the objective field distribution (see equation (9)).

$$(\psi_{obj}\psi_{surf}^{*})\psi_{surf} = \psi_{obj}\left|\psi_{surf}\right|^{2} \tag{9}$$

In the case of a tilted beam radiation pattern, the resulting metasurface impedance pattern is shown in figure 9. (a). The metasurface is implemented using metallic patches printed over dielectric substrate. The corresponding radiation pattern is illustrated figure 9. (b). The holographic principal was also extended to tensor case and it will be discussed in the next subsection.

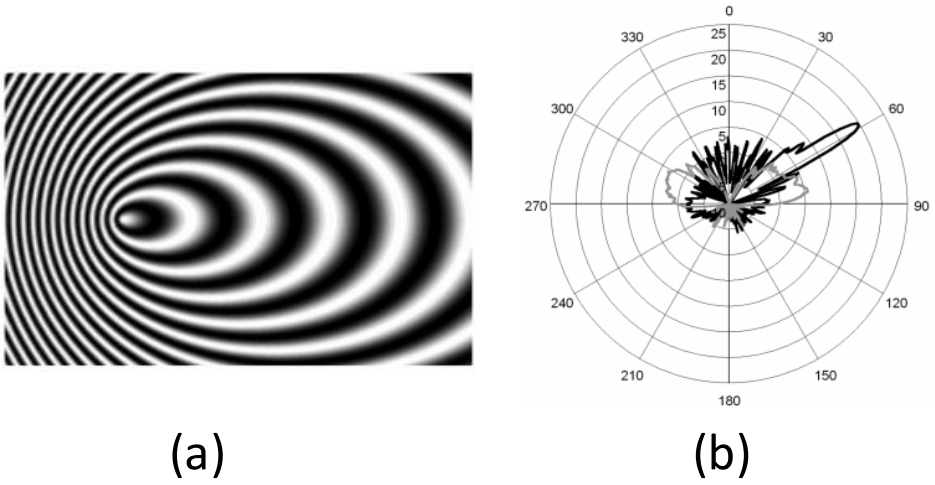

Figure 9: Tilted beam metasurface antenna [17] (a) Scalar impedance pattern formed from holographic interference (b) Measured radiation pattern

The main issue of scalar metasurfaces is the limited control of the radiated leaky wave polarization. The direction of the electric field above the metasurface is defined by the type of excitation used in order to generate the surface wave. It is therfore difficult to generate a circularly polarized beam using this kind of antennas. Some solutions has been proposed in order to overcome this limitation.

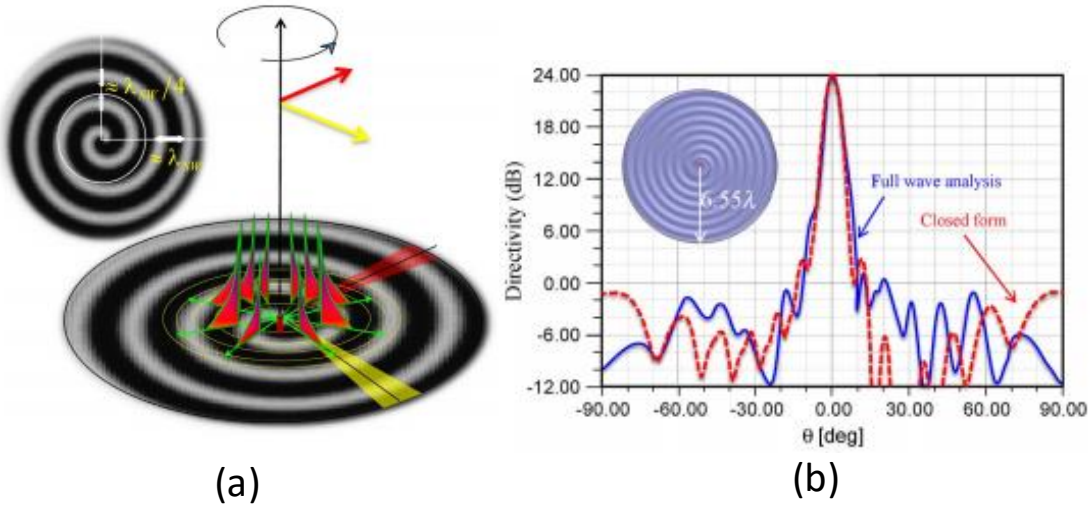

Figure 10: Spiral shaped metasurface antenna [18]. (a) Spiral shape (b) Radiation pattern

A first solution is presented in [18], where a broadside circularly polarized beam is obtained using a two-dimensional spiral shaped metasurface. The spiral shape of the metasurface produces the circular polarization by introducing a phase shift between the different directions of the propagation (Figure.10).

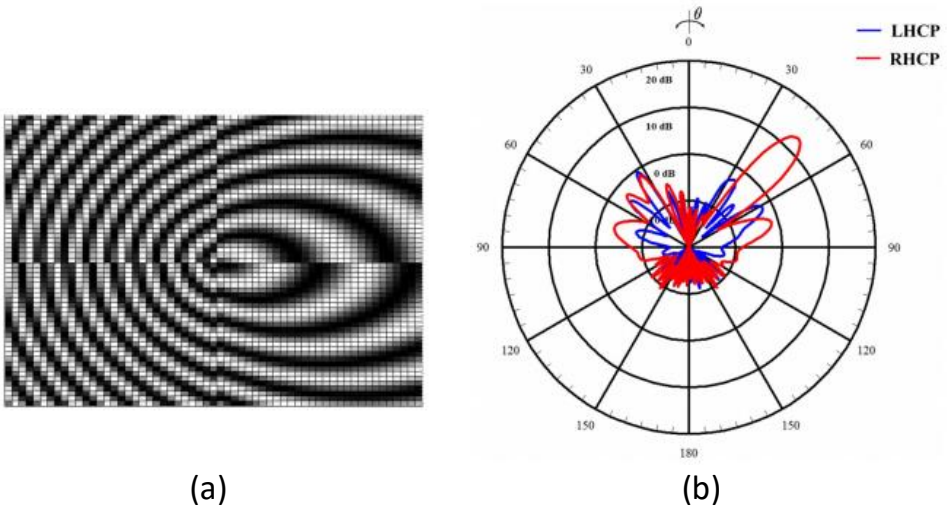

Figure 11: Tilted beam circularly polarized antenna [19]. (a) Modified metasurface to radiate circular polarized waves (b) Radiation pattern

In [19], holographic interference is used in order to generate tilted beam metasurface

antenna. The circular polarization is then obtained by deviding the metasurface into four parts and introducing a 90° phase shift in the impedance variation between each of the parts (Figure.11). A tilted beam with right hand circular polarization is then generated using this technique. A linear polarization is also obtained by dividing the metasurface into two sectors with a 180° phase shift between the two sections.

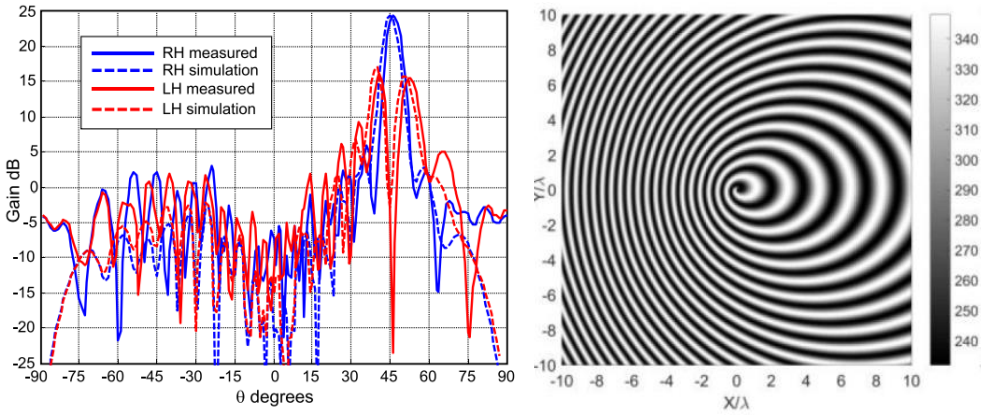

(a) (b)

Figure 12: Tilted beam circularly polarized antenna using scalar metasurface [20]. (a) Structure (b) Radiation pattern.

In [20] a new method for the aperture field generation (instead of beam generation) has been presented by our lab. By controlling the modulation parameters of the surface impedance, the leaky wave mode is used in order to generate a desired aperture field distribution. This aperture distribution can correspond to any objective far-field or near-field radiation pattern. This approach significantly broadens the design possibilities offered by scalar metasurfaces (except for polarization control limitations). A spiral shape is tilted in order to generate a tilted beam with circular polarization as illustrated in figure 12. The advantage of this solution with respect the previous designs is that the whole metasurface participate in the radiation pattern instead of having parts of the metasurface for each polarization component. In addition, using this method, a near-field metasurface antenna radiating a Bessel beam was designed. The designed antenna has a good focusing effect within the non-diffractive region of the Bessel beam.

Another interesting approach for near-field control was introduced in [21]. In this paper, eight mono-directional leaky wave lines are used in order to produce a near-field focus-

ing pattern antenna. The eight lines are disposed symmetrically in order to produce the desired focusing pattern (Figure.13).

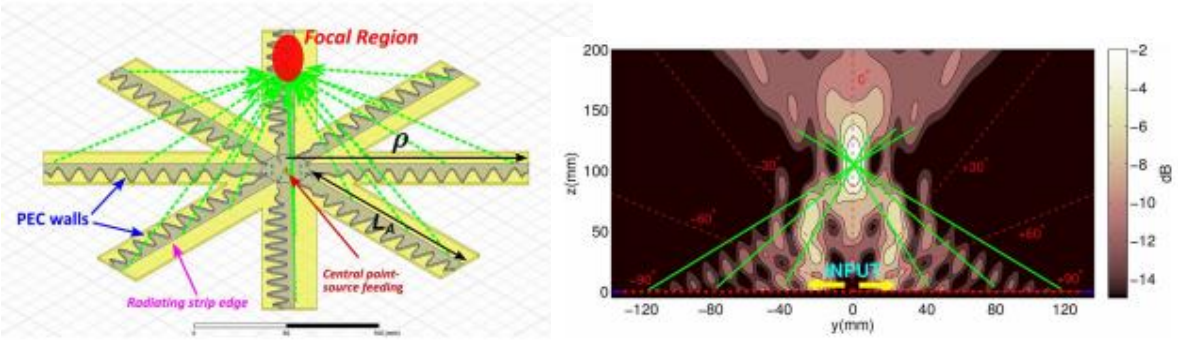

(a) (b)

Figure 13: Near field focusing pattern antenna [21]. (a) Principle (b) Simulated near field.

Scalar metasurfaces offers an interesting range of possibilities and are relatively easy to implement. However, their performances are limited when it comes to polarization control. Moreover, the aperture efficiency is pretty limited (lower than 20%) in this type of metasurfaces [18]-[20]. In addition, some more complex radiation patterns with complex polarization configurations would be difficult and maybe impossible to obtain using this kind of metasurfaces. This motivates the need for investigating tensor metasurfaces. Although this kind of metasurface is more difficult to control and design, they offer a broader set of possibilities. This type of metasurfaces will be discussed in the next subsection.

1.3.5 Tensor metasurfaces

In contrast with scalar metasurfaces, the surface impedance (defined in equation (8)) of this group of metasurfaces is a tensor. The ratio between the tangential electric field and the tangential magnetic field will have four components instead of one. For example if we write the surface impedance tensor $\underline{\underline{\mathbf{Z}_s}}$ in the cylindrical coordinates, we obtain:

$$\underline{\underline{\mathbf{Z}_s}} = \begin{bmatrix} Z_{\rho\rho} & Z_{\rho\phi} \\ Z_{\phi\rho} & Z_{\phi\phi} \end{bmatrix} \tag{10}$$

The possibility of modulating each element of the surface impedance results in an increase of the degrees of freedom of the metasurface design. This significantly widens the possibilities offered by this type of antennas in term of radiation pattern, especially regarding polarization control.

In [17], the holography principle introduced in the previous sub-section is generalized for tensor metasurfaces. The principle is then used in order to design a tilted beam circularly polarized metasurface antenna using sliced gap unit cell topology. Figure.14 Illustrates the obtained metasurface and the measured radiation pattern.

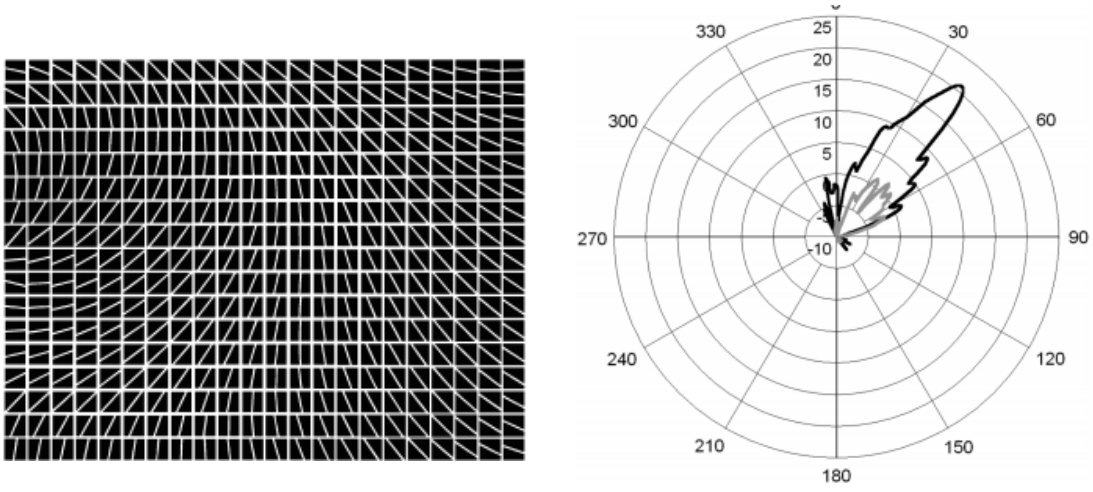

Figure 14: Tilted beam circularly polarized metasurface antenna [17]. (a) A portion of the tensor holographic impedance surface (b) Radiation pattern with the RHCP in black and the LHCP in gray

A circularly polarized isoflux antenna was designed in [22] using tensor metasurfaces. This kind of antenna is wildly used in LEO satellites in order to obtain uniform power density on the ground. The isoflux radiation was successfully obtained using modulated tensor metasurfaces with screw head unit cell topology (Figure.15).

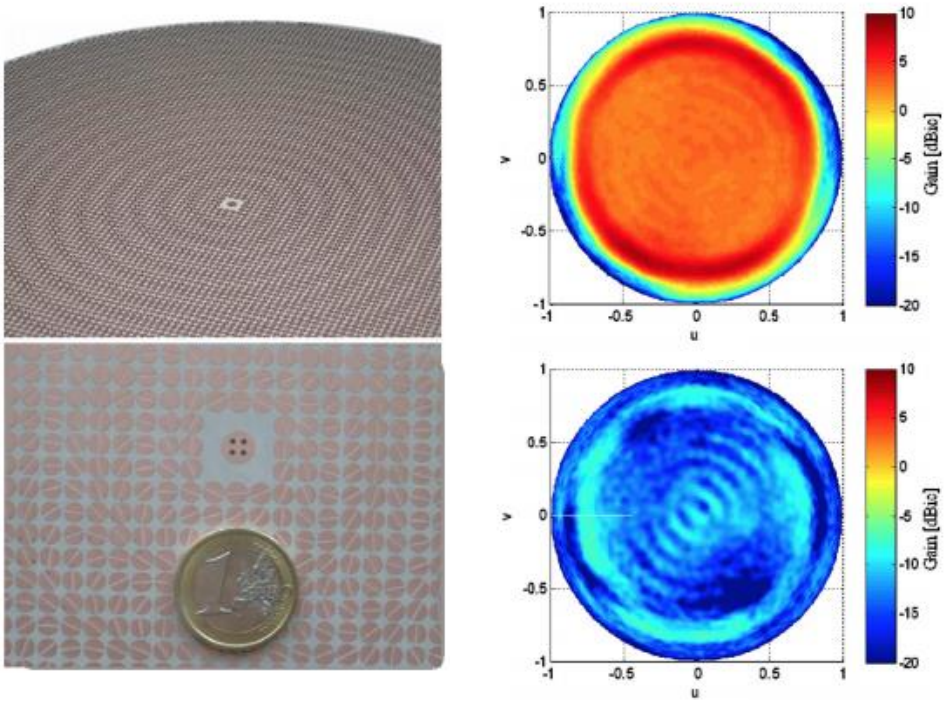

Figure 15: Circularly polarized isoflux antenna [22]. (a) Photograph of the realized prototype. (b) Gain measurements at 8.6 GHz (up: right hand component. down: left hand component).

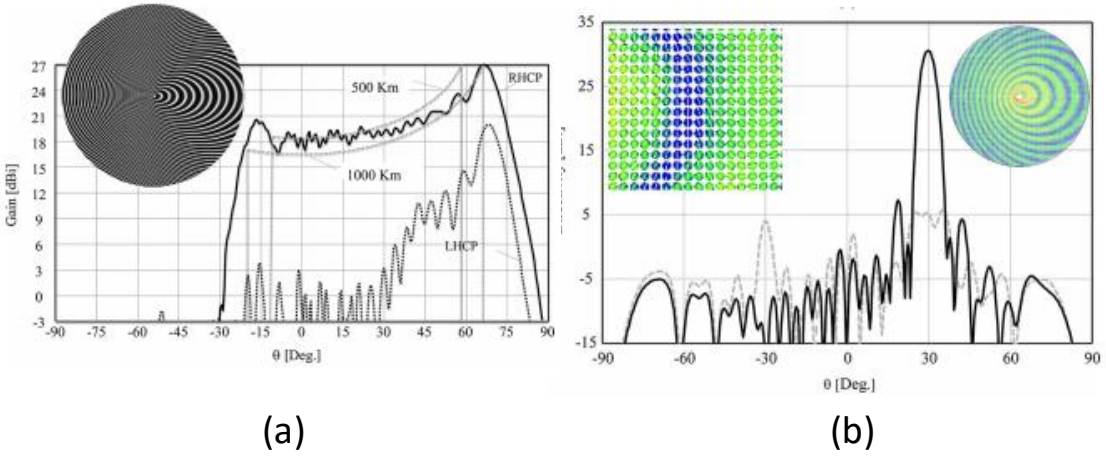

Figure 16: Example of metasurface antenna designs presented in [23]. (a) Sector isoflux antenna (b) Tilted beam circularly polarized antenna.

The same antenna is reintroduced in [23] alongside various tensor metasurfaces antenna designs (broadside CP, tilted beam CP, sector isoflux …etc). Some examples of the achieved radiation patterns are illustrated in Figure.16. The article summarizes the different steps in the design of tensor metasurface antennas and shows some of the designs realized so far.

In some recently published articles [24]-[26], metasurface antennas are used in order to generate radiation pattern with control over amplitude, phase and polarization. In these papers, a modulation index variating in space is used in order to control the leakage parameter of the field over the metasurface. By controlling this leakage parameter and thus the power converted into leaky-wave by the metasurface, a tapering of the amplitude distribution over the metasurface is achieved. This method is used in order to improve the performances of previously designed metasurface by the same group. Figure 17 presents a circularly polarized broadside beam metasurface antenna with a tapered amplitude distribution.

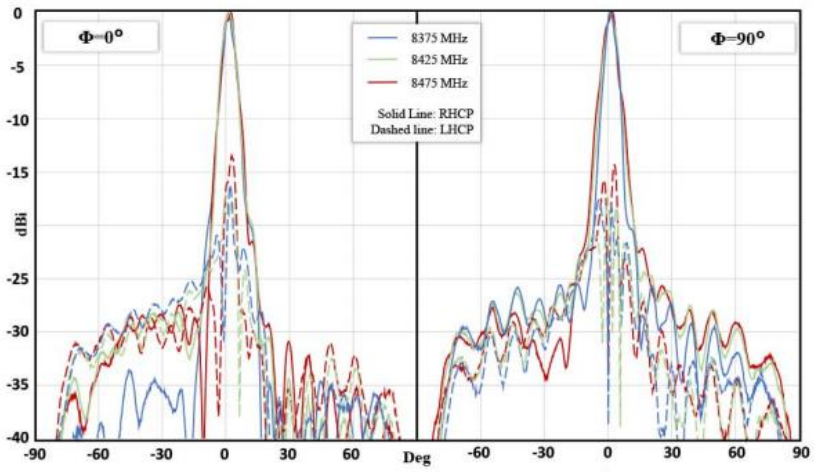

(a) (b)

Figure 17: Radiation pattern measurement of a broadside circularly polarized metasurface antenna with tapered amplitude distribution [26]: (a) $\phi = 0°$ cut-plane (b) $\phi = 90°$ cut-plane.

1.4 Goal of the thesis

The goal of this thesis is to introduce a new approach for the design of tensorial metasurface antennas generalizing the procedure presented in [20] to the tensorial case. In this approach, we focus on the control of the aperture field above the metasurface in order to generate the desired radiation pattern. Using the proposed method, arbitrary aperture distribution can be generated with control on amplitude, phase and polarization. The objectives of this thesis are summarized below:

1- Full control of the generated leaky wave. By treating the general case of a hybrid surface wave excited on the metasurface, the objective is to have an independent control over the generated leaky wave components.
2- Introduce a general approach for the generation of arbitrary aperture field distribution. The objective is to propose a method for generating arbitrary phase and amplitude distribution by acting on the modulation parameters of the impedance tensor.
3- Implementation of the obtained metasurface using printed patches over dielectric substrate. The method is treated for the widely used cylindrical wave excitation case. A design algorithm treating the particularities of the cylindrical excitation case is presented.
4- Validation of the design procedure with numerical simulations. The method is validated for wide range of objective radiation patterns treating the cases of both far-field and near field radiation control. The simulation results are obtained mostly using the commercial software Ansys Designer and compared with the radiation pattern given using ideal aperture distribution as well as equivalent magnetic currents over the metasurface.
5- Validation of the design procedure with measurements. Several prototypes are manufactured and measured for the frequencies of 10GHz, 12.25GHz and 20GHz. Far-field and near-field metasurfaces antennas are designed. Some manufacturing challenges as well as antennas adaptation are treated.

Chapter 2. Formulation and theoretical background

In this section, the leaky wave generation mechanism is presented in the case of scalar and tensorial metasurfaces. In addition, a new method for the generation of aperture field based on the control of leaky waves is introduced. In the presented method, an independent control of the phase and amplitude of each component of the leaky wave aperture field distribution is achieved allowing implementing any arbitrary aperture field distribution.

2.1 Theoretical background

This section presents some theoretical background about leaky wave metasurface antennas. The leaky wave generation mechanism is presented for the scalar case and then extended to the tensor case.

2.1.1 Scalar leaky wave metasurfaces

A surface wave propagating through a scalar metasurface is described by the equation (8) (where the surface impedance $\underline{\underline{\mathbf{Z}}}_{\mathbf{s}}$ is a scalar). Let's consider the case of a mono-directional TM surface wave (SW) propagating along the x direction through reactive surface of impedance $\underline{\underline{\mathbf{Z}}}_{\mathbf{s}} = jX_s$ (Figure 18). The magnetic field above the metasurface has the following form:

$$\mathbf{H_t(x)} = Ie^{jk_t^{sw}x}\hat{\mathbf{y}} \tag{11}$$

where k_t^{sw} is the wavenumber of the propagating surface wave.

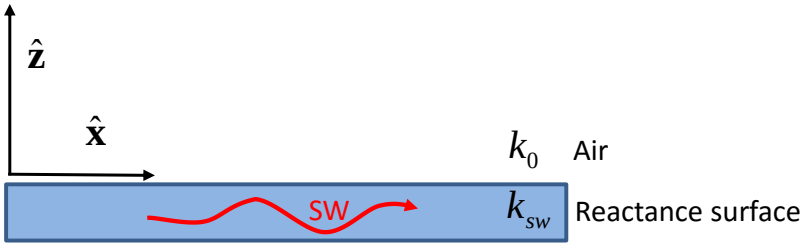

Figure 18: A surface wave propagating through a mono-directional reactance surface.

By defining k_0 as the free-space wavenumber, we can write the z component of the wave vector as

$$k_z^{sw} = \sqrt{k_0^2 - \left(k_t^{sw}\right)^2} \tag{12}$$

In the case of a surface wave, k_t^{sw} is greater than the free-space wavenumber k_0. As a result, k_z^{sw} is purely imaginary and the wave does not propagate in the z direction.

Let's now introduce a sinusoidal modulation of the reactance surface along the propagation direction as described by equation (13) :

$$Z_s(x) = jX_s\left(1 + M\cos\left(\frac{2\pi}{a}x\right)\right) \tag{13}$$

where

X_s is the average reactance.

M is the modulation index.

a is the periodicity of the modulation.

The periodicity of the surface impedance leads to the generation of an infinite number of Floquet modes that propagates through the metasurface [15]. As a result, the electric field and the magnetic field over the metasurface can be expressed in the following form:

$$\begin{cases} \mathbf{H_t(x)} = \sum_{n=-\infty}^{+\infty} I_n e^{jk_{t,n}^{sw}x}\hat{\mathbf{y}} \\ \mathbf{E_t(x)} = \sum_{n=-\infty}^{+\infty} V_n e^{jk_{t,n}^{sw}x}\hat{\mathbf{x}} \end{cases} \tag{14}$$

where

I_n and V_n are the current and voltage modal coefficients of the Floquet's modes.

$k_{t,n}^{sw} = k_{t,0}^{sw} + \frac{n2\pi}{a} \quad n \in \mathbb{Z}$ is the corresponding wavenumber of each mode.

$k_{t,0}^{sw}$ is the wavenumber of the mode 0.

For small values of *M*, the tangential electric field on the metasurface can be approximated at the first order by writing the sinusoidal modulation of equation (13) in the exponential form [20]. This leads to:

$$\mathbf{E_t(x)} = jIX_s\left(e^{jk_t^{sw}x} + \frac{M}{2}e^{j\left(k_t^{sw}-\frac{2\pi}{a}\right)x} + \frac{M}{2}e^{j\left(k_t^{sw}+\frac{2\pi}{a}\right)x}\right)\hat{\mathbf{x}} \tag{15}$$

The tangential electric field is then composed of three modes with different corresponding wavenumbers:

- The mode 0 of wavenumber k_t^{sw}: this mode is surface wave mode because $k_t^{sw} > k_0$.
- The mode +1 of wavenumber $k_t^{sw} + \frac{2\pi}{a}$: this mode is also a surface wave mode because $k_t^{sw} + \frac{2\pi}{a} > k_0$.
- The mode -1 of wavenumber $k_t^{sw} - \frac{2\pi}{a}$: this mode can be a leaky wave mode if $k_t^{sw} - \frac{2\pi}{a} < k_0$.

Figure 19 illustrates the effect of the modulation periodicity on leaky wave generation. It presents the electric field on the half space above the metasurface with respect to the term $k_t^{sw} - \frac{2\pi}{a}$. The figure was obtained by calculating, on a MATLAB code, the total electric field corresponding to the tangential field described by equation (15). It can be seen from the figure that only a surface wave is present when the metasurface is not modulated. By increasing the modulation periodicity, we notice a first case where $k_t^{sw} - \frac{2\pi}{a} = 1.05k_0 > k_0$. In this case, only surface waves are present above the metasurface. The three previously described modes are surface wave modes. When further increasing the modulation periodicity, we notice the appearance of leaky waves propagating away from the metasurface when $k_t^{sw} - \frac{2\pi}{a} < k_0$. In addition, it can be seen that the direction of propagation of the generated leaky wave is affected by periodicity of the impedance modulation.

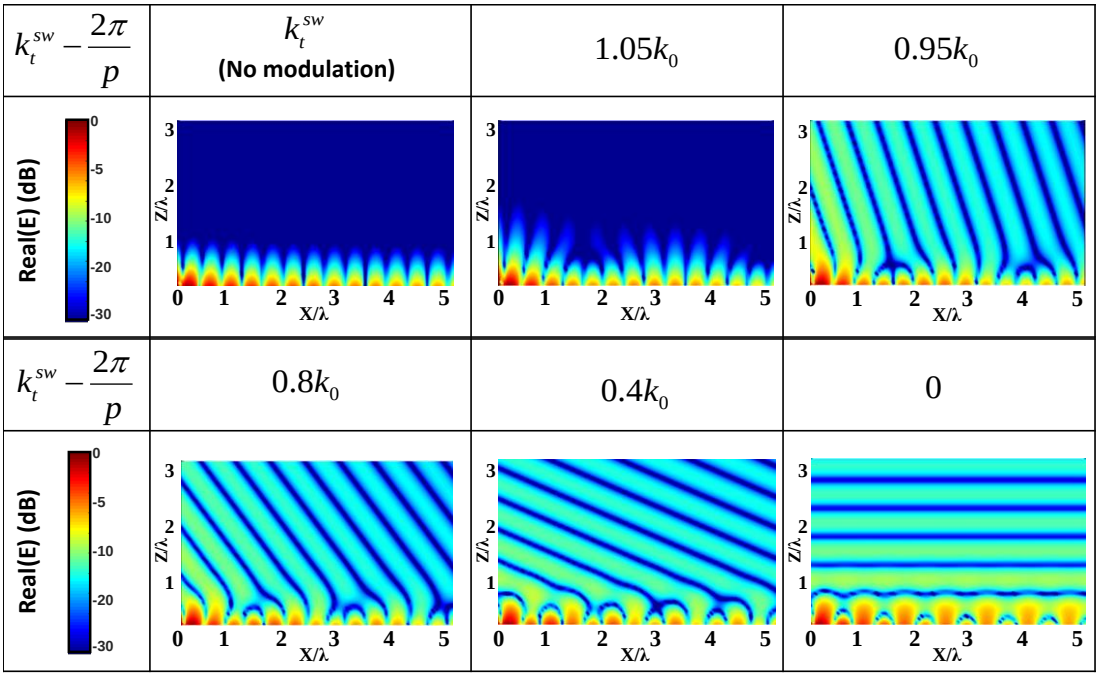

Figure 19: Effect of the modulation periodicity on leaky wave generation at a frequency of 20GHz .

The leaky wave direction of propagation is related to the modulation periodicity by the following equation [16]:

$$\sin(\theta_{-1}) = \frac{k_t^{sw} - \frac{2\pi}{a}}{k_0} \tag{16}$$

where θ_{-1} is the propagation direction of the mode -1.

Using equation (16), the modulation periodicity needed in order to obtain a leaky wave radiating at the direction θ_{-1} can be easily calculated. However, some important points have to be considered in the metasurface design:

- Higher order modes can also be propagating modes if $\left| k_t^{sw} - \frac{n2\pi}{a} \right| < k_0$ for $n < -1$. This aspect has to be checked in order to avoid undesired radiated beams. A possible solution is to use a modulation index M small enough to neglect higher order modes (In our case M<0.5).

- When the metasurface is modulated, the wavenumber of the incident surface wave becomes complex. This latter has been calculated as in [15] and used instead of k_t^{sw} in order to have a more accurate design procedure.

2.1.2 Non-modulated tensorial metasurfaces

Before extending the leaky wave generation principle to the tensorial case, the properties of non-modulated tensorial metasurfaces are presented. In particular, this section discusses the properties of the surface impedance and the propagating modes traveling through the metasurface.

2.1.2.1 Surface impedance tensor

As stated in the previous chapter, the surface impedance of these metasurfaces is described by a tensor. Equation (8) is then written as follows:

$$\mathbf{E}_t\left(\boldsymbol{\rho}'\right)\Big|_{\boldsymbol{\rho}'\in S} = \underline{\underline{\mathbf{Z}_s}}\left(\mathbf{k}^{\mathbf{sw}}\right)\hat{\mathbf{n}}\times\mathbf{H}_t\left(\boldsymbol{\rho}'\right)\Big|_{\boldsymbol{\rho}'\in S} = \underline{\underline{\mathbf{Z}_s}}\mathbf{J}\left(\boldsymbol{\rho}'\right) \tag{17}$$

where

$\boldsymbol{\rho}' = x'\hat{\mathbf{x}} + y'\hat{\mathbf{y}}$ is a point on the antenna surface.

$\hat{\mathbf{n}}$ is a unit vector normal to the surface *S*.

$\mathbf{J}\left(\mathbf{r}\right) = \hat{\mathbf{n}}\times\mathbf{H}_t\left(\mathbf{r}\right)\Big|_{\mathbf{r}\in S}$ is the equivalent surface current.

The impedance $\underline{\underline{\mathbf{Z}_s}}\left(\mathbf{k}^{\mathbf{sw}}\right)$ tensor is defined for a discrete set of wavenumbers, namely:

$$\mathbf{k}^{\mathbf{sw}} = k_t^{sw}\left(n,\omega,\varphi\right)\hat{\mathbf{k}}_t^{sw} = k_t^{sw}\left(n,\omega,\varphi\right)\left(\hat{\mathbf{x}}\cos\left(\varphi\right)+\hat{\mathbf{y}}\sin\left(\varphi\right)\right) \tag{18}$$

where k_t^{sw} is the wavenumber associated with the *n*-th mode propagating along the direction $\hat{\mathbf{k}}_t^{sw}$ defined by the angle φ (Figure 20) at the angular velocity ω.

We will focus our attention on the dominant mode (n=0) propagating on a lossless reciprocal metasurface. For a lossless metasurface, the impedance tensor is anti-Hermitian ($\underline{\underline{\mathbf{Z}_s}}^{\dagger} = -\underline{\underline{\mathbf{Z}_s}}$). If in addition, the metasurface is reciprocal, $\underline{\underline{\mathbf{Z}_s}}$ is a purely imaginary tensor [37].

Thus, on a general 2D orthogonal system, placed on the surface S, equation (17) be-

comes:

$$\begin{bmatrix} E_1 \\ E_2 \end{bmatrix} = j \begin{bmatrix} X_{11} & X_{12} \\ X_{12} & X_{22} \end{bmatrix} \begin{bmatrix} -H_2 \\ H_1 \end{bmatrix} = j \begin{bmatrix} X_{11} & X_{12} \\ X_{12} & X_{22} \end{bmatrix} \begin{bmatrix} J_1 \\ J_2 \end{bmatrix} \tag{19}$$

In what follows, we consider that a surface wave propagating at a direction $\hat{\mathbf{k}}_t^{sw}$ is excited on a metasurface placed in the x-y plane (Figure 20).

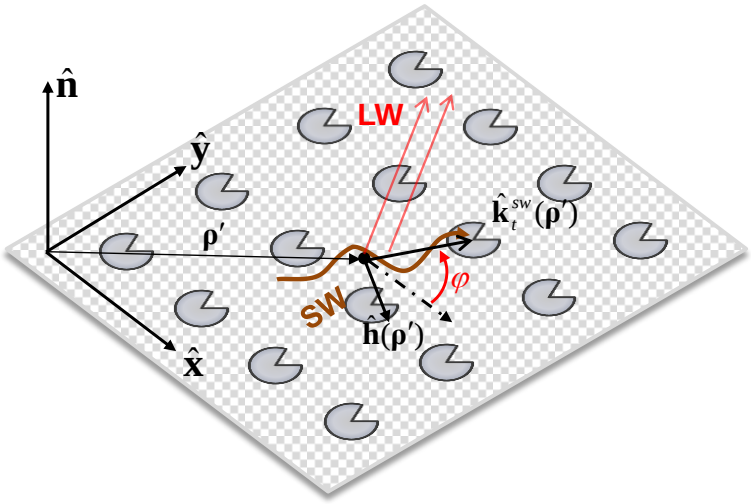

Figure 20: Metasurface geometry and leaky wave generation.

2.1.2.2 Propagating modes

In order to study the surface wave modes propagating on a non-modulated tensorial metasurface, a procedure similar to the one presented in [38] is introduced.

For a tensorial metasurface, the dominant mode is a hybrid EH surface mode. In cylindrical coordinates, it is described by the following equation:

$$\begin{cases} \mathbf{E}_t = \left[V_{TM} \hat{\boldsymbol{\rho}} - V_{TE} \hat{\boldsymbol{\phi}} \right] \mathrm{H}_1^{(2)} \left(k_t^{sw} \rho' \right) \\ \mathbf{H}_t = -\left[I_{TM} \hat{\boldsymbol{\phi}} + I_{TE} \hat{\boldsymbol{\rho}} \right] \mathrm{H}_1^{(2)} \left(k_t^{sw} \rho' \right) \end{cases} \tag{20}$$

where:

V_{TM} , V_{TE} , I_{TM} and I_{TE} are the voltage and current modal coefficients of the surface wave,

$H_1^{(2)}$ is the first order Hankel Function of the second kind.

The wavenumber k_t^{sw} of the surface wave mode can be found using transverse resonance technique as follows:

- The impedance boundary condition (equation (19)) is written between the modal coefficients leading to:

$$\begin{bmatrix} V_{TM} \\ V_{TE} \end{bmatrix} = \underline{\underline{\mathbf{Z}_s}} \begin{bmatrix} I_{TM} \\ I_{TE} \end{bmatrix} = j \begin{bmatrix} X_{mm} & X_{me} \\ X_{me} & X_{ee} \end{bmatrix} \begin{bmatrix} I_{TM} \\ I_{TE} \end{bmatrix} \tag{21}$$

where X_{mm}, X_{me}, X_{ee} are the TM and TE components of the impedance tensor.

- By introducing the quantity Δ defined as:

$$\Delta = \sqrt{\left(\frac{k_t^{sw}}{k_0}\right)^2 - 1} \tag{22}$$

the dyadic free-space impedance is written as :

$$\begin{bmatrix} V_{TM} \\ V_{TE} \end{bmatrix} = \underline{\underline{\mathbf{Z}_0}} \begin{bmatrix} I_{TM} \\ I_{TE} \end{bmatrix} = \begin{bmatrix} -j\zeta_0\Delta & 0 \\ 0 & j\zeta_0/\Delta \end{bmatrix} \begin{bmatrix} I_{TM} \\ I_{TE} \end{bmatrix} \tag{23}$$

where ζ_0 is the free space impedance

- By applying the transverse resonance technique condition ($\det\left[\underline{\underline{\mathbf{Z}_s}} + \underline{\underline{\mathbf{Z}_0}}\right] = 0$) we obtain a second order polynomial equation of unknown Δ:

$$\Delta^2\left(\zeta_0 X_{ee}\right) + \Delta\left(-X_{mm}X_{ee} + \zeta_0^{\,2} + X_{me}^2\right) - X_{mm}\zeta_0 = 0 \tag{24}$$

- Solving the second order polynomial equation leads to the expression of Δ:

$$\Delta = \frac{\left(X_{mm}X_{ee} - \zeta_0^{\,2} - X_{me}^2\right) \pm \sqrt{\left(X_{mm}X_{ee} - \zeta_0^{\,2} - X_{me}^2\right)^2 + 4\zeta_0^{\,2}X_{ee}X_{mm}}}{2\zeta_0 X_{ee}} \tag{25}$$

- The wavenumber k_t^{sw} of the surface wave mode is finally obtained as:

$$k_t^{sw} = k_0\sqrt{\Delta^2 + 1} \tag{26}$$

- For the solution of equation (25), the modal coefficients of equation (20) must satisfy :

$$\begin{cases} I_{TE} = \dfrac{\left(X_{mm} - \zeta_0 \Delta\right)}{X_{me}} I_{TM} \\ I_{TE} = \dfrac{X_{me}}{\left(X_{ee} + \dfrac{\zeta_0}{\Delta}\right)} I_{TM} \end{cases} \tag{27}$$

As for the scalar case, the surface wave wavenumber k_t^{sw} have to be greater than the free-space wavenumber. As a result, the quantity Δ has to be a real positive number. Depending on the values of the impedance tensor components, we can distinguish four cases [38]-[39]:

- Case 1: $X_{mm}X_{ee} > 0$. In this case, equation (24) has two solutions different in sign. That means that a single surface wave type, corresponding to the positive solution of Δ, propagates on the metasurface.
- Case 2: $\left(X_{mm}X_{ee} - \zeta_0^{\,2} - X_{me}^2\right)^2 > -4\zeta_0^{\,2}X_{ee}X_{mm} > 0$. In this case, equation (24) have two solutions with the same sign as X_{ee}. That means that there are either no SW or two SW propagating on the metasurface with different wavenumbers $k_{t,1}^{sw}$ and $k_{t,2}^{sw}$.
- Case 3: $\left(X_{mm}X_{ee} - \zeta_0^{\,2} - X_{me}^2\right)^2 = -4\zeta_0^{\,2}X_{ee}X_{mm}$. After calculations, this condition leads to $X_{me} = 0$ and $X_{mm}X_{ee} = -\zeta_0^{\,2}$. In this case, the term Δ either has no positive solution or a single positive solution corresponding to a TE and a TM surface wave modes, propagating independently with the same wavenumber k_t^{sw}.
- Case 4: $\left(X_{mm}X_{ee} - \zeta_0^{\,2} - X_{me}^2\right)^2 < -4\zeta_0^{\,2}X_{ee}X_{mm}$. In this case, Δ is complex. That does not correspond to any physical surface wave.

In order to have only one surface wave excited on the metasurface, we place ourselves in the first case of study.

2.1.3 Wave-modes generated by modulated tensorial metasurfaces

After studying the surface wave modes propagating on non-modulated tensorial metasurfaces, the leaky wave mechanism that was presented for scalar metasurfaces is extended to the tensorial case.

In this study, we place ourselves in the case of a sinusoidal modulation of each component of the impedance tensor along the direction of propagation of the form:

$$X_{ij}(x) = \bar{X}_{ij}\left[1 + M_{ij}\cos\left(\frac{2\pi}{p_{ij}}x\right)\right] \tag{28}$$

where

X_{ij} is a component of the impedance tensor.

$\bar{X}_{ij}$ is the average impedance of each component.

M_{ij} is the modulation index of each component.

p_{ij} is the periodicity of modulation for each component.

Depending on the values of the individual periodicities p_{ij}, two main cases can be distinguished when introducing the sinusoidal modulation of the impedance components:

- If the periodicities p_{ij} are multiple of the same periodicity p, then the global problem is periodic. The dispersion problem can then be treated using a discrete infinite number of independent transmission lines [39]. For tensorial metasurfaces, lines with different polarizations (TE/TM) are coupled together.
- If the periodicities p_{ij} are different, the global problem is aperiodic. As a result, the dispersion problem cannot be treated using conventional techniques based on Floquet-mode decomposition. In [39], a circuital approach for the analysis of the propagation characteristics of waves guided by scalar or tensorial metasurfaces modulated by functions with discrete spectrum is proposed. This paper presents a solution to the dispersion problem of this case of study (modulation with different periodicities).

As for the scalar case, the infinite number of Floquet-modes can be replaced by a first order approximation of the electric field for small values of the modulation indices M_{ij}. This approximation is obtained by writing the sinusoidal terms of equation (28) in the exponential form and replacing them in (19). As a result, we obtain:

$$\begin{cases} E_1 = j(\bar{X}_{11}J_1+\bar{X}_{12}J_2+\dfrac{M_{11}}{2}\bar{X}_{11}J_1e^{-j\frac{2\pi}{p_{11}}x}+\dfrac{M_{12}}{2}\bar{X}_{12}J_2e^{-j\frac{2\pi}{p_{12}}x} \\ \qquad +\dfrac{M_{11}}{2}\bar{X}_{11}J_1e^{j\frac{2\pi}{p_{11}}x}+\dfrac{M_{12}}{2}\bar{X}_{12}J_2e^{j\frac{2\pi}{p_{12}}x}) \\ E_2 = j(\bar{X}_{12}J_1+\bar{X}_{22}J_2+\dfrac{M_{12}}{2}\bar{X}_{12}J_1e^{-j\frac{2\pi}{p_{12}}x}+\dfrac{M_{22}}{2}\bar{X}_{22}J_2e^{-j\frac{2\pi}{p_{22}}x} \\ \qquad +\dfrac{M_{21}}{2}\bar{X}_{21}J_1e^{j\frac{2\pi}{p_{21}}x}+\dfrac{M_{22}}{2}\bar{X}_{22}J_2e^{j\frac{2\pi}{p_{22}}x}) \end{cases} \tag{29}$$

Each component of the electric field $E_{i,j}$ is composed of six terms depending on the surface current components J_k. These terms can be decomposed into three main groups depending on their corresponding wavenumber:

- Two terms of the form $\bar{X}_{ij}J_k$: these terms correspond to the mode 0 excited on the metasurfaces. They are surface waves of wavenumber $k_t^{sw} > k_0$.
- Two terms of the form $\bar{X}_{ij}J_k e^{j\frac{2\pi}{p_{ij}}x}$: these terms also correspond to surface wave modes of wavenumber $k_t^{sw} + \dfrac{2\pi}{p_{ij}} > k_0$.
- Two terms of the form $\bar{X}_{ij}J_k e^{-j\frac{2\pi}{p_{ij}}x}$: these terms can generate leaky wave modes if the corresponding wavenumber $k_t^{sw} - \dfrac{2\pi}{p_{ij}}$ is smaller than the free-space wavenumber.

In fact, as for scalar metasurfaces, the wavenumber of the mode 0 propagating on a modulated metasurface is different from the one on a non-modulated metasurface. This wavenumber becomes complex and can be obtained using the procedure presented in [39].

If the condition $k_t^{sw} - \dfrac{2\pi}{p_{ij}} < k_0$ is satisfied, a leaky wave is generated above the modulated metasurface. This leaky wave would have the following form:

$$\mathbf{E}_t^{LW} = \begin{bmatrix} E_1^{LW} \\ E_2^{LW} \end{bmatrix} = j \begin{bmatrix} \frac{M_{11}}{2} \bar{X}_{11} J_1 e^{-j\frac{2\pi}{p_{11}}x} + \frac{M_{12}}{2} \bar{X}_{12} J_2 e^{-j\frac{2\pi}{p_{12}}x} \\ \frac{M_{21}}{2} \bar{X}_{21} J_1 e^{-j\frac{2\pi}{p_{21}}x} + \frac{M_{22}}{2} \bar{X}_{22} J_2 e^{-j\frac{2\pi}{p_{22}}x} \end{bmatrix} \tag{30}$$

It should be noted that the components $\bar{X}_{12}$ and $\bar{X}_{21}$ are distinguished in equations (29) and (30). This is done in order to later check the anti-Hermitian property of the proposed formulation.

2.2 Goal of the proposed procedure

In this work, we propose to control the leaky wave described by equation (30) in order to generate an objective aperture distribution of the form:

$$\mathbf{E}_t^{obj} = \begin{bmatrix} E_1^{obj} \\ E_2^{obj} \end{bmatrix} = \begin{bmatrix} \left|E_1^{obj}\right| e^{j\arg(E_1^{obj})} \\ \left|E_2^{obj}\right| e^{j\arg(E_2^{obj})} \end{bmatrix} \tag{31}$$

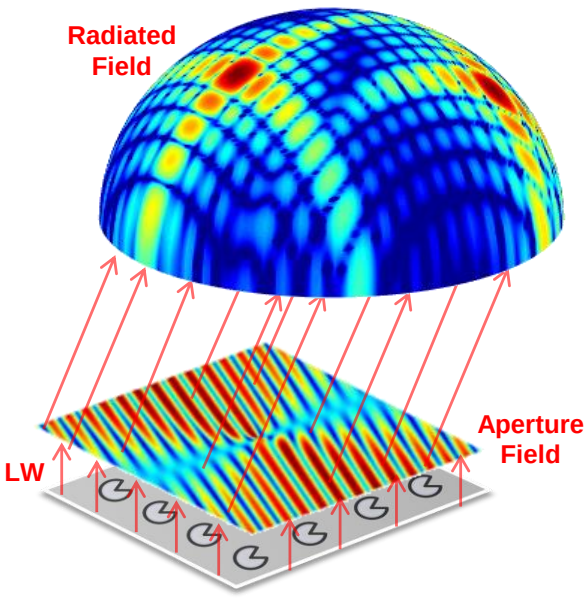

Figure 21: Leaky wave control for aperture field generation.

It can be seen from equation (30) that the phase of the leaky wave is affected by the periodicity of the modulation while the amplitude is controlled by the modulation index and the average impedance.

The working principle of these metasurfaces can then be summarized as follows: “The use of modulated tensorial metasurfaces to generate leaky waves. These leaky waves are then used in order to obtain an objective aperture field giving the desired radiation pattern (Figure 21)”.

2.3 Aperture field generation

The generation of aperture field distribution using modulated tensorial metasurfaces can be decomposed into two main aspects:

- Generation of the phase distribution.
- Generation of the amplitude distribution.

2.3.1 Phase distribution generation

Phase matching between the leaky wave and the objective aperture distribution is obtained using holography principle. This principle is adapted to surface wave to leaky wave conversion. The impedance variation law results from the interaction of the incident wave with the objective aperture field.

In principle, two possible approaches may be considered to obtain the objective phase distribution:

- **First approach:** For each component of the tangential field, equating the phase of each individual term of (30) with the phase of (31).
- **Second approach:** For each component, equating the phase of the sum of the terms of (30) with the phase of (31).

2.3.1.1 First approach

The objective phase distribution is imposed on each term of the generated leaky wave (described by equation (30)). This condition is summarized by the following set of equations:

$$\begin{cases} \arg\left(j\bar{X}_{11} J_1 e^{-j\frac{2\pi}{p_{11}}x} \right) = \arg(E_1^{obj}) \\ \arg\left(j\bar{X}_{12} J_2 e^{-j\frac{2\pi}{p_{12}}x} \right) = \arg(E_1^{obj}) \end{cases} \text{and} \begin{cases} \arg\left(j\bar{X}_{21} J_1 e^{-j\frac{2\pi}{p_{21}}x} \right) = \arg(E_2^{obj}) \\ \arg\left(j\bar{X}_{22} J_2 e^{-j\frac{2\pi}{p_{22}}x} \right) = \arg(E_2^{obj}) \end{cases} \tag{32}$$

These equations lead to the following conditions for the modulation periodicities:

$$\begin{aligned} p_{11} &= \frac{2\pi}{\arg(J_1) + \Pi_{11} - \arg\left(E_1^{obj}\right)}, \; p_{12} = \frac{2\pi}{\arg(J_2) + \Pi_{12} - \arg\left(E_1^{obj}\right)} \\ p_{21} &= \frac{2\pi}{\arg(J_1) + \Pi_{21} - \arg\left(E_2^{obj}\right)}, \; p_{22} = \frac{2\pi}{\arg(J_2) + \Pi_{22} - \arg\left(E_2^{obj}\right)} \end{aligned} \tag{33}$$

where

$$\Pi_{ij} = \pi\left(\operatorname{sgn}\left(\bar{X}_{ij}\right) - 1\right)/2 \quad \text{and} \quad \Pi_{12} = \Pi_{21}.$$

By defining the incident vector phase wave $\boldsymbol{\Psi}_{inc}$ as the phase of the current $\mathbf{J}$ and the objective vector phase wave $\boldsymbol{\Psi}_{obj}$ as the phase terms of the objective electric field (31) , we obtain:

$$\boldsymbol{\Psi}_{inc} = \begin{bmatrix} \Psi_1^{inc} \\ \Psi_2^{inc} \end{bmatrix} = \begin{bmatrix} e^{j\arg(J_1)} \\ e^{j\arg(J_2)} \end{bmatrix}, \; \boldsymbol{\Psi}_{obj} = \begin{bmatrix} \Psi_1^{obj} \\ \Psi_2^{obj} \end{bmatrix} = \begin{bmatrix} e^{j\arg(E_1^{obj})} \\ e^{j\arg(E_2^{obj})} \end{bmatrix} \tag{34}$$

If all of the average impedances $\bar{X}_{ij}$ have the same sign, the set of equations (33) can be written as follows:

$$\begin{aligned} je^{-j\frac{2\pi}{p_{11}}x} &= \Psi_1^{obj}\Psi_1^{inc*}, \; je^{-j\frac{2\pi}{p_{12}}x} = \Psi_1^{obj}\Psi_2^{inc*} \\ je^{-j\frac{2\pi}{p_{21}}x} &= \Psi_2^{obj}\Psi_1^{inc*}, \; je^{-j\frac{2\pi}{p_{11}}x} = \Psi_2^{obj}\Psi_2^{inc*} \end{aligned} \tag{35}$$

By replacing the imaginary parts of (35) in (28), the impedance tensor $\underline{\underline{\mathbf{Z}_s}}$ can be cast in the following compact form:

$$\begin{aligned}\underline{\underline{\mathbf{Z_s}}} &= j\begin{bmatrix}\bar{X}_{11} & \bar{X}_{12}\\ \bar{X}_{21} & \bar{X}_{22}\end{bmatrix} + j\begin{bmatrix}\bar{X}_{11}\,\mathrm{Im}\left(\Psi_1^{obj}\Psi_1^{inc*}\right) & \bar{X}_{12}\,\mathrm{Im}\left(\Psi_1^{obj}\Psi_2^{inc*}\right)\\ \bar{X}_{21}\,\mathrm{Im}\left(\Psi_2^{obj}\Psi_1^{inc*}\right) & \bar{X}_{22}\,\mathrm{Im}\left(\Psi_2^{obj}\Psi_2^{inc*}\right)\end{bmatrix}\\ &= j\underline{\underline{\mathbf{X}}} + j\underline{\underline{\mathbf{X}}}\circ\underline{\underline{\mathbf{M}}}\,\Im\left(\Psi_{obj}\otimes\Psi_{inc}^{*}\right)\end{aligned} \tag{36}$$

where

$\underline{\underline{\mathbf{X}}}$ is the average reactance tensor,

$\underline{\underline{\mathbf{M}}}$ is the modulation index matrice,

$\otimes$ and $\circ$ are the outer and the Hadamard products respectively.

As stated in a previous sub-section, the impedance tensor $\underline{\underline{\mathbf{Z_s}}}$ is anti-Hermitian (equation (19)). Equation (36) does not guarantee that as the off diagonal terms depends on field components that cannot be controlled at priory (incident field and objective field). A possible solution is to decompose the impedance tensor into the Hermitian part $\underline{\underline{\mathbf{H}}}$ and the anti-Hermiatian one $\underline{\underline{\mathbf{A}}}$ defined by:

$$\underline{\underline{\mathbf{H}}} = \frac{\underline{\underline{\mathbf{Z_s}}} + \underline{\underline{\mathbf{Z}}}_s^{\dagger}}{2}, \qquad \underline{\underline{\mathbf{A}}} = \frac{\underline{\underline{\mathbf{Z_s}}} - \underline{\underline{\mathbf{Z}}}_s^{\dagger}}{2} \tag{37}$$

and then use $\underline{\underline{\mathbf{A}}}$ as the impedance tensor. This solution leads to the formulation presented in [17]. However, this technique neglect a significant part of the impedance tensor (Hermitian-part) that guarantee the exact objective phase distribution.

2.3.1.2 Second approach

The objective phase distribution is now imposed on the sum of the terms of the leaky wave. This can be summarized as follows:

$$\begin{cases}\arg\left(j\dfrac{M_{11}}{2}\bar{X}_{11}J_1 e^{-j\frac{2\pi}{p_{11}}x} + j\dfrac{M_{12}}{2}\bar{X}_{12}J_2 e^{-j\frac{2\pi}{p_{12}}x}\right) = \arg(E_1^{obj})\\ \arg\left(j\dfrac{M_{21}}{2}\bar{X}_{21}J_1 e^{-j\frac{2\pi}{p_{21}}x} + j\dfrac{M_{22}}{2}\bar{X}_{22}J_2 e^{-j\frac{2\pi}{p_{22}}x}\right) = \arg(E_2^{obj})\end{cases} \tag{38}$$

It can be seen from equation (38) that obtaining the desired phase distribution is not a trivial task as a significant number of elements needs to be controlled simultaneously.

For example, if we consider the first component of the objective field E_1^{obj}, one must control the average impedances $\left(\bar{X}_{11}, \bar{X}_{12}\right)$, the modulation indices $\left(M_{11}, M_{12}\right)$ and the periodicities $\left(p_{11}, p_{12}\right)$ in order to obtain the desired phase distribution. Moreover, an anti-Hermitian impedance tensor can then be obtained by imposing that $\bar{X}_{12} = \bar{X}_{21}$ without neglecting terms of the impedance tensor.

In this work, this approach is adopted as no impedance term is neglected. To simplify the calculations a new local framework formulation is introduced. To the best of our knowledge, no work has been published on this important aspect. This completely novel formulation is described in the next section.

2.3.1.3 Local framework formulation

In this approach, we take advantage of the fact that physical properties (energy conservation and reciprocity) are conserved under orthogonal transformations. At each point of the metasurface we define a local framework such that the magnetic field $\mathbf{H}_t\left(\boldsymbol{\rho}'\right)$ is directed along a local axis (Figure 22).

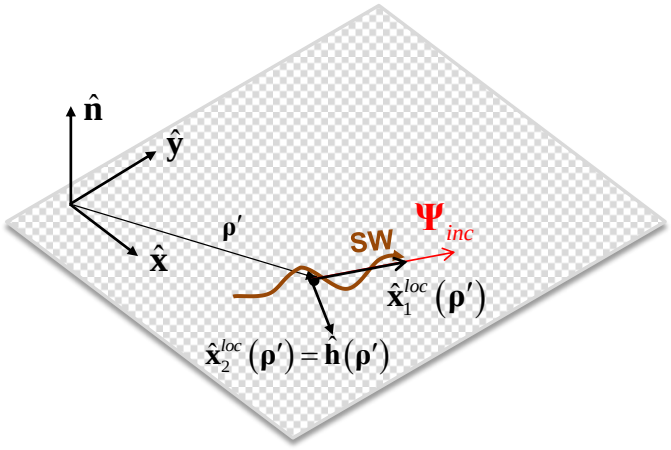

Figure 22: Local framework definition at each point of the metasurface.

Such a local orthogonal reference system can be defined as

$$\begin{aligned} \hat{\mathbf{x}}_2^{loc}\left(\boldsymbol{\rho}'\right) &= \hat{\mathbf{h}}\left(\boldsymbol{\rho}'\right) \\ \hat{\mathbf{x}}_1^{loc}\left(\boldsymbol{\rho}'\right) &= \hat{\mathbf{x}}_2^{loc}\left(\boldsymbol{\rho}'\right) \times \hat{\mathbf{n}} \end{aligned} \tag{39}$$

Thus, by defining at each point of the metasurface the transformation matrix $\underline{\underline{\mathbf{R}}}(\boldsymbol{\rho}')$ between the global framework and the local framework, the relation between local and global quantities can be written as

$$\begin{aligned}
\mathbf{E}_t^{loc}(\boldsymbol{\rho}') &= \underline{\underline{\mathbf{R}}}(\boldsymbol{\rho}') \cdot \mathbf{E}_t(\boldsymbol{\rho}') \\
\mathbf{H}_t^{loc}(\boldsymbol{\rho}') &= \underline{\underline{\mathbf{R}}}(\boldsymbol{\rho}') \cdot \mathbf{H}_t(\boldsymbol{\rho}') \\
\underline{\underline{\mathbf{Z}}}_s^{loc}(\boldsymbol{\rho}') &= \underline{\underline{\mathbf{R}}}(\boldsymbol{\rho}') \cdot \underline{\underline{\mathbf{Z}}}_s(\boldsymbol{\rho}') \cdot \underline{\underline{\mathbf{R}}}(\boldsymbol{\rho}')^{-1}
\end{aligned} \tag{40}$$

In equation (40) and what follows, the superscript *loc* indicates that the considered quantity is written in the local framework. In this local framework, equation (19) simplifies as :

$$\begin{bmatrix} E_1^{loc} \\ E_2^{loc} \end{bmatrix} = j \begin{bmatrix} X_{11}^{loc} & X_{12}^{loc} \\ X_{21}^{loc} & X_{22}^{loc} \end{bmatrix} \begin{bmatrix} -H_2^{loc} \\ 0 \end{bmatrix} = j \begin{bmatrix} X_{11}^{loc} & X_{12}^{loc} \\ X_{21}^{loc} & X_{22}^{loc} \end{bmatrix} \begin{bmatrix} J_1^{loc} \\ 0 \end{bmatrix} \tag{41}$$

It can be seen from equation (41) that only the first column of $\underline{\underline{\mathbf{Z}}}_s^{loc}$ affects the local electric field. The second approach described by equation (38) reduces to the use of the holographic principle on the first collumn of the local impedance tensor. This yields:

$$\begin{cases} X_{11}^{loc} = \bar{X}_{11}^{loc} \left[1 + M_{11}^{loc} \Im\left(\Psi_{obj,1}^{loc} \cdot \Psi_{obj,1}^{loc*} \right) \right] \\ X_{21}^{loc} = \bar{X}_{21}^{loc} \left[1 + M_{21}^{loc} \Im\left(\Psi_{obj,2}^{loc} \cdot \Psi_{obj,1}^{loc*} \right) \right] \end{cases} \tag{42}$$

The anti-Hermitian property of the impedance tensor is then guaranteed by imposing $X_{12}^{loc} = X_{21}^{loc}$ as this component does not affect the electric field. In addition, X_{22}^{loc} is a free quantity that can be used for other design purposes. However, as the surface wave wavenumber k_t^{sw} depends on the impedance components, X_{22}^{loc} can not be selected arbitrarily.

Finally, the impedance tensor that allows an exact phase match between the leaky wave and the objective wave is written in the global framework as follows:

$$\underline{\underline{\mathbf{Z}}}_{\mathbf{s}}(\boldsymbol{\rho}') = \underline{\underline{\mathbf{R}}}(\boldsymbol{\rho}') \, j \begin{bmatrix} X_{11}^{loc}(\boldsymbol{\rho}') & X_{21}^{loc}(\boldsymbol{\rho}') \\ X_{21}^{loc}(\boldsymbol{\rho}') & X_{22}^{loc}(\boldsymbol{\rho}') \end{bmatrix} \underline{\underline{\mathbf{R}}}(\boldsymbol{\rho}')^{-1} \tag{43}$$

Figure 23 presents an example of the generation of an objective phase distribution. The figure illustrate for one component, the incident wave (Figure 23.(a)), the objective wave (Figure 23.(b)) and the corresponding impedance variation obtained using equation (43) (Figure 23.(c)). Then, figure 23.(d) presents the phase of the generated leaky wave. It can be seen from the figure that the phase of the generated leaky wave corresponds to the objective phase distribution.

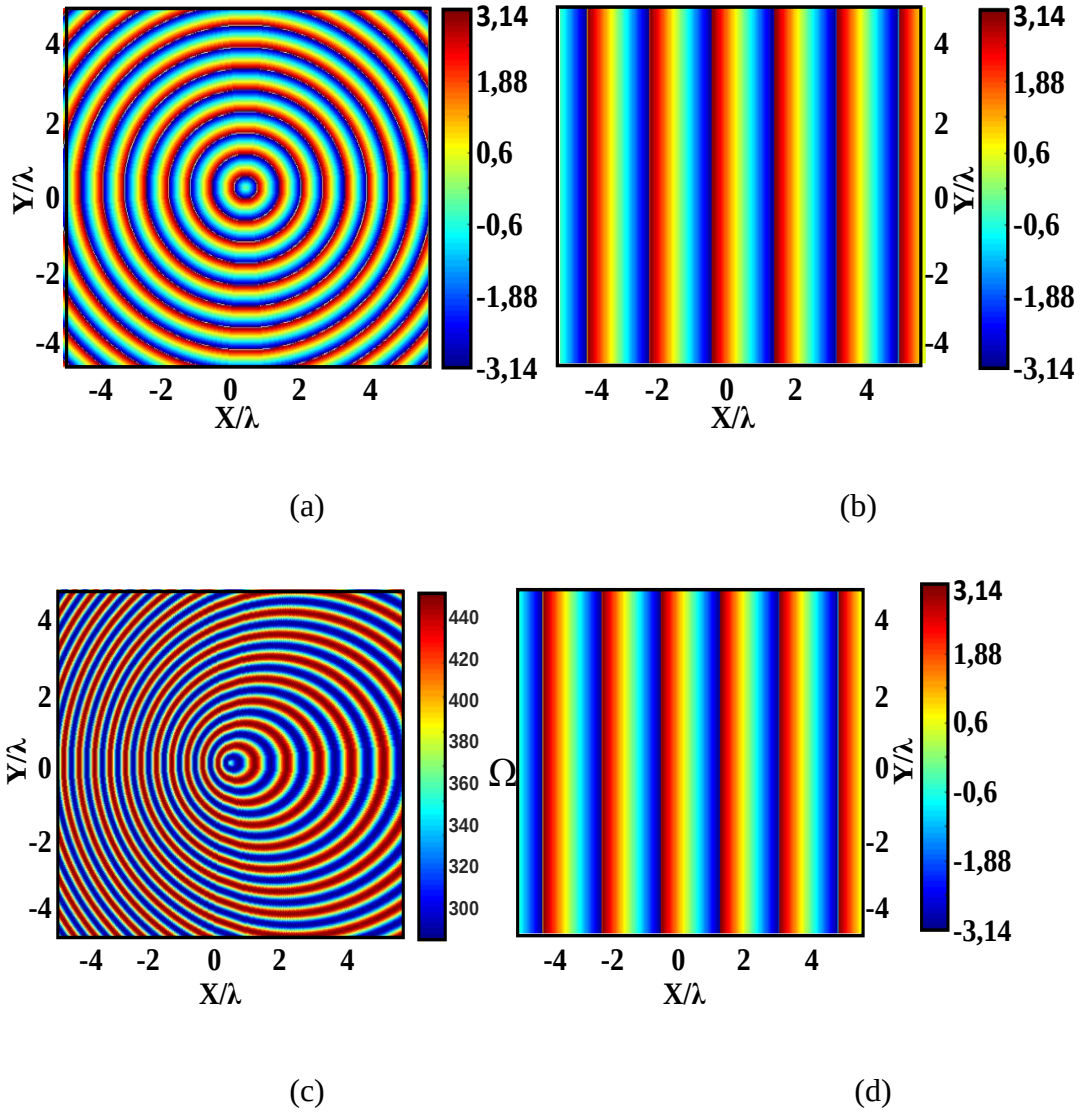

Figure 23: Example of a phase distribution generation (one component). (a) Phase of the incident wave (in rad). (b) Phase of the objective field (in rad). (c) Corresponding impedance distribution obtained using equation (43) (in Ω). (d) Phase of the generated leaky wave (in rad).

2.3.2 Amplitude distribution generation

As explained in the previous sub-sections, the first order approximation of the amplitude of the generated leaky wave is proportional to the product $\bar{X}_{ij}M_{ij}$. Thus, the idea is to change the average impedance and the modulation index along the metasurface in order to obtain the desired amplitude distribution above the metasurface. This amplitude control includes two aspects :

- The compensation of the spreading factor of the surface wave.
- The generation of the desired amplitude distribution.

It should be noted that the proposed amplitude generation technique is developed in the local framework that was developed in the previous sub-section. We decompose the procedure into two steps :

2.3.2.1 Step 1: Compensation of the surface wave spreading factor

The primary step of the amplitude control is the compensation of the attenuation due to the propagation of the surface wave on the metasurface. The first objective is then to obtain uniform amplitude of the generated leaky wave.

This objective is achieved using a modulation index and average impedance that vary depending on the position on the metasurface leading to the following condition:

$$\begin{cases} \bar{X}_{11}^{loc}\left(\boldsymbol{\rho}'\right)M_{11}^{loc}\left(\boldsymbol{\rho}'\right)\left|H_2^{loc}\left(\boldsymbol{\rho}'\right)\right| = c \\ \bar{X}_{12}^{loc}\left(\boldsymbol{\rho}'\right)M_{12}^{loc}\left(\boldsymbol{\rho}'\right)\left|H_2^{loc}\left(\boldsymbol{\rho}'\right)\right| = c \end{cases} \tag{44}$$

where c is a constant that depends on the possibilities offered by the implementation method. This constant is maximized in order to have the maximum amplitude of the generated leaky wave.

Equation (44) imposes a condition on the product $\bar{X}_{ij}M_{ij}$ but not on their individual values. However, since the dispersion constant k_t^{sw} is affected mainly by the average impedance values, smooth continuous variations of these have to be imposed to avoid undesired reflections. In the following, a linear variation of $\bar{X}_{ij}^{loc}$ along the direction of propagation is supposed. However, other variation laws could be used.

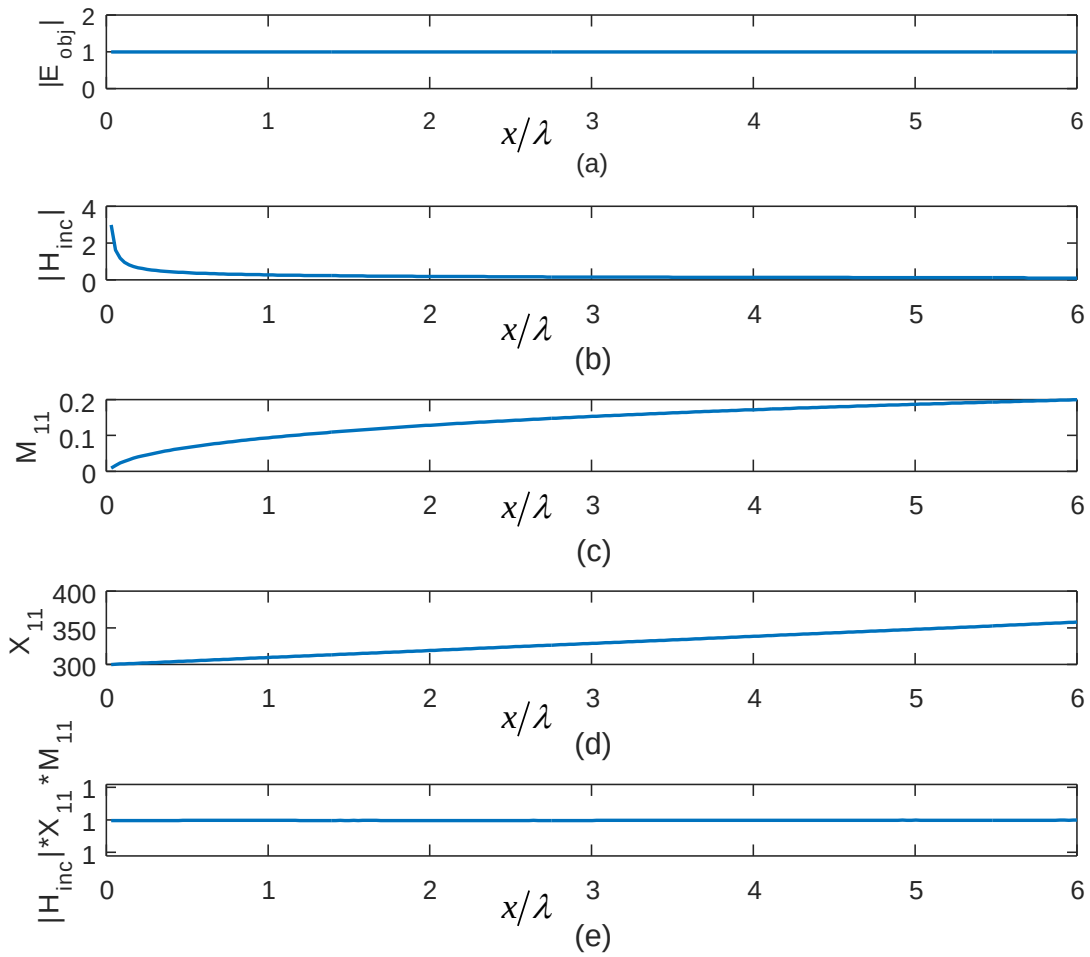

Figure 24: Compensation of the surface wave spreading factor example. (a) Objective amplitude distribution. (b) Amplitude of the incident wave. (c) Variation of the modulation index M . (d) Variation of the average impedance $\bar{X}$. (e) Amplitude of the generated leaky wave (normalized).

Figure 24 presents an example of spreading factor compensation. The example treats a single component case on a distance of 6λ . It can be seen from the example that using a product $\bar{X}M$ varying depending on the position, the amplitude of the generated leaky wave is constant (Figure 24.(e)).

It should be noted that the variation of the average impedance leads to a variation of the dispersion constant k_t^{sw} . This may affect the phase of the incident wave along the metasurface and may lead to a detuning in the phase matching of the leaky wave. To solve this, the average impedances variation laws are imposed before the phase

matching. Therefore, the detuning due to this variation is automatically corrected by the local holographic procedure.

2.3.2.2 Step 2: Generation of the desired amplitude distribution

After compensating the spreading factor of the surface wave, the product $\bar{X}_{ij}M_{ij}$ is modified in order to obtain arbitrary amplitude distributions of the generated leaky wave. This is obtained by multiplying the modulation indices obtained in the previous step by the objective amplitudes as described by the following equation :

$$\begin{cases} M_{11}^{loc}\left(\boldsymbol{\rho}'\right) = M_{11}^{loc,u}\left(\boldsymbol{\rho}'\right)\left|E_1^{loc,obj}\left(\boldsymbol{\rho}'\right)\right| \\ M_{12}^{loc}\left(\boldsymbol{\rho}'\right) = M_{12}^{loc,u}\left(\boldsymbol{\rho}'\right)\left|E_2^{loc,obj}\left(\boldsymbol{\rho}'\right)\right| \end{cases} \tag{45}$$

where

$M_{ij}^{loc,u}\left(\boldsymbol{\rho}'\right)$ are the modulation indices giving uniform distribution.

$M_{ij}^{loc}\left(\boldsymbol{\rho}'\right)$ are the modulation indices giving the desired amplitude distribution.

Equation (44) and (45) can then be combined in a single equation giving the amplitude matching condition described as follows:

$$\begin{cases} \bar{X}_{11}^{loc}\left(\boldsymbol{\rho}'\right)M_{11}^{loc}\left(\boldsymbol{\rho}'\right)\left|H_2^{loc}\left(\boldsymbol{\rho}'\right)\right| = c\left|E_1^{loc,obj}\left(\boldsymbol{\rho}'\right)\right| \\ \bar{X}_{12}^{loc}\left(\boldsymbol{\rho}'\right)M_{12}^{loc}\left(\boldsymbol{\rho}'\right)\left|H_2^{loc}\left(\boldsymbol{\rho}'\right)\right| = c\left|E_2^{loc,obj}\left(\boldsymbol{\rho}'\right)\right| \end{cases} \tag{46}$$

Figure 25 presents an example of amplitude generation using variating modulation index along the propagation direction. The figure illustrates the objective amplitude variation, the amplitude of the incident wave, the variation of the modulation index and the average impedance and the amplitude of the generated leaky wave. The objective amplitude presented in this example is a tapered amplitude distribution (Figure 25.(a)). It can be seen from the figure that the amplitude of the generated leaky wave (Figure 25.(e)) corresponds to the objective amplitude variation.

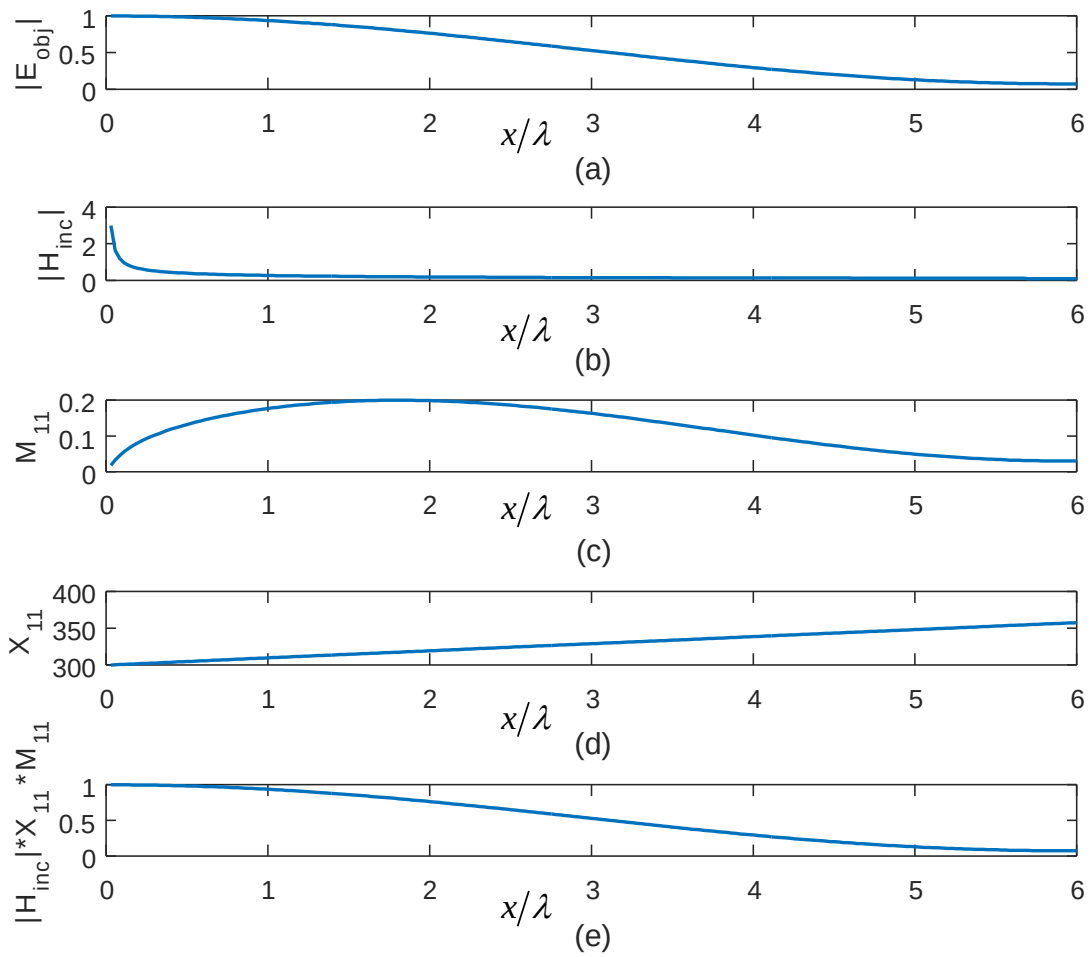

Figure 25: Generation of arbitrary field amplitude distribution. (a) Objective amplitude distribution. (b) Amplitude of the incident wave. (c) Variation of the modulation index M . (d) Variation of the average impedance $\bar{X}$. (e) Amplitude of the generated leaky wave (normalized).

2.4 Conclusion of the chapter

In this chapter, a method for the generation of arbitrary aperture field distributions using tensor metasurfaces is presented. The working principle of these metasurface antennas is based on the conversion of excited surfaces waves to leaky waves propagating away from the metasurface.

By introducing a sinusoidal modulation of the metasurface impedance components, an

infinity of hybrid modes are generated. The modulation parameters are chosen in such a way that only modes of order -1 are non-negligible leaky waves. These modes are then controlled using the modulation parameters in order to obtain the desired aperture field distribution above the metasurface. As the modulation parameters are controlled independently, the metasurface is not periodical; Even though each individual component is periodical.

On one hand, the phase of the generated leaky wave is controlled using modulation of the periodicities of the individual components. The objective phase distribution is obtained using the holographic principle in the tensorial case. In order to obtain the desired phase matching and at the same time ensuring the physical feasibility of the metasurface (anti-Hermitian impedance tensor), a local framework is introduced at each point of the metasurface. The holography principle is then applied in this local framework (equation (42)) to obtain the desired phase distribution above the metasurface.

On the other hand, for each component, the amplitude of the generated leaky wave is proportional to the product of the average impedance with the modulation index. The desired amplitude distribution is then obtained by varying these parameters depending on the position on the metasurface. The two parameters are used in order to compensate the spreading factor of the excited surface wave while at the same time imposing the desired amplitude distribution above the metasurface (equation (46)).

Equations (42) and (46) are the main blocks of the proposed formulation describing idealized continuous metasurfaces. In practice, these metasurfaces are implemented by printing sub-wavelength asymmetric patches over a dielectric substrate as already proposed in [16]-[20] and [22]-[26]. In the next chapter, the implementation method of this type of metasurfaces as well as the excitation of the surface wave is presented.

Chapter 3. Implementation of the metasurfaces

3.1 Introduction

In the previous chapter, leaky wave generation using modulated tensorial metasurfaces was addressed. By controlling the generated leaky waves, arbitrary aperture field distribution can be generated with control on both phase and amplitude distributions. The metasurfaces treated in the previous chapter are idealized continuous metasurfaces with arbitrary excitation of the surface wave. In our work, we focused on the most common case of a cylindrical surface wave excitation obtained using a coaxial probe placed at the center of the metasurface. In addition, the metasurfaces are implemented by printing subwavelength metallic patches over a grounded dielectric substrate resulting in a square grid of printed patches discrete metasurface.

In the present chapter, we start by developing the previous formulation for the cylindrical surface wave excitation case. Practical considerations such as field continuity, surface wave wave-front and incident wave estimation are treated. Then, the implementation of the discrete metasurface on a grounded dielectric slab is addressed. A new unit-cell having multiple degrees of freedom is presented. Finally, a step by step design algorithm starting from the objective aperture field to the corresponding metasurface design is presented.

3.2 Cylindrical wave excitation

In most practical cases, a cylindrical surface wave is excited using a coaxial probe placed at the center of the metasurface [16]-[20] and [22]-[26] (Figure 26). For this widely used geometry, the cylindrical coordinates system represents a natural global framework. The impedance boundary condition will then have the following form:

$$\begin{bmatrix} E_\rho(\boldsymbol{\rho}') \\ E_\phi(\boldsymbol{\rho}') \end{bmatrix} = j \begin{bmatrix} X_{\rho\rho}(\boldsymbol{\rho}') & X_{\rho\phi}(\boldsymbol{\rho}') \\ X_{\rho\phi}(\boldsymbol{\rho}') & X_{\phi\phi}(\boldsymbol{\rho}') \end{bmatrix} \begin{bmatrix} -H_\phi(\boldsymbol{\rho}') \\ H_\rho(\boldsymbol{\rho}') \end{bmatrix} \tag{47}$$

In the previously developed formulation, a linear variation of the average impedance

was imposed in order to compensate for the spreading factor of the surface wave. Imposing a radial variation of the average impedance introduces radial symmetry (invariance with respect to the azimuthal angle ϕ) in $\bar{X}_{ij}(\boldsymbol{\rho}') = \bar{X}_{ij}(\rho')$, thus $\partial \bar{X}_{ij}(\rho')/\partial\phi = 0$.

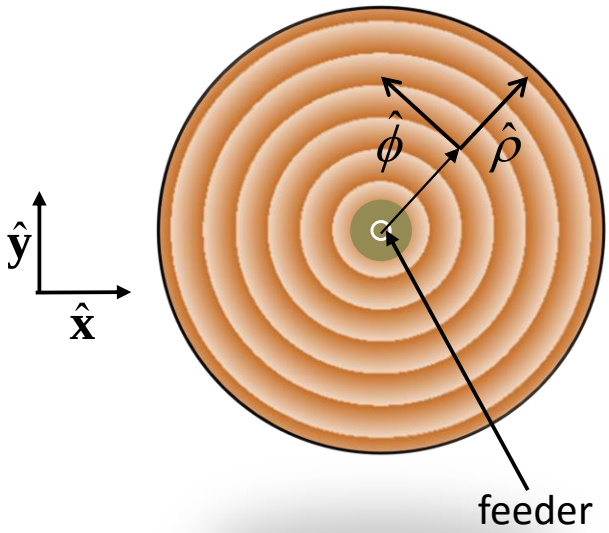

Figure 26: Cylindrical wave surface wave excitation.

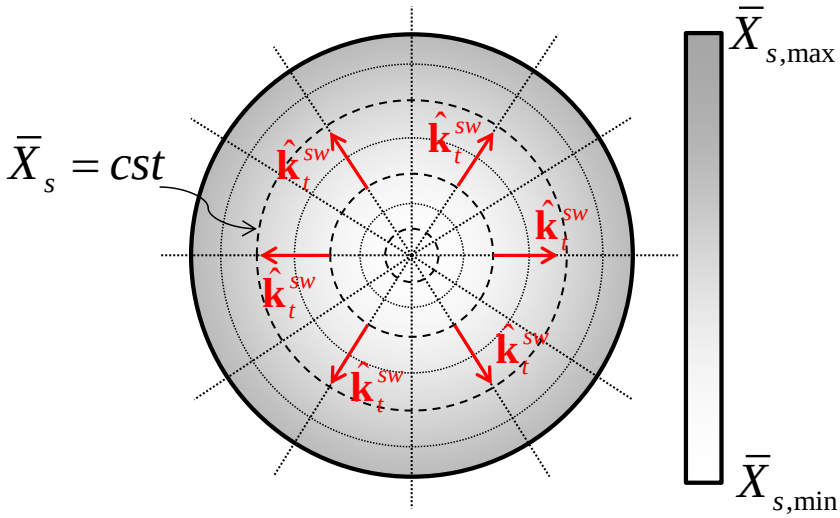

Figure 27: Radial variation of the effective impedance over the metasurface.

As a result, the excited cylindrical surface wave travelling from the center to the periphery of the metasurface continues to have a radial direction of propagation $\hat{\mathbf{k}}_t^{sw}(\boldsymbol{\rho}') = \hat{\boldsymbol{\rho}}, \forall \boldsymbol{\rho}'$ as shown in Fig.27. In addition, we assume that under a small modulation index, the impedance modulation does not affect the radial propagation of the surface wave.

3.2.1 Local framework derivation

The local framework at each point of the metasurface is derived by replacing equation (27) into (20) to obtain the expression of the tangential electric field $\mathbf{E}_t(\boldsymbol{\rho}')$ and magnetic field $\mathbf{H}_t(\boldsymbol{\rho}')$, yielding:

$$\begin{aligned}\mathbf{E}_t(\boldsymbol{\rho}') &= I_{TM}(\boldsymbol{\rho}')\, j\zeta_0 \left[\Delta(\boldsymbol{\rho}')\hat{\boldsymbol{\rho}} + \frac{X_{\rho\rho}(\boldsymbol{\rho}') - \zeta_0\Delta(\boldsymbol{\rho}')}{\Delta(\boldsymbol{\rho}')\, X_{\rho\phi}(\boldsymbol{\rho}')}\hat{\boldsymbol{\phi}}\right] \mathrm{H}_1^{(2)}(k_{sw}\rho') \\ \mathbf{H}_t(\boldsymbol{\rho}') &= -I_{TM}(\boldsymbol{\rho}') \left[\frac{X_{\rho\rho}(\boldsymbol{\rho}') - \zeta_0\Delta(\boldsymbol{\rho}')}{X_{\rho\phi}(\boldsymbol{\rho}')}\hat{\boldsymbol{\rho}} + \hat{\boldsymbol{\phi}}\right] \mathrm{H}_1^{(2)}(k_{sw}\rho')\end{aligned} \tag{48}$$

By defining the direction of the magnetic field $\mathbf{H}_t(\boldsymbol{\rho}')$ as a unit vector $\hat{\mathbf{x}}_2^{loc}(\boldsymbol{\rho}')$ of the local framework, we obtain:

$$\hat{\mathbf{x}}_2^{loc}(\boldsymbol{\rho}') = \frac{1}{\sigma(\boldsymbol{\rho}')}\hat{\boldsymbol{\phi}} + \frac{\left(X_{\rho\rho}(\boldsymbol{\rho}') - \zeta_0\Delta(\boldsymbol{\rho}')\right)}{\sigma(\boldsymbol{\rho}')\, X_{\rho\phi}(\boldsymbol{\rho}')}\hat{\boldsymbol{\rho}} \tag{49}$$

where the quantity

$\sigma(\boldsymbol{\rho}') = \sqrt{1 + \left(X_{\rho\rho}(\boldsymbol{\rho}') - \zeta_0\Delta(\boldsymbol{\rho}')\right)^2 / X_{\rho\phi}^2(\boldsymbol{\rho}')}$ is used for normalisation.

The second unit vector of the local framwork is then defined as

$$\hat{\mathbf{x}}_1^{loc}(\boldsymbol{\rho}') = \hat{\mathbf{x}}_2^{loc}(\boldsymbol{\rho}') \times \hat{\mathbf{z}} = \frac{1}{\sigma(\boldsymbol{\rho}')}\hat{\boldsymbol{\rho}} - \frac{\left(X_{\rho\rho}(\boldsymbol{\rho}') - \zeta_0\Delta(\boldsymbol{\rho}')\right)}{\sigma(\boldsymbol{\rho}')\, X_{\rho\phi}(\boldsymbol{\rho}')}\hat{\boldsymbol{\phi}} \tag{50}$$

The transformation matrix $\underline{\underline{\mathbf{R}}}(\boldsymbol{\rho}')$ from the global framework to the local framework is then directly given by

$$\underline{\underline{\mathbf{R}}}(\boldsymbol{\rho}') = \begin{bmatrix} \dfrac{1}{\sigma(\boldsymbol{\rho}')} & -\dfrac{X_{\rho\rho}(\boldsymbol{\rho}') - \zeta_0 \Delta(\boldsymbol{\rho}')}{\sigma(\boldsymbol{\rho}') X_{\rho\phi}(\boldsymbol{\rho}')} \\ \dfrac{X_{\rho\rho}(\boldsymbol{\rho}') - \zeta_0 \Delta(\boldsymbol{\rho}')}{\sigma(\boldsymbol{\rho}') X_{\rho\phi}(\boldsymbol{\rho}')} & \dfrac{1}{\sigma(\boldsymbol{\rho}')} \end{bmatrix} \tag{51}$$

The magnetic field and the current density in the local framework are given by:

$$\begin{aligned} \mathbf{H}_t^{loc}(\boldsymbol{\rho}') &= \underline{\underline{\mathbf{R}}}(\boldsymbol{\rho}') \cdot \mathbf{H}_t(\boldsymbol{\rho}') = -I_{TM}(\boldsymbol{\rho}') \sigma(\boldsymbol{\rho}') \mathrm{H}_1^{(2)}\left(k_t^{sw} \rho'\right) \hat{\mathbf{x}}_2^{loc}(\boldsymbol{\rho}') \\ \mathbf{J}^{loc}(\boldsymbol{\rho}') &= \hat{\mathbf{n}} \times \mathbf{H}_t^{loc}(\boldsymbol{\rho}') = I_{TM}(\boldsymbol{\rho}') \sigma(\boldsymbol{\rho}') \mathrm{H}_1^{(2)}\left(k_t^{sw} \rho'\right) \hat{\mathbf{x}}_1^{loc}(\boldsymbol{\rho}') \end{aligned} \tag{52}$$

The transformation matrix $\underline{\underline{\mathbf{R}}}(\boldsymbol{\rho}')$ has to be evaluated at each point of the metasurface in order to write the different electromagnetic quantities in the local framework.

3.2.2 Incident wave amplitude and phase estimation

A key step of the metasurface design is the estimation of the incident field defined by $\mathbf{H}_t(\boldsymbol{\rho}')$. In the case of cylindrical surface wave, the term $I_{TM}(\boldsymbol{\rho}')$ needed in (52) is the only unknown. This term can be found numerically using the geometrical optic based procedure introduced in [20] and extending it to the tensorial case.

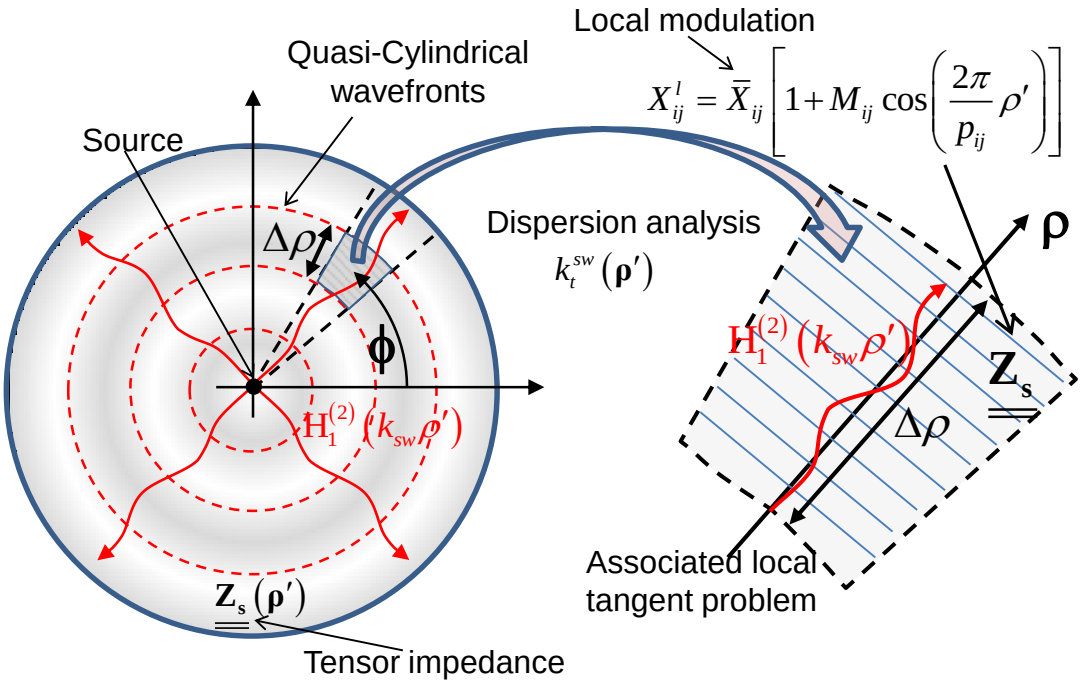

Figure 28: Radial variation of the effective impedance over the metasurface.

The impedance variation of the sinusoidally modulated metasurface can be interpreted as a two scales problem :

- A component with rapid variation rate, corresponding to sinusoidal variation of the impedance and governed by the periodicities p_{ij} .
- A component with slow rate given by the variation of the modulation parameters (M_{ij} , $\bar{X}_{ij}$, and p_{ij}).

Under optic approximation, the metasurface can be described by an equivalent impedance $\bar{X}_s$ obtained using the local periodic problem. The metasurface can then be considered as a slowly-variating equivalent surface impedance $\bar{X}_s(\boldsymbol{\rho}')$. It should be noted that even though the metasurface is loss-less, the equivalent impedance has a real part describing the energy loss due to leaky wave radiation [39].

The propagation problem can be solved numerically with the following steps:

- The metasurface is divided into sectorial areas where the propagation can be considered as mono-directional. For each direction ϕ, an associated local tangent problem with radial direction of propagation is defined (figure 28). Each local problem is defined by the impedance tensor described by equation (43).
- Each sectorial area is then divided into N sub-sections, along the propagation direction, in which the modulation parameters (M_{ij} , $\bar{X}_{ij}$, and p_{ij}) are assumed to be constant (figure 28).
- In each sub-domain, the dispersion problem is solved analytically using the procedure developed in our lab [39]. Using the proposed method, the complex wavenumber $k_{t,n,\phi}^{sw} = \beta_{t,n,\phi}^{sw} - j\alpha_{t,n,\phi}^{sw}$ associated to each sub-domain is estimated. $\beta_{t,n,\phi}^{sw}$ is the real perturbed local wavenumber and $\alpha_{t,n,\phi}^{sw}$ is the local leakage attenuation parameter.
- The local framework transformation matrix $\underline{\underline{\mathbf{R}}}(\boldsymbol{\rho}')$ defined by the equations (51) and (52) is calculated at each individual sub-domain.
- The incident magnetic field in the n-th section is then approximated in the local framework as

$$\mathbf{H}_t^{loc}(\boldsymbol{\rho}') = -I_{n,\phi}^{TM}(\boldsymbol{\rho}')\sigma(\boldsymbol{\rho}')\mathrm{H}_1^{(2)}\left(k_{t,n,\phi}^{sw}\rho'\right)\hat{\mathbf{x}}_2^{loc}(\boldsymbol{\rho}') \tag{53}$$

The complex magnitude $I_{n,\phi}^{TM}(\boldsymbol{\rho}')$ is obtained by imposing the continuity of the magnetic field across two adjacent sectors as described by the following equa-

tion:

$$I_{n,\phi}^{TM} = \frac{I_{n-1,\phi}^{TM}\sigma^{n-1}\left(\rho_n'\right)\mathrm{H}_1^{(2)}\left(k_{t,n-1,\phi}^{sw}\rho_n'\right)}{\sigma^{n}\left(\rho_n'\right)\mathrm{H}_1^{(2)}\left(k_{t,n,\phi}^{sw}\rho_n'\right)} \tag{54}$$

As the continuity of magnetic field is enforced by the equation (54) and the variation of the average impedance is smooth and continuous, we can assume a quasi-conservation of power at the different interfaces.

After estimating the incident wave on the metasurface and establishing the impedance variation using equations (42) and (46), the next step is to physically implement the metasurface structure.

3.3 Physical implementation of the metasurface

The impedance variation law found with the proposed formulation is independent from the approach used to implement the metasurface. Indeed, the surface impedance $\underline{\underline{\mathbf{Z}}}_s$ takes into account all of the interaction effects between the wave, the metasurface and the media below the $z = 0$ plane.

3.3.1 Metasurface structure

In this work, the metasurface structure is implemented using sub-wavelength metallic elements printed in a square lattice over a grounded dielectric substrate (Figure 29).

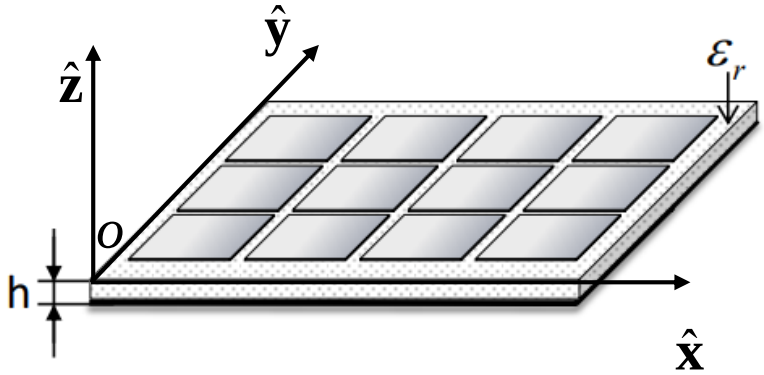

Figure 29: Metasurface structure composed by periodic metallic elements printed over a grounded substrate [39].

Several patches topologies giving tensor surface impedances are presented in the literature (Figure 30). In order to have an independent control of the impedance elements, a large range of impedance elements is needed. Therefore, a new unit cell geometry giving an additional degree of freedom was introduced (Figure 30.(a)).

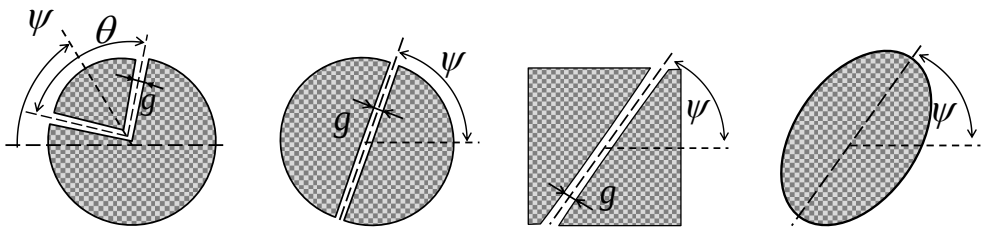

(a) (b) (c) (d)

Figure 30: Unit cell topologies. The chosen cell (a) consists of a circular patch with a v shaped slot. It is defined by slot wideness g, the orientation angle ψ and the slot aperture angle θ.

3.3.2 Unit cell parameters

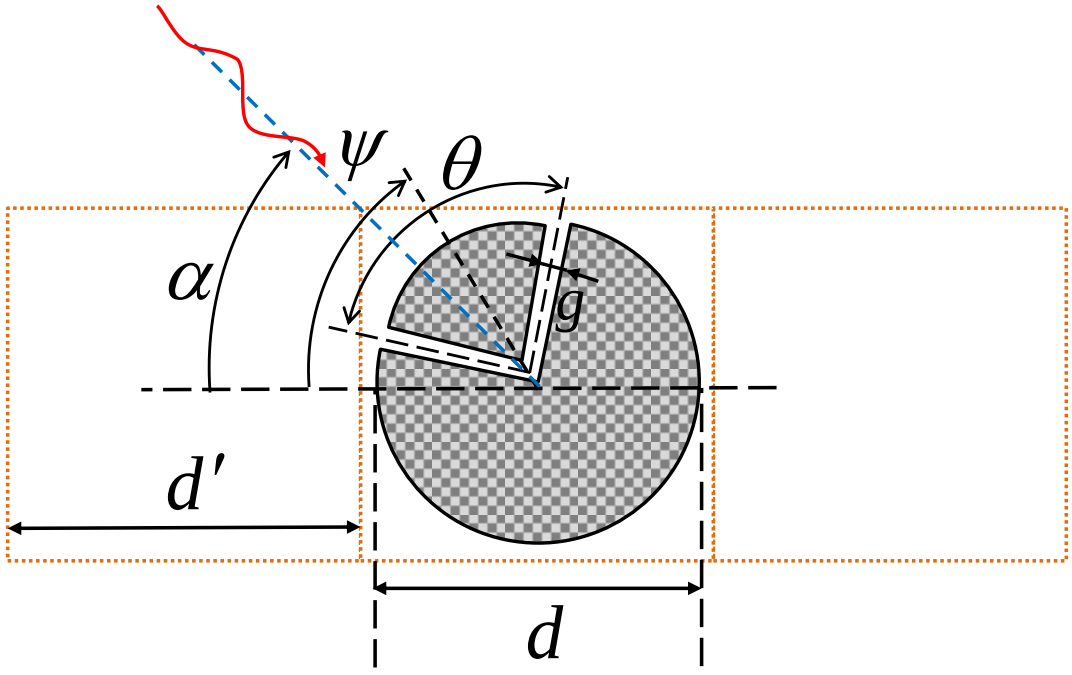

Figure 31: Unit cell design: circular patch with a v-shaped slot.

The proposed unit cell is a circular patch with a variable v-shaped slot (Figure 31). It presents an axis of symmetry corresponding to the middle of the v-shaped slot. The

patch geometry is described by the following parameters:

- The lattice periodicity d'. This quantity corresponds to the unit cell dimension and it should not be confused with the modulation periodicity of the impedance component p_{ij}.
- The patch dimension d. For the considered unit cell topology, it corresponds to the diameter of the circular patch.
- The filling factor $a_{\%} = \frac{d}{d'}$. It is defined as the ratio of the unit cell dimension over the structure periodicity. It is expressed in %.
- The slot size g. It gives the width of the v-shaped slot. In our case, it is expressed as a fraction of the filling factor.
- The opening angle of the v-shaped slot. It is expressed by the parameter θ.
- The incident angle of the electromagnetic wave. It gives the angle between the direction of propagation of the incident wave and the axes of the square lattice. It is expressed by the parameter α.
- The cell rotation. It gives the angle between the axe of symmetry of the unit cell and the square lattice of the structure. It is expressed by the parameter ψ.

It should be noted that the rotation of the incident angle α is not equivalent to the rotation ψ of the unit cell in the opposite direction (see figure 32). The two structures are not equivalent due to the periodicity of the structure in a square lattice. It is therefore important to consider these two rotation parameters separately.

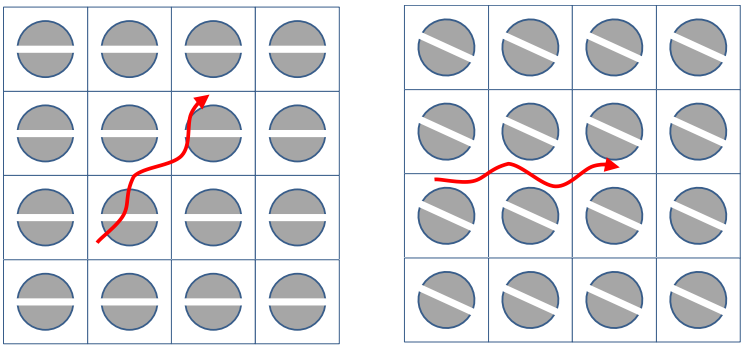

(a) (b)

Figure 32: Comparison between the rotation of the unit cell and the incident angle of the surface wave. (a) Rotation of the incident angle ($(\psi,\alpha)=(0°,-30°)$). (b) Rotation of the unit cell ($(\psi,\alpha)=(30°,0°)$).

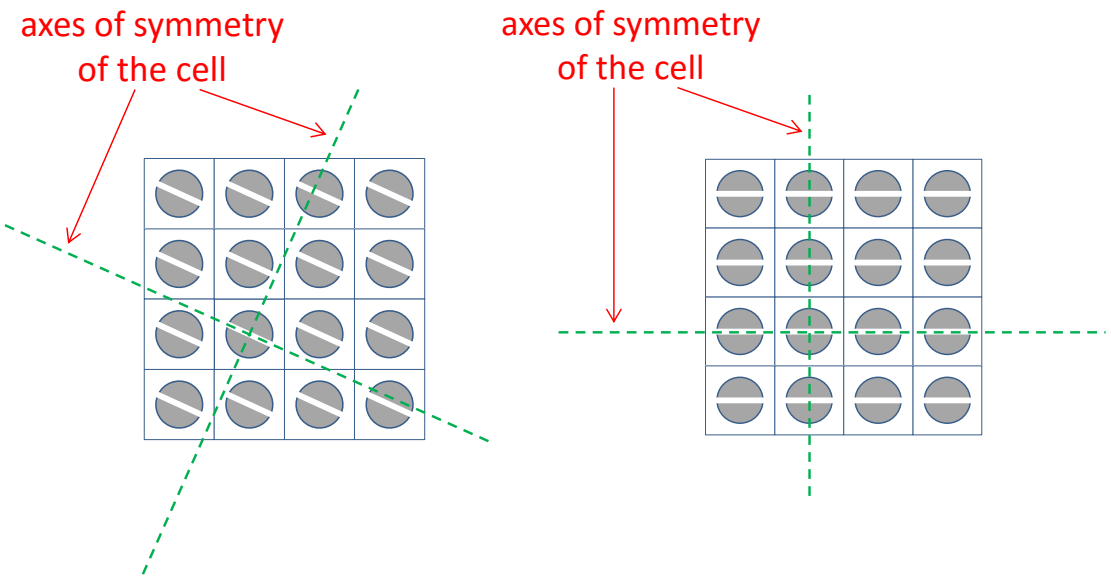

(a) (b)

Figure 33: Effect of the symmetry of the unit cell on the symmetry of the metasurface structure. (a) Symmetry of the unit cell not aligned with the lattice. (b) Symmetry of the unit cell aligned with the lattice.

Another important aspect is the symmetry of the metasurface. In the case of a symmetrical metasurface, the impedance tensor is diagonal when the incident wave propagates in the direction of the symmetry axis. However, it should be noted that symmetry of the unit cell is not equivalent to the symmetry of the metasurface. In the example of figure 33.(a), the unit cell has two axis of symmetry while the metasurface structure is not symmetrical. This is due to the square lattice of the metasurface. A symmetrical unit cell gives a symmetrical metasurface when the axes of symmetry of the cell are parallel to the axes of the square periodicity of the structure (Figure 33.(b)).

3.3.3 Surface impedance calculation

In order to estimate the impedance tensor corresponding to a given unit cell, the metasurface is assumed to be locally periodical (in terms of spatial periodicity and not modulation periodicity). As a result, the impedance tensor is calculated for an infinite periodical metasurface composed of same unit cell (the unit cell of interest).

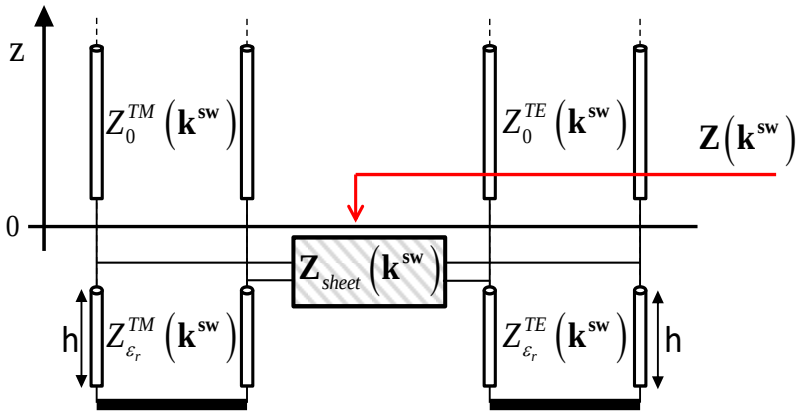

Figure 34: Printed metasurface equivalent TM and TE transmission lines.

In order to estimate the surface impedance tensor $\underline{\underline{\mathbf{Z}_s}}\left(\mathbf{k}^{sw}\right)$, an in-house model based on periodical Method of Moment already developed in our lab is used. The model is used to characterize the surface impedance by taking into account all the different dispersion effects (dispersion of the dielectric substrate, presence of the ground plane…). The metasurface is represented by the equivalent transmission lines circuit described in figure 34. The equivalent circuit is composed of two transmission lines (TE and TM) coupled together with the sheet impedance tensor $\mathbf{Z}_{sheet}\left(\mathbf{k}^{sw}\right)$. It should be noted that the surface impedance and the sheet impedance tensors are defined for a given wavenumber $\mathbf{k}^{sw}$.

The surface impedance tensor is calculated by the following steps:

- Using a Method of Moment and the Green function of a periodic grounded dielectric slab, the wavenumber $\mathbf{k}^{sw}$ of the propagating surface wave is numerically calculated. Its value is obtained by imposing that $\det\left(\mathbf{Z}_{MoM}\right)=0$.
- The sheet impedance $\mathbf{Z}_{sheet}\left(\mathbf{k}^{sw}\right)$ associated to this particular wavenumber is calculated by projecting the induced current of the patch on the corresponding TM/TE mode.
- The surface impedance $\underline{\underline{\mathbf{Z}_s}}\left(\mathbf{k}^{sw}\right)$ is then obtained by adding the contribution of the grounded dielectric slab at the resonant wavenumber $\mathbf{k}^{sw}$.

The metasurface design procedure presented in the chapter 2 is independent of the implementation method used in order to obtain the surface impedance distribution. The MoM model will then be modified or replaced if another implementation method is used (multi-layer substrate…).

3.3.4 Database generation

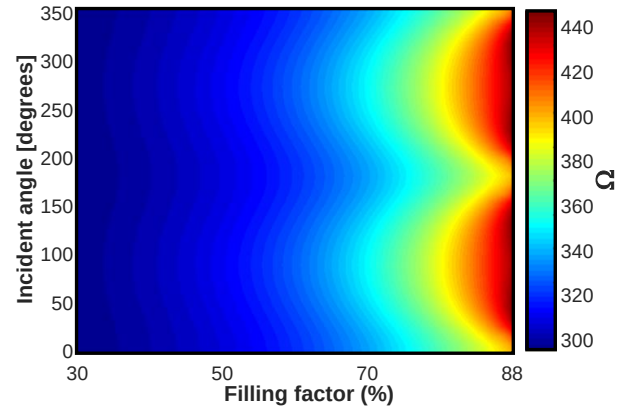

(a)

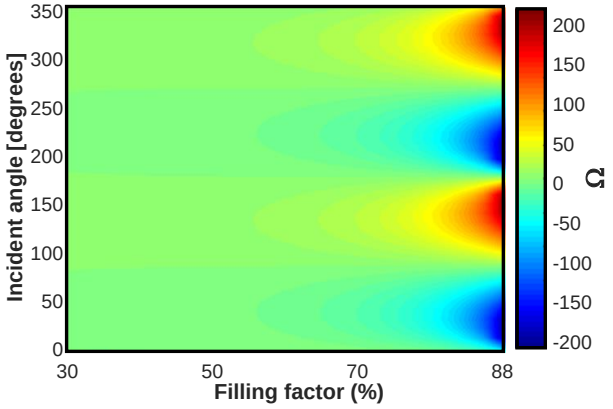

(b)

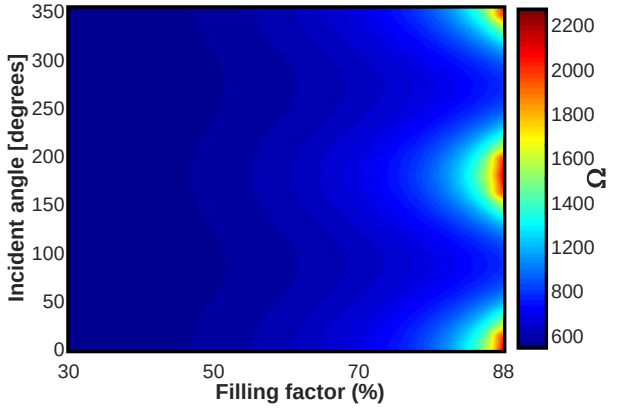

(c)

Figure 35: Reactance levels corresponding to the unit cells of slot size $g = 0.2$ and angles $\theta = 60°$ and $\psi = 0°$ printed over a substrate TMM6 of permittivity 6 and thickness 1.27mm : $X_{\rho\rho}$ (a), $X_{\phi\rho}$ (b), and $X_{\phi\phi}$ (c).

As stated in the two previous sub-sections, the impedance tensor is affected by the unit cell parameters, the surface wave wavenumber $\mathbf{k}^{sw}$ and the structure of the metasurface (printed patches over a grounded dielectric slab).

Figure 35 presents the variations of the impedance parameters written in the cylindrical coordinates with respect to the filling factor (horizontal axis) and the incident angle (vertical axis). These values have been calculated using the MoM model for a unit cell for parameters $g = 0.2$, $\theta = 60°$ and $\psi = 0°$, a working frequency of 20GHz and a substrate Rogers TMM6 of relative permittivity 6 and thickness 1.27mm.

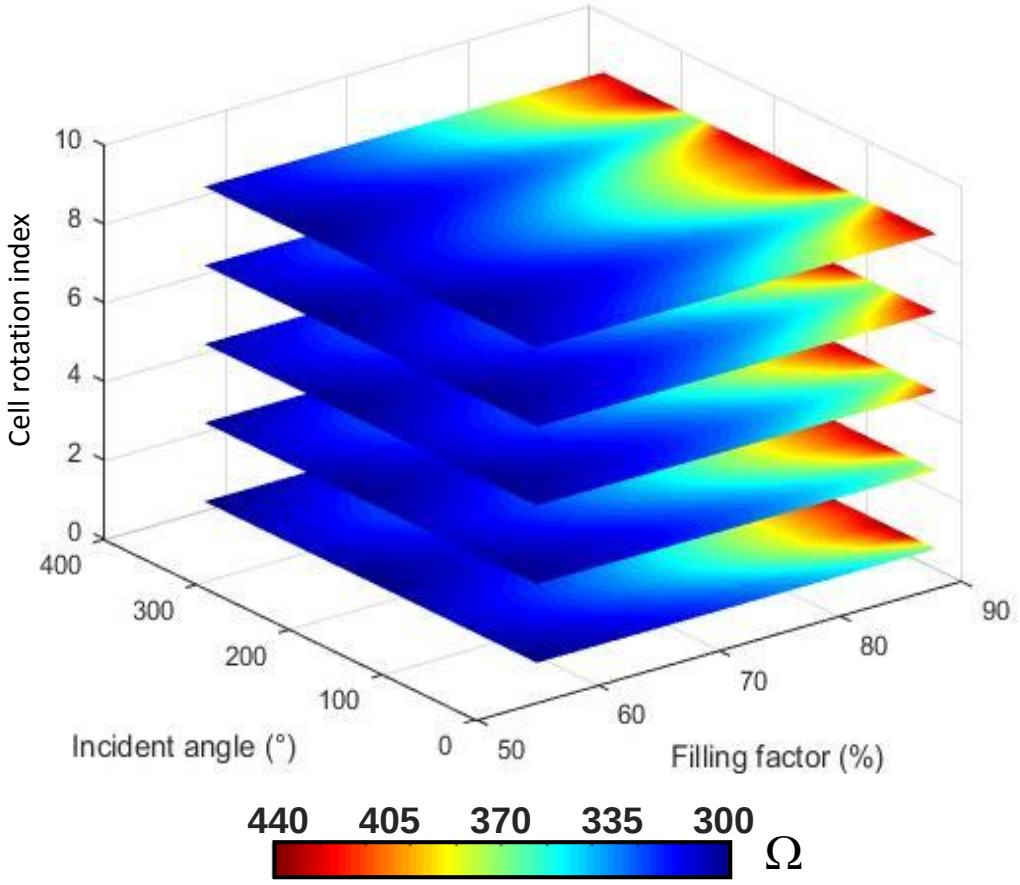

Figure 36: Tensorial reactance database generation. Component $X_{\rho\rho}$ of the impedance tensor for a substrate Rogers TMM6 of relative permittivity 6 and thickness 1.27mm. The working frequency is 20GHz.

By varying the unit cell parameters such as the orientation angle ψ and the slot opening θ, a database containing reactance maps (similar to those in figure 35) is generat-

ed. Figure 36 illustrate the generated database of the $X_{\rho\rho}$ component for the same substrate configuration. Similar databases have to be generated if the working frequency or the dielectric substrate are changed.

3.3.5 Spatial discretization of the metasurface

In order to implement the metasurface with a square grid of printed patches, the impedance variation law $\underline{\underline{\mathbf{Z}_s}}(\boldsymbol{\rho}')$ needs to be discretized with respect to the position on the metasurface. In this context, the metasurface is discretized into a square grid of discretization step $\Delta x = \Delta y$. The average impedance, the modulation index and the periodicity of each impedance component are assumed to be constant inside the unit cells. Their value is set to be equal to the central value of the impedance modulation parameters.

Figure 37 presents the variation of the reactance $X_{\rho\rho}$ of a given metasurface for different values of the discretization step $\Delta x = \Delta y = \frac{\lambda}{3}, \frac{\lambda}{6}, \frac{\lambda}{12}$. It can be seen from the figure that the impedance variation is not described well with a step of $\Delta x = \Delta y = \frac{\lambda}{3}$ and starts to be visible for $\Delta x = \Delta y > \frac{\lambda}{6}$. In order to have a good description of the impedance variation, a discretization step of $\Delta x = \Delta y = \frac{\lambda}{12}$ was used. This parameter is also used as a spatial periodicity of the metasurface structure $d' = \frac{\lambda}{12}$.

The discrete metasurface is now described by the discrete impedance elements $X_{ij}^{d}(x_k, y_l)$ in the global framework and $X_{ij}^{d,loc}(x_k, y_l)$ in the local one. The resulting metasurface will then have three variation scales:

- A slow variation of the modulation parameters M_{ij}, $\overline{X}_{ij}$, and p_{ij} of the impedance components.
- A fast variation of the impedance due to the sinusoidal modulation and governed by the periodicity p_{ij}.
- An “apparent” very fast variation between two adjacent discrete positions.

The latter variation is only “apparent” in the sense that, since the impedance elements are small compared to the wavelength, the real physical boundary condition “feel” by the wave is a sort of average impedance between adjacent different values. This effect recreates a continuous impedance condition (homogenization).

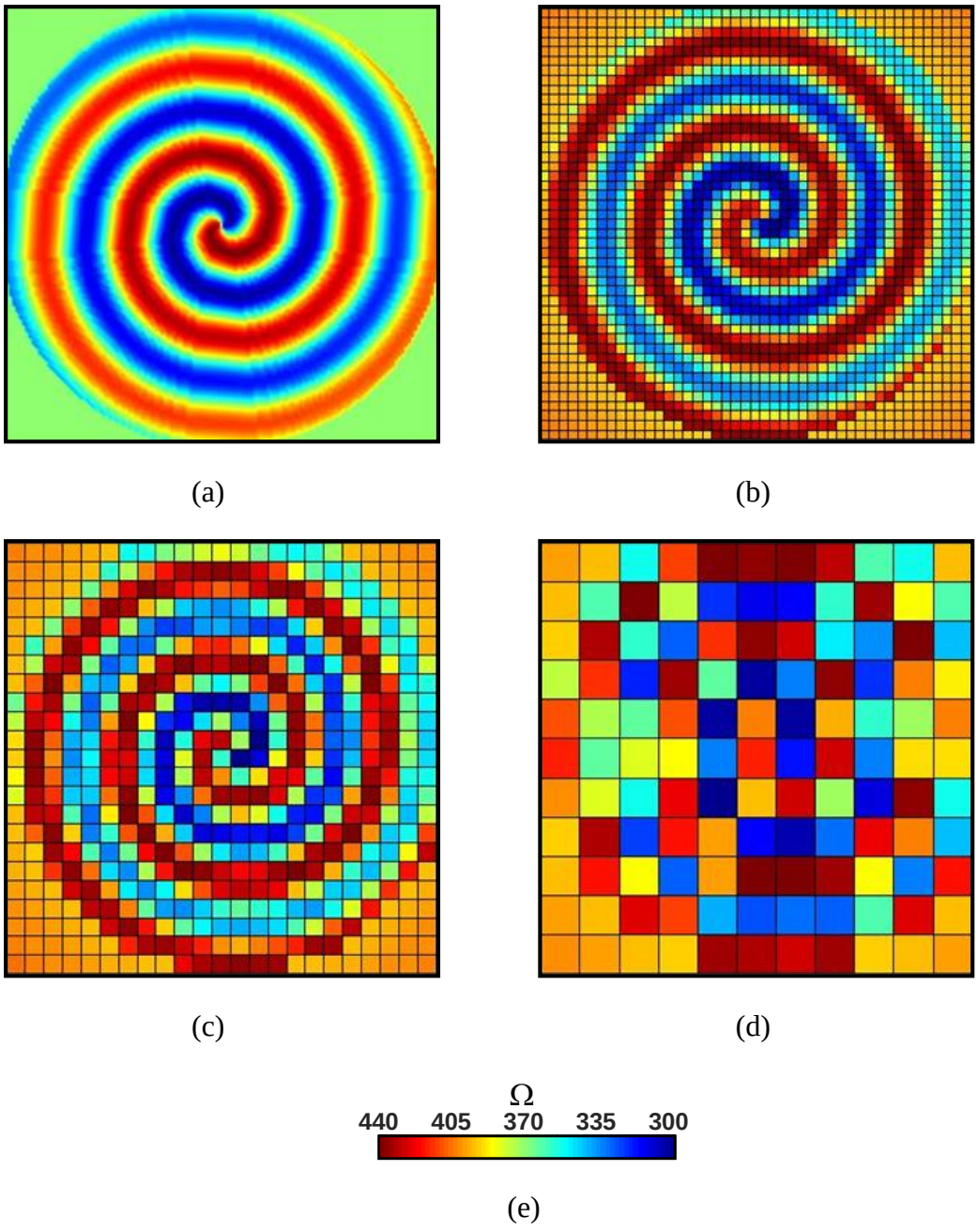

Figure 37: Effect of the spatial discretization on the reactance variation. Effect of the discretization on the $X_{\rho\rho}$ component for different discretization steps : (a) Continuous impedance. (b) $\Delta x = \Delta y = \lambda/12$. (c) $\Delta x = \Delta y = \lambda/6$. (d) $\Delta x = \Delta y = \lambda/3$. (e) Impedance scale.

3.4 Implementation algorithm

In this section, the algorithm for the design and implementation of modulated tensorial metasurfaces for aperture field generation is summarized and detailed. Figure 38 shows the algorithm flowchart describing each step needed for the implementation of an arbitrary aperture field distribution $\mathbf{E}_t^{obj}(\boldsymbol{\rho}')$. The algorithm described in this chapter was implemented in a MATLAB code.

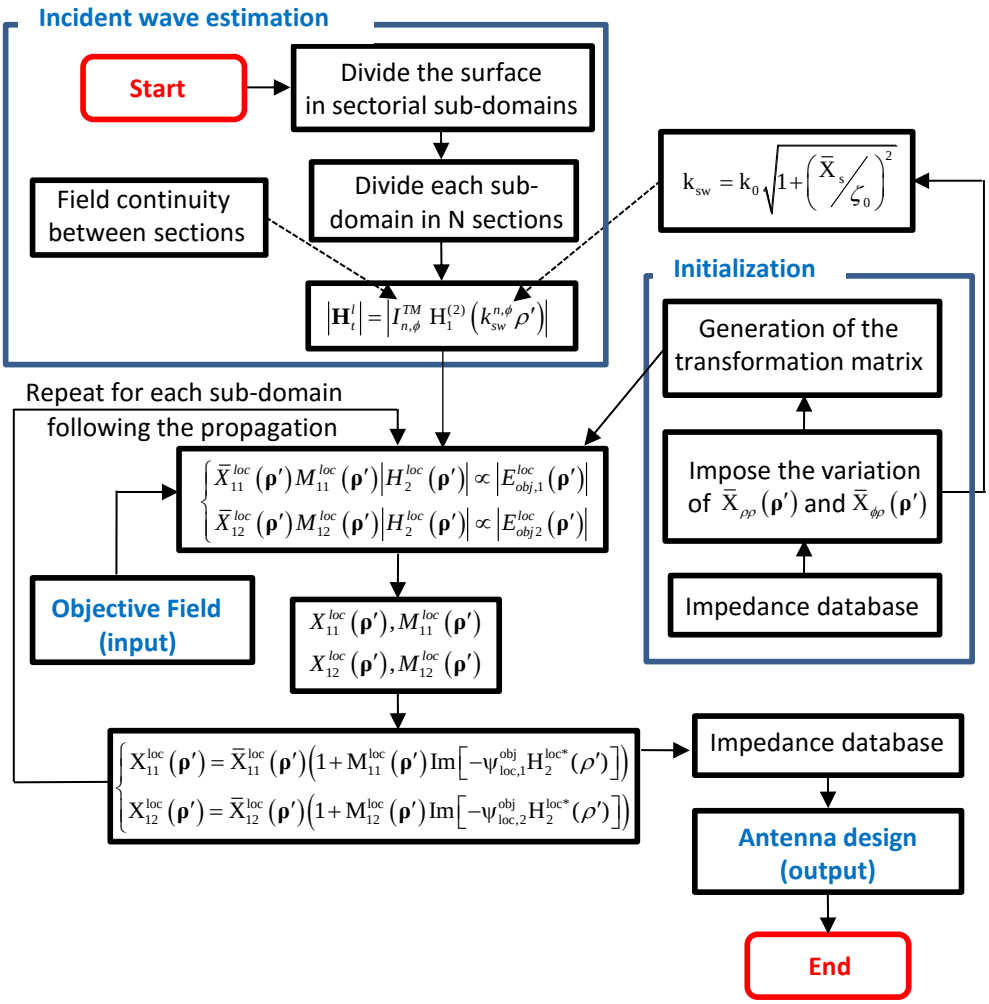

Figure 38: Flowchart of the metasurface implementation algorithm.

The algorithm is composed by the following steps:

3.4.1 Preliminary steps

These steps are independent of the objective aperture field distribution. They are carried out as follows :

- Step 1.1 : The working frequency is fixed
- Step 1.2 : The dielectric substrate and the unit cell design are selected. It should be noted that these two elements are chosen so that the achievable impedance variation range is the largest possible.
- Step 1.3 : Generation of the impedance database using the MoM model for a fixed discretization step.
- Step 1.4 : The average impedance variation laws and the maximum values of the modulation indices are fixed. These values are obtained by ensuring that the impedance variation stays always inside the impedance database.
- Step 1.5 : The metasurface is decomposed into subdomains, along the direction of propagation, in which the surface modulation is assumed to be constant. For a cylindrical surface wave excitation, the metasurface is divided into angular subdomains and then each subdomain is divided into N elementary sections.

These important steps are further described in the table 3.1.

Step	Input	Step description	Output
1.1	f	Fix the working frequency.	k_0, λ
1.2	-	Selected the dielectric substrate and the unit cell design.	ε_r, h, d'
1.3	f, ε_r, h, d'	Generate the impedance database using the MOM model.	X_{ij}^{DB}
1.4	X_{ij}^{DB}	Impose the average impedance variation and the maximum value of modulation indices.	$\bar{X}_{ij}(\boldsymbol{\rho}')$, $\max(M_{ij})$
1.5	-	Divide the metasurface into sectors and sections.	-

Table 3.1: Preliminary steps of the design algorithm.

3.4.2 Continuous impedance determination

After performing the preliminary steps, the objective aperture field distribution is defined $\mathbf{E}_t^{obj}(\boldsymbol{\rho}')$. After that, starting from the source and following the propagation path, the impedance $\underline{\underline{\mathbf{Z}}}_{\mathbf{s}}(\boldsymbol{\rho}')$ is calculated on each sector by performing the following steps :

- Step 2.1 : The propagation constant $k_{t,n,\phi}^{sw}$ is found by solving the local dispersion problem [39].
- Step 2.2 : The magnetic field amplitude and phase are found using equation (54) by imposing the continuity of the magnetic field at the sections interface.
- Step 2.3 : The transformation matrix $\underline{\underline{\mathbf{R}}}(\boldsymbol{\rho}')$ is found and used in order to write the incident and the objective fields in the local framework.
- Step 2.4 : The modulation indices $M_{11}^{loc}(\boldsymbol{\rho}')$ and $M_{12}^{loc}(\boldsymbol{\rho}')$ are calculated using the amplitude matching condition described by equation (46).
- Step 2.5 : The impedance variation $\underline{\underline{\mathbf{Z}}}_{\mathbf{s}}(\boldsymbol{\rho}')$ is obtained using equation (43) (local holography formulation) and equation (46).

The steps for the calculation of the continuous impedance variation are further described in table 3.2.

Step	Input	Step description	Eq	Output
For each sector (loop on the sectors)				
Starting from source and following the propagation path				
2.1	$\bar{X}_{ij}(\boldsymbol{\rho}')$, $\max(M_{ij})$	Estimate the propagation constant by solving the local dispersion problem [39].	-	$k_{t,n,\phi}^{sw}$
2.2	-	Find the magnetic field amplitude and phase	(54)	$\mathbf{H}_t(\boldsymbol{\rho}')$

2.3	$\bar{X}_{ij}(\boldsymbol{\rho}')$	Define the local framework transformation matrix $\underline{\underline{\mathbf{R}}}(\boldsymbol{\rho}')$.	(51) ,(52)	$\underline{\underline{\mathbf{R}}}(\boldsymbol{\rho}')$, $\mathbf{H}_t^{loc}(\boldsymbol{\rho}')$, $\mathbf{E}_t^{loc,obj}(\boldsymbol{\rho}')$
2.4	$\mathbf{H}_t^{loc}(\boldsymbol{\rho}')$, $\mathbf{E}_t^{loc,obj}(\boldsymbol{\rho}')$, $\bar{X}_{ij}(\boldsymbol{\rho}')$	Calculate the modulation indices $M_{11}^{loc}(\boldsymbol{\rho}')$ and $M_{12}^{loc}(\boldsymbol{\rho}')$.	(46)	$M_{11}^{loc}(\boldsymbol{\rho}')$, $M_{12}^{loc}(\boldsymbol{\rho}')$
2.5	$\mathbf{H}_t^{loc}(\boldsymbol{\rho}')$, $\mathbf{E}_t^{loc,obj}(\boldsymbol{\rho}')$, $\bar{X}_{ij}(\boldsymbol{\rho}')$, $M_{11}^{loc}(\boldsymbol{\rho}')$, $M_{12}^{loc}(\boldsymbol{\rho}')$	Calculate the impedance variation law $\underline{\underline{\mathbf{Z}_s}}(\boldsymbol{\rho}')$.	(43)	$\underline{\underline{\mathbf{Z}_s}}(\boldsymbol{\rho}')$

Table 3.2: Continous impedance determination algorithm.

3.4.3 Metasurface design generation

After calculating the impedance varation law, the metasurface design is generated with the following steps:

- Step 3.1 : The metasurface is discretized into a rectangular grid with a discretization step equal to the unit cell spatial periodicity ($\Delta x = \Delta y = d'$).
- Step 3.2 : The discrete impedance components $X_{ij}^d(x_k, y_l)$ are defined as the value of the continuous impedance at the center of the squares.
- Step 3.3 : At each discrete point, the unit cell giving the desired impedance $X_{ij}^d(x_k, y_l)$ is found in the impedance database. The unit cell is described by the orientation angle ψ , the slot opening θ, and the filling factor. It should be noted that the impedance database is scanned for a fixed incident angle corresponding to the position (x_k, y_l).
- Step 3.4 : A DXF (Drawing eXchange Format) file corresponding to the impedance design is generated.

The steps corresponding to the metasurface design generation are described in Table 3.3.

Step	Input	Step description	Output
3.1	$\Delta x = \Delta y = d'$	Discretize the metasurface into rectangular grid.	(x_k, y_l)
3.2	$X_{ij}(\boldsymbol{\rho}')$	Define the discrete impedance as the value at the center.	$X_{ij}^{d}(x_k, y_l)$
3.3	X_{ij}^{DB}, (x_k, y_l)	Find the unit cell giving the desired impedance in the impedance database.	$\theta(x_k, y_l)$, $\psi(x_k, y_l)$, filling factor
3.4	$\theta(x_k, y_l)$, $\psi(x_k, y_l)$, filling factor	Generate the metasurface design.	DXF file

Table 3.3: Final metasurface design generation.

3.5 Feeder design

The last step of the metasurface antenna implementation is the design of the feeding structure. The geometry shown in figure 39 is used to excite a cylindrical surface wave on the metasurface. The feeding structure consists of a circular patch of outer radius r_2 with an annular slot of inner radius r_1 and width e. The inner circle of the feeder is connected to the core of a coaxial cable from below the metasurface.

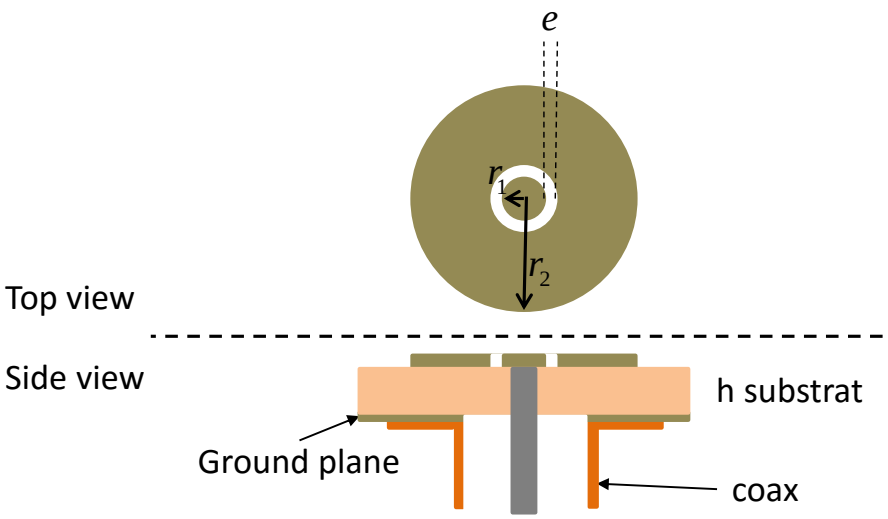

Figure 39: Structure of the cylindrical wave excitation feeder.

For a fixed substrate thickness and relative permittivity, the metasurface antenna is adapted by acting on the parameters r_1, e and r_2 of the feeder. The effects of these parameters on the antenna adaptation are presented in the next chapter.

3.6 Conclusion of the chapter

In this chapter, practical considerations in the metasurface implementation are presented.

First, the widely used cylindrical surface wave excitation was presented. The local framework definition and the impedance variation laws were described in this special case. In addition, a method for the estimation of the incident wave amplitude and phase variation was presented.

Then, the different aspects of the implementation using printed patches over a grounded dielectric substrate were presented. A new unit cell design offering an additional degree of freedom was introduced. In addition, considerations about the spatial discretization of the metasurface and the surface impedance calculation were addressed.

After that, the algorithm used for the generation of the metasurface design was sum-

marized and detailed with a flowchart and different explanation tables. The algorithm started with preliminary steps independent of the objective aperture distribution. Then, the procedure for the calculation of the impedance variation was presented. In the final step of the algorithm, the DXF of the metasurface structure is generated.

In the last part of the chapter, the feeding structure used in order to generate a cylindrical surface wave was presented. The structure consists of a circular patch with an annular slot in it. The parameters of the feeder are used in order to control the antenna adaptation.

The implementation procedure was presented in the case of cylindrical wave excitation. However, it can be generalized to other types of excitations by estimating the incident wave analytically or numerically. In addition, other structures such as multilayered substrate should be investigated.

In the next chapter, simulation results are presented. The effects of the parameters of the feeder on the antenna adaptation are studied. Then several metasurface designs with various radiation patterns are simulated with the software ANSYS Designer. The simulation results are compared with the theoretical ideal aperture field radiation pattern.

Chapter 4. Numerical Results

4.1 Introduction

In this chapter, a numerical validation of the proposed procedure through commercial software analysis is presented. In the first part of the chapter, the effects due to the variation of the feeder's geometrical parameters on the antenna impedance matching are studied by parametric analysis on HFSS.

In the second part, several antenna metasurface designs are introduced and analyzed using the software ANSYS Designer. Designs treating far-field as well as near-field radiation pattern are presented. Simulation results are compared with radiation pattern radiated by the ideal aperture field distribution and by the estimated equivalent magnetic currents above the metasurface.

4.2 Study of the parameters of the feeder:

In order to take into account the effect of the coaxial cable, the feeding structure described in the previous chapter (Figure 39) is imported in the simulation software HFSS. Figure 40 illustrates the metasurface, the feeding structure and the coaxial cable designs in HFSS.

In order to study the effect of the parameters r_1, e and r_2 of the feeder (Figure 39), a parameter-sweep simulation is performed. Due to the complexity of the structure, the analysis is performed on the central portion of the metasurface surrounded by absorbing boundary conditions. The dimensions of the portion are chosen in such a way that increasing it would not affect the scattering parameter variation. In our study, each parameter of the feeder is studied separately in order to understand its effect on the antenna matching. The simulations were performed for a Rogers TMM6 substrate of thickness h=1.27mm and relative permittivity ε_r=6.

In figure 41, the variations of the scattering parameter S_{11} in dB with respect to the frequency are presented for different values of the inner radius r_1 of the annular slot.

The simulations were performed for $r_2 = 3.7\text{mm}$ and $e = 0.25\text{mm}$. It can be seen from the figure that the variation of the parameters r_1 mainly affects the level of S_{11} at the resonance with a slight shift of the resonant frequency.

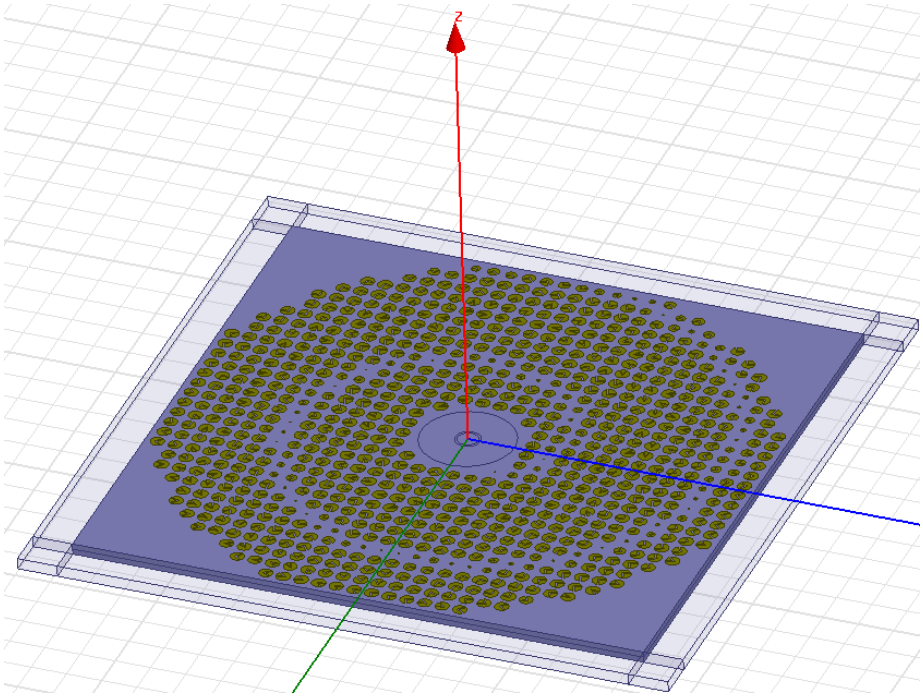

(a)

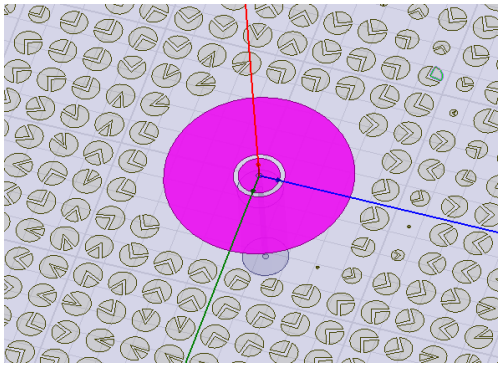

(b)

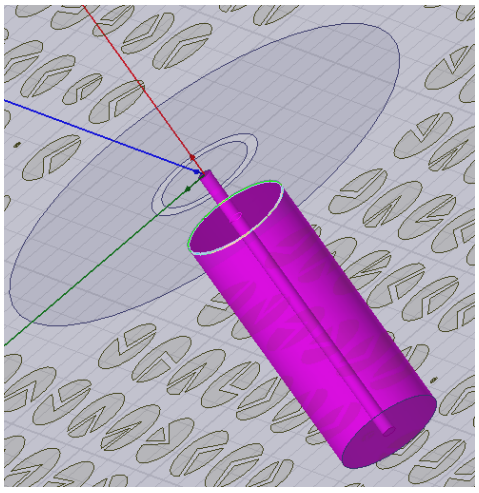

(c)

Figure 40: Simulation of the metasurface in HFSS. (a) Metasurface structure. (b) Structure of the feeder. (c) Coaxial cable modelization.

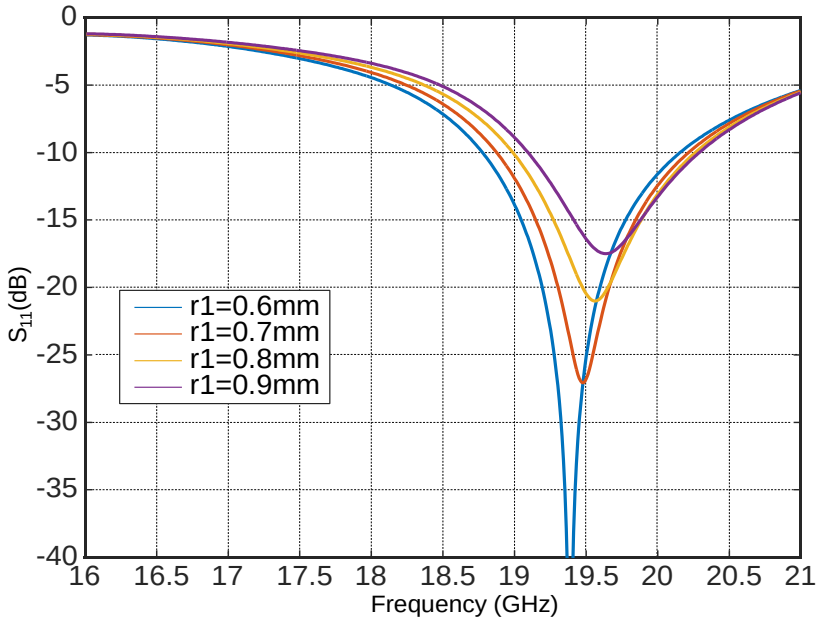

Figure 41: Variation of the scattering parameter S_{11} with respect to frequency for different values of r_1. The remaining parameters have fixed values $e = 0.25\text{mm}$ and $r_2 = 3.7\text{mm}$.

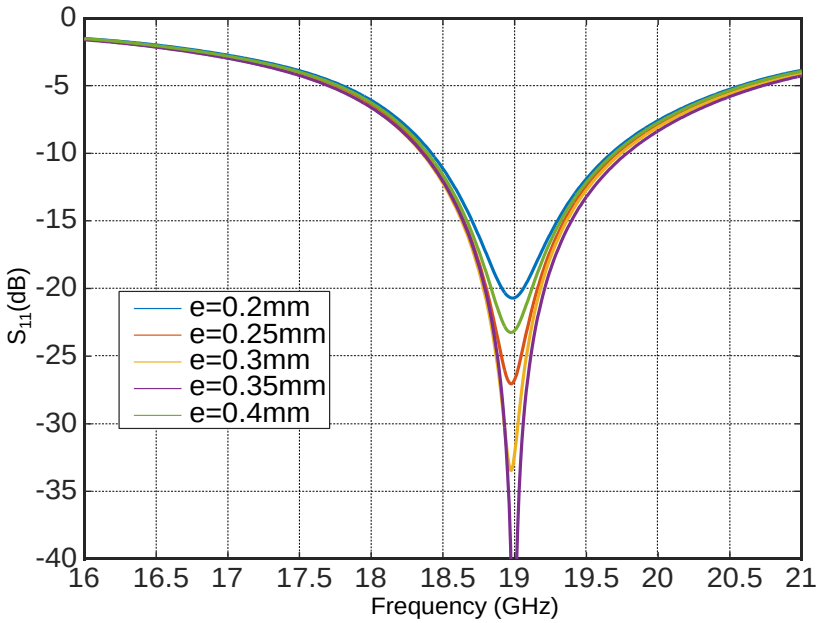

Figure 42: Variation of the scattering parameter S_{11} with respect to frequency for different values of e. The remaining parameters have fixed values $r_1 = 0.8\text{mm}$ and $r_2 = 3.8\text{mm}$.

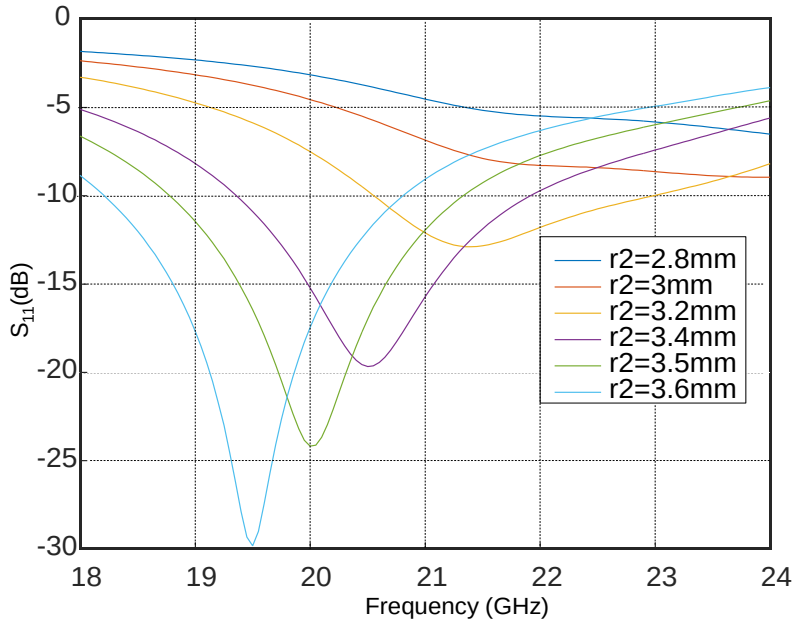

Figure 43: Variation of the scattering parameter with S_{11} respect to frequency for different values of r_2. The remaining parameters have fixed values $e = 0.25\text{mm}$ and $r_1 = 0.8\text{mm}$.

Step	Step description	Effect
1	Parameter sweep of r_2	Frequency shift + Adaptation
2	Parameter sweep of r_1	Adaptation + Small frequency shift
3	parameter sweep of e	Adaptation + No frequency shift
4	Adjuste the value of r_2	Correct the frequency shift of 1 and 2

Table 4.1: Adaptation steps of the feeder.

In figure 42, the variations of the scattering parameter S_{11} in dB with respect to the frequency are presented for different values of the width e of the annular slot. The simulations were performed for $r_2 = 3.8\text{mm}$ and $r_1 = 0.8\text{mm}$. As for r_1, the parameter

e mainly affects the level of S_{11} at the resonance. However, it has almost no effect on the resonant frequency.

Finally, figure 43 presents the variation of the scattering parameter S_{11} in dB for different values of the outer radius r_2 of the patch. The parameter sweep was performed for $e = 0.25\text{mm}$ and $r_1 = 0.8\text{mm}$. Unlike the two previous parameters, a variation of r_2 produces a shift of the resonant frequency. The step by step adaptation procedure is described in Table 4.1.

4.3 Metasurface designs

In order to validate the proposed design procedure, several metasurface antennas examples have been generated and simulated using commercial software. The obtained results are compared with :

- The theoretical far field resulting from the ideal continuous aperture field distribution. It is labelled “Ideal Aperture” in the different plots of the radiation patterns and represented in blue.
- The free-space radiation pattern of the equivalent magnetic current $\mathbf{J}(\boldsymbol{\rho}') = 2\hat{\mathbf{n}} \times \mathbf{E}_t$. This radiation pattern is obtained using the Equivalence Theorem. The magnetic currents are estimated by following the propagation path of the surface wave using the impedance values found in the database. It is labelled “Equiv Current” in the different plots of the radiation patterns and represented in red.

All the examples presented in this chapter are designed on a Rogers TMM6 substrate of relative permittivity ε_r=6 and thickness h=1.27mm. The working frequency is 20GHz. A unit cell with dimension of $\lambda/12$ is used for the metasurface while the following parameters: $(r_1; r_2; e) = (0.8; 3.5; 0.25)\,\text{mm}$ assures the antenna matching (see Figure 43 : S_{11}= -24dB).

4.3.1 Tilted beam linearly polarized antenna

The first design example is an antenna radiating a single beam at the direction $(\theta_0, \phi_0) = (30°, 0°)$ with a linear polarization along the ϕ axis (see Figure 44). A linearly polarized single beam pointing at (θ_0, ϕ_0) can be obtained by imposing the fol-

lowing objective aperture field:

$$\mathbf{E}_t^{obj}(\boldsymbol{\rho}') = e^{-jk_0(\sin\theta_0\cos\phi_0 x' + \sin\theta_0\sin\phi_0 y')}\hat{\mathbf{e}}(\phi_0) \tag{55}$$

where the amplitude is constant over the aperture and the polarization of the beam is controlled by $\hat{\mathbf{e}}(\phi_0)$ as :

$$\hat{\mathbf{e}}(\phi_0) = \begin{cases} \cos\phi_0\hat{\mathbf{x}} + \sin\phi_0\hat{\mathbf{y}} & \text{for } \hat{\boldsymbol{\theta}} \text{ polarization} \\ -\sin\phi_0\hat{\mathbf{x}} + \cos\phi_0\hat{\mathbf{y}} & \text{for } \hat{\boldsymbol{\phi}} \text{ polarization} \end{cases} \tag{56}$$

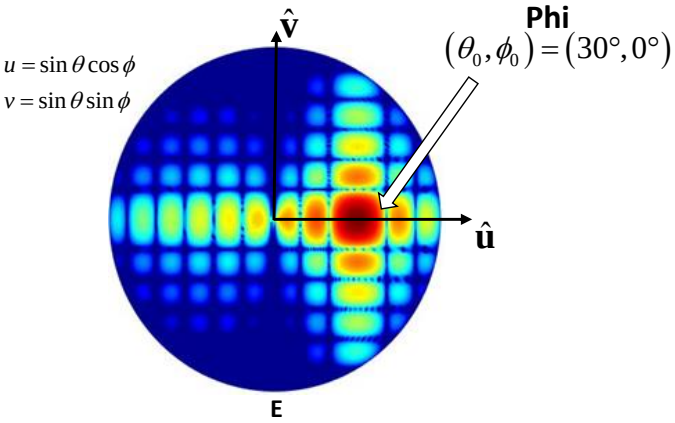

Figure 44: Objective far field radiation pattern: linearly polarized beam along the phi axis radiating in the direction $(\theta_0, \phi_0) = (30°, 0°)$.

The aperture field distribution giving the desired radiation pattern was calculated on MATLAB using equations (55) and (56). The resulting phase and amplitude distribution of this aperture field in the cylindrical coordinates are represented in figure 45. The design algorithm was then used in order to calculate, in the local framework, the reactance tensor components that are represented in figure 46.(a)-(b). The final antenna layout is composed of 3720 patches. A DXF file of the metasurface geometry was generated in order to simulate the structure. Several simulation software were investigated for the validation of the design procedure. At first, the radius of the aperture was limited to 3λ so that the metasurface could be simulated with different software. The simulations are performed in a work station Dell with a CPU Intel® CPU E5-1650 v3 with 128 Go RAM. Despite describing well the feeding structure, HFSS could not simulate structures with a radius larger than 2λ. The metasurface was then

simulated on FEKO and ANSYS Designer. The mesh quality had to be reduced in FEKO in order to perform the simulation.

Figure 47 presents the far field results obtained using ANSYS Designer and FEKO. The phi and theta components of the electric field in the $\phi = 0°$ cut-plane are represented in figure 47(a) and (b) respectively. In figure 47(c) a 3D representation of the far field radiation pattern obtained using Designer is represented.

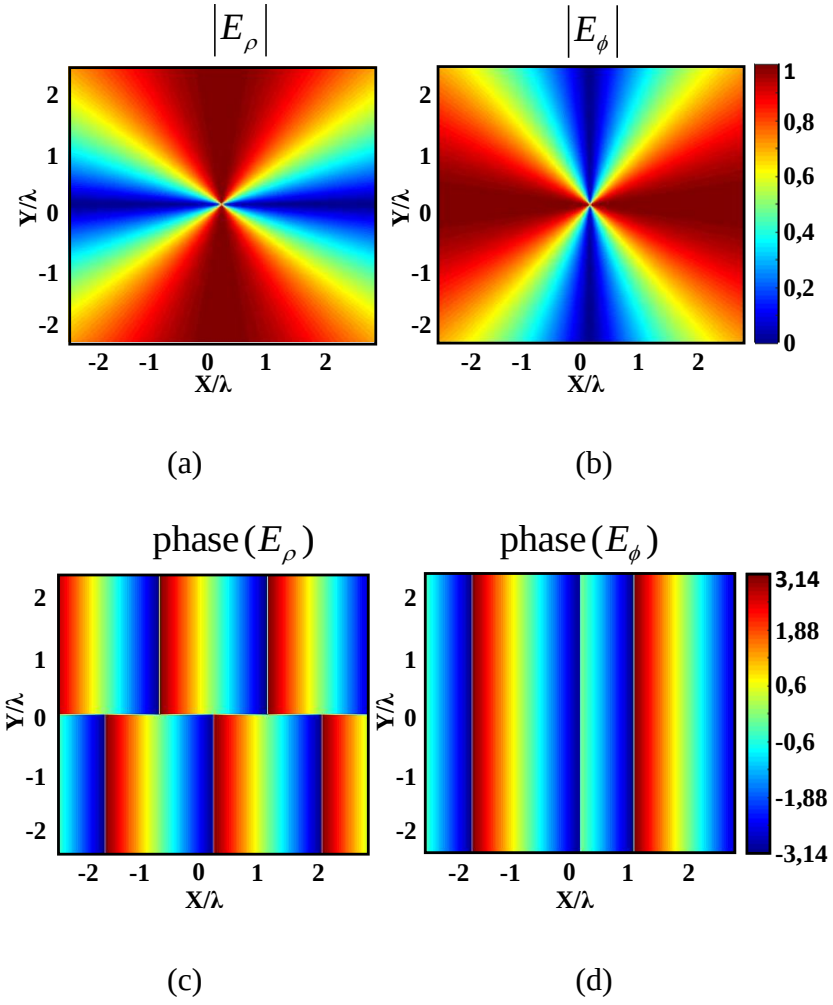

Figure 45: Aperture field distribution giving a linearly polarized beam along the phi axis in the direction $(\theta_0, \phi_0) = (30°, 0°)$. (a) $|E_\rho^{obj}|$ (b) $\arg(E_\rho^{obj})$ (c) $|E_\phi^{obj}|$ (d) $\arg(E_\phi^{obj})$.

As expected, the radiation pattern presents a tilted beam pointing at the desired direction with the desired linear polarization. The simulated beamwidth is equal to 15°.

The cross-polarization levels differ between the two software (-17dB in FEKO and –24dB in Designer). This discrepancy is probably due to the varying-quality mesh that was used in the two simulations.

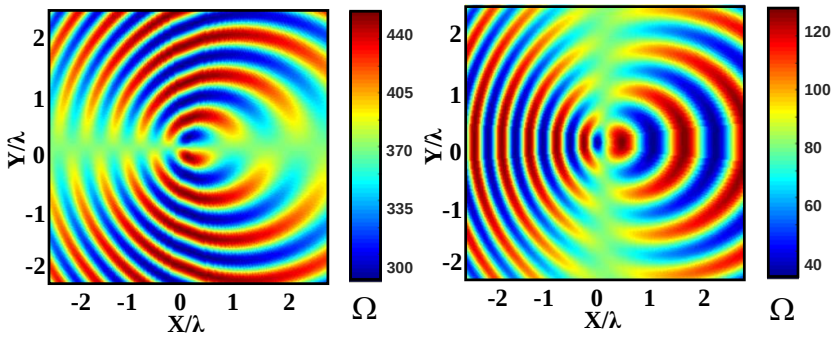

(a) (b)

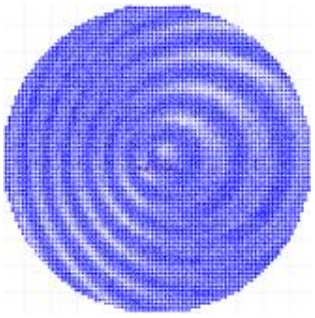

(c)

Figure 46: Generation of the metasurface design using the MATLAB Algorithm: (a) Variations of $X_{11}^{loc}(\boldsymbol{\rho}')(\Omega)$ (b) Variations of $X_{12}^{loc}(\boldsymbol{\rho}')(\Omega)$ (c) Structure of the metasurface imported in ANSYS Desinger.

The differences between the simulation and the theoretical radiation pattern may have several causes. For instance:

- The dielectric substrate is supposed infinite in the simulation software.
- The feeder does not convert all the input power into surface wave. As a result, part of this energy is radiated directly.
- The surface wave that was not converted into leaky waves may be radiated or reflected when reaching the end of the metasurface.
- The surface wave reflected at the end of the metasurface can be converted into undesired leaky waves radiating in unpredicted directions.
- The mesh quality greatly affects the value of the off-diagonal reactance com-

ponents while at the same time seriously impacting the feasibility of the simulation.

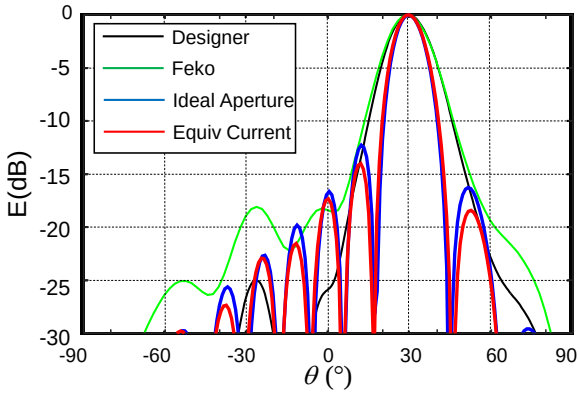

(a)

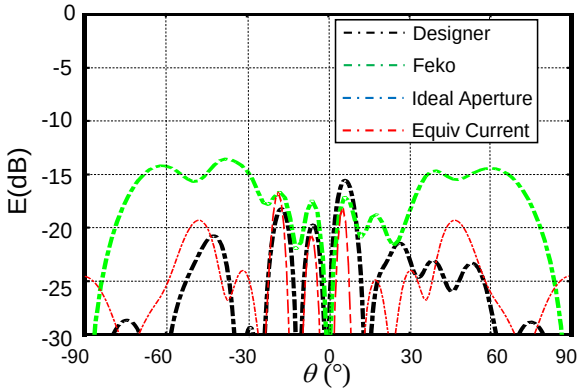

(b)

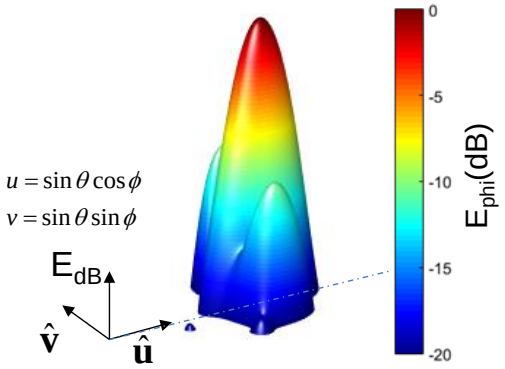

(c)

Figure 47: Far field radiation pattern (normalized) results for the linealry polarized

metasurface [27]: (a) Phi component in the $\phi = 0$ cut-plane. (b) Theta component in the $\phi = 0$ cut-plane. (c) 3D representation of the radiation pattern.

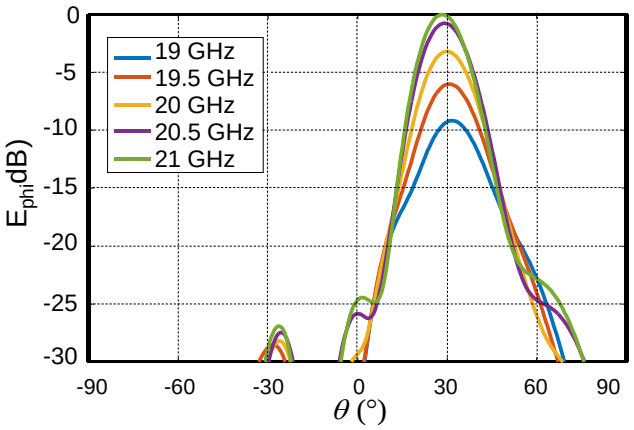

Figure 48: Phi component of the far field radiation pattern at the $\phi = 0$ cut plane for different frequencies [27].

Fig.48 represents the phi component of the radiated field in the frequency range $[19, 21]$GHz . As for any LW antennas, the beam direction deviates from the design direction θ_0 as the frequency changes. In fact, a frequency variation leads to a different value of propagation constant k_t^{sw}. This change will affect the phase of the incident wave producing a phase error (proportional to the frequency shift) in result of the holography. In addition, the variation of the propagation constant also affects the values of the impedance tensor elements.

The results of figures 47 and 48 validate the design procedure in the case of tilted beam LP radiation pattern. In order to reduce the undesired reflections at the edges of the metasurface, larger metasurfaces will be considered. Therefore, only results obtained with Ansys Designer will be presented in the upcoming examples.

4.3.2 Broadside circularly polarized antenna

The second example is a broadside circularly polarized antenna producing the pattern shown in figure 49. A circular polarization (CP) can be obtained by superposing two linearly polarized beams with orthogonal polarization and $\frac{\pi}{2}$ phase shift. Thus, the relative aperture field distribution is given by

$$\mathbf{E}_t^{obj}(\boldsymbol{\rho}') = \left(1/\sqrt{2}\right)\left(\hat{\mathbf{x}} + j\hat{\mathbf{y}}\right) \tag{57}$$

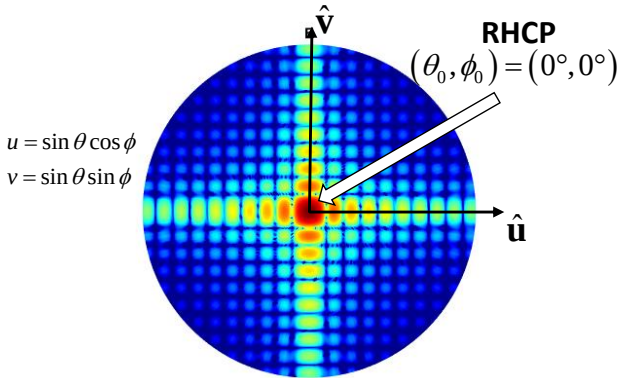

Figure 49: Objective far field radiation pattern: right hand circularly polarized beam radiating at broadside $(\theta_0, \phi_0) = (0°, 0°)$.

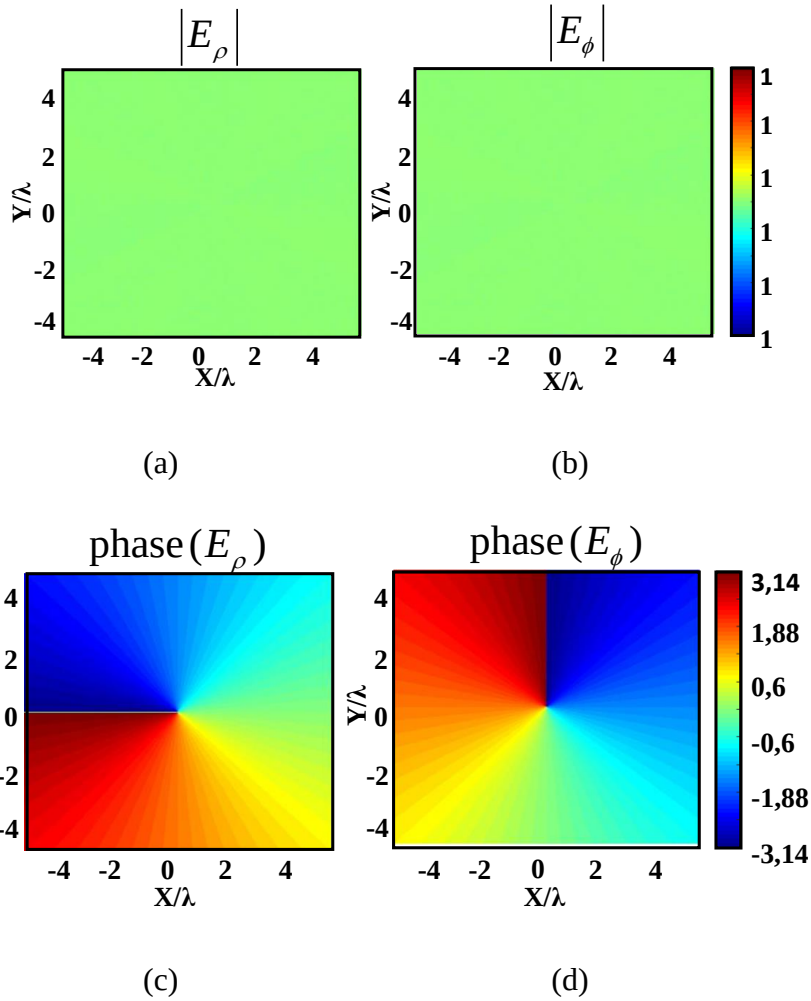

Figure 50: Aperture field distribution giving a right hand circularly polarized beam at broadside. a) $|E_\rho^{obj}|$; (b) $|E_\phi^{obj}|$ (c) $\arg(E_\rho^{obj})$; (d) $\arg(E_\phi^{obj})$.

The corresponding aperture field distribution was calculated in MATLAB for a metasurface of radius 5λ . The phase and amplitude of aperture field in the cylindrical coordinates are represented in figure 50.

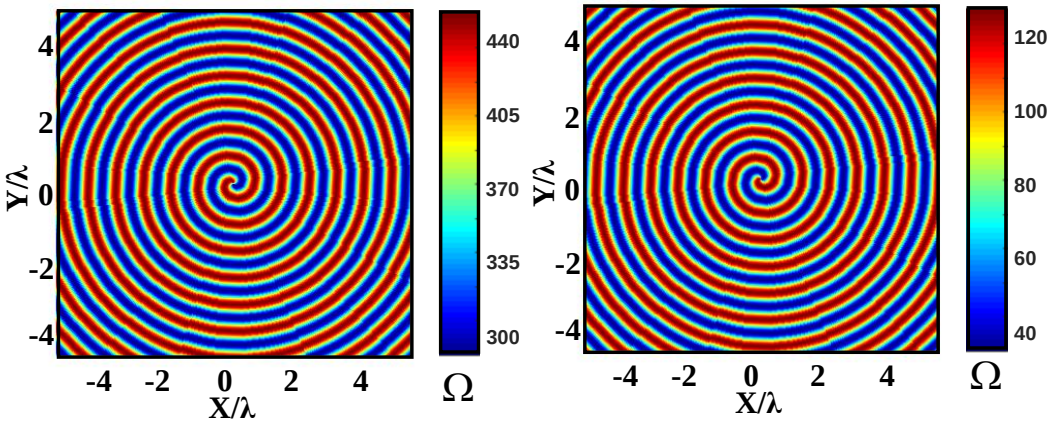

(a) (b)

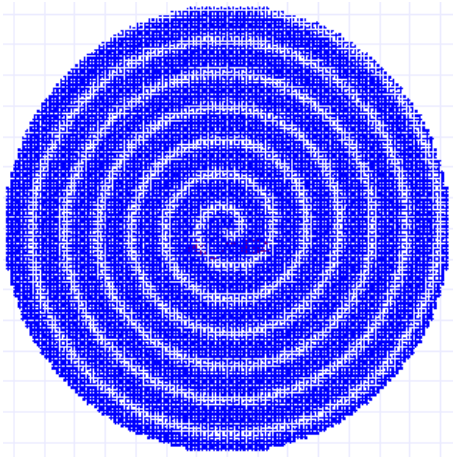

(c)

Figure 51: Generation of the broadside RHCP metasurface using the MATLAB Algorithm: (a) Variations of $X_{11}^{loc}(\boldsymbol{\rho}')(\Omega)$ (b) Variations of $X_{12}^{loc}(\boldsymbol{\rho}')(\Omega)$ (c) Structure of the metasurface imported in ANSYS Desinger.

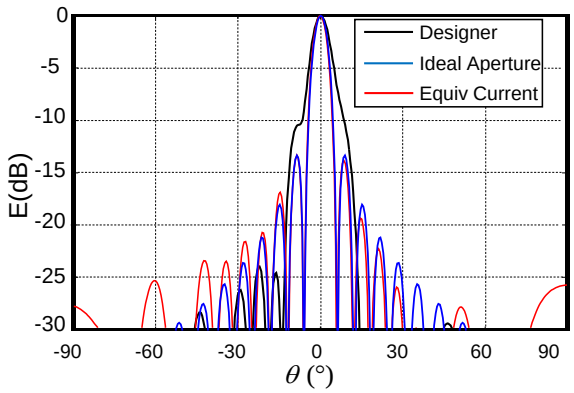

(a)

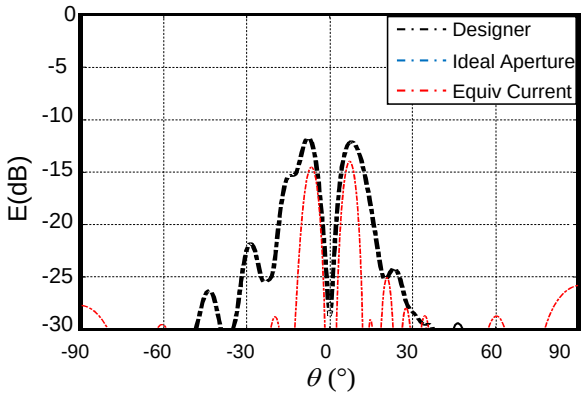

(b)

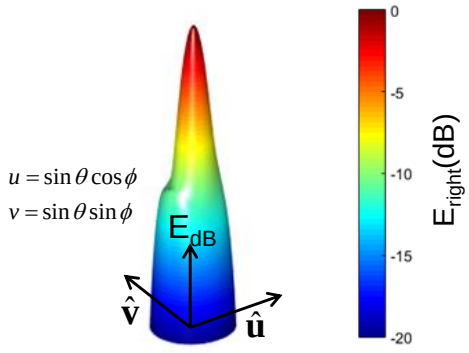

(c)

Figure 52: Far field radiation pattern (normalized) results for the broadside RHCP metasurface [27]: (a) RHCP component in the $\phi = 0°$ cut-plane. (b) LHCP component in the $\phi = 0°$ cut-plane. (c) 3D representation of the radiation pattern.

In figure 51.(a)-(b), the corresponding reactance tensor components are represented in the local framework. The DXF of the metasurface was then generated and imported in ANSYS Designer (figure 51.(c)) in order to simulate the structure. The final antenna layout is composed of 10732 patches.

Figure 52 represents the far field radiation pattern. The RHCP and the LHCP components in the $\phi = 0$ cut-plane are represented in figure 52.(a) and (b), respectively. The 3D radiation pattern is represented in figure 52.(c). It can be seen from the figure that the radiation pattern corresponds the predicted broadside RHCP radiation. In addition, a good agreement is obtained between the simulation and the theoretical results. The simulated beamwidth is equal to 8° with a side lobe level of –12dB. A better agreement can be obtained by further increasing the antenna dimensions to diminish the undesired edges reflections. The results given in figure 52 validate the metasurface design procedure in the case of broadside RHCP radiation pattern.

4.3.3 Multi-beam metasurface antenna:

As a third example, we consider a metasurface antenna radiating multiple beams. In order to obtain a multi-beam radiation pattern, we propose to superpose the aperture field distribution corresponding to each beam. This leads to [27]-[30]:

$$\mathbf{E}_t^{obj}(\boldsymbol{\rho}') = \frac{1}{N_{beams}} \sum_{k=1}^{N_{beams}} \mathbf{E}_t^{k}(\boldsymbol{\rho}') \tag{58}$$

where

N_{beams} is the number of beams.

$\mathbf{E}_t^{k}(\boldsymbol{\rho}')$ is the objective field corresponding to each individual beam.

In this report, two examples of multi-beam metasurface antennas are presented. The first antenna radiates two beams with different polarizations. The second antenna has a more complex radiation pattern of four beams radiating in different directions with different types of polarizations. For each antenna, the objective aperture distribution is calculated using equation (58) by variating the number of beams and the nature of their polarization.

4.3.3.1 Two beams antenna

The first multi-beam antenna example that we considered is a metasurface radiating two beams (Figure 53) with the following characteristics:

- Beam 1: A LP beam along the phi axis radiating in the direction $(\theta_1, \phi_1) = (30°, 0°)$.
- Beam 2: A RHCP beam radiating in the direction $(\theta_2, \phi_2) = (45°, 135°)$.

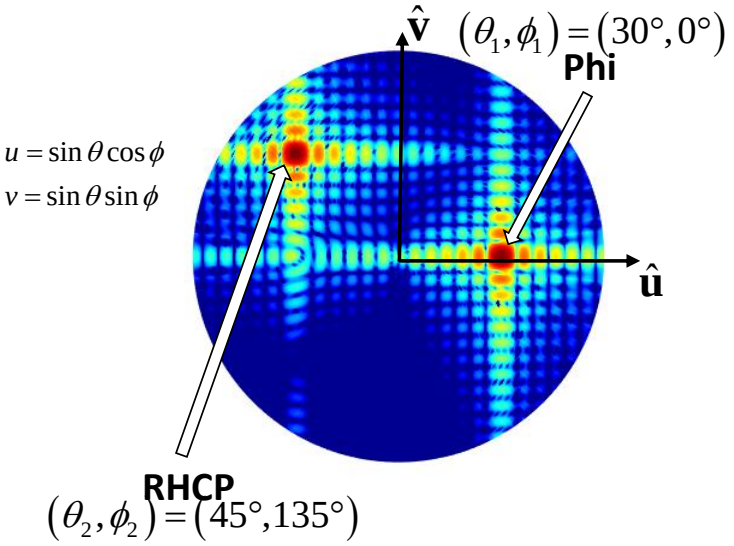

Figure 53: Objective far field radiation pattern: two beams radiation pattern.

The aperture field distribution generating the radiation pattern described in figure 53 was calculated using equation (58). The phase and amplitude of the objective distribution in the cylindrical coordinates are represented in figure 54. Figures 55.(a) and (b) present the metasurface's reactance components variations in the local framework. The final metasurface design imported in Designer is represented in figure 55.(c)

Figure 56 presents the far field radiation pattern results obtained using Designer. The figure 56.(a) presents the linear components in the $\phi = 0°$ cut-plane. The theta components are represented in solid lines while the phi components are represented in solid lines. Figure 56.(b) gives the circular components in the $\phi = 135°$ cut-plane. The RHCP components are represented in solid lines while the LHCP components are represented in dashed lines. The 3D representation of the total field is given in figure 56.(c).

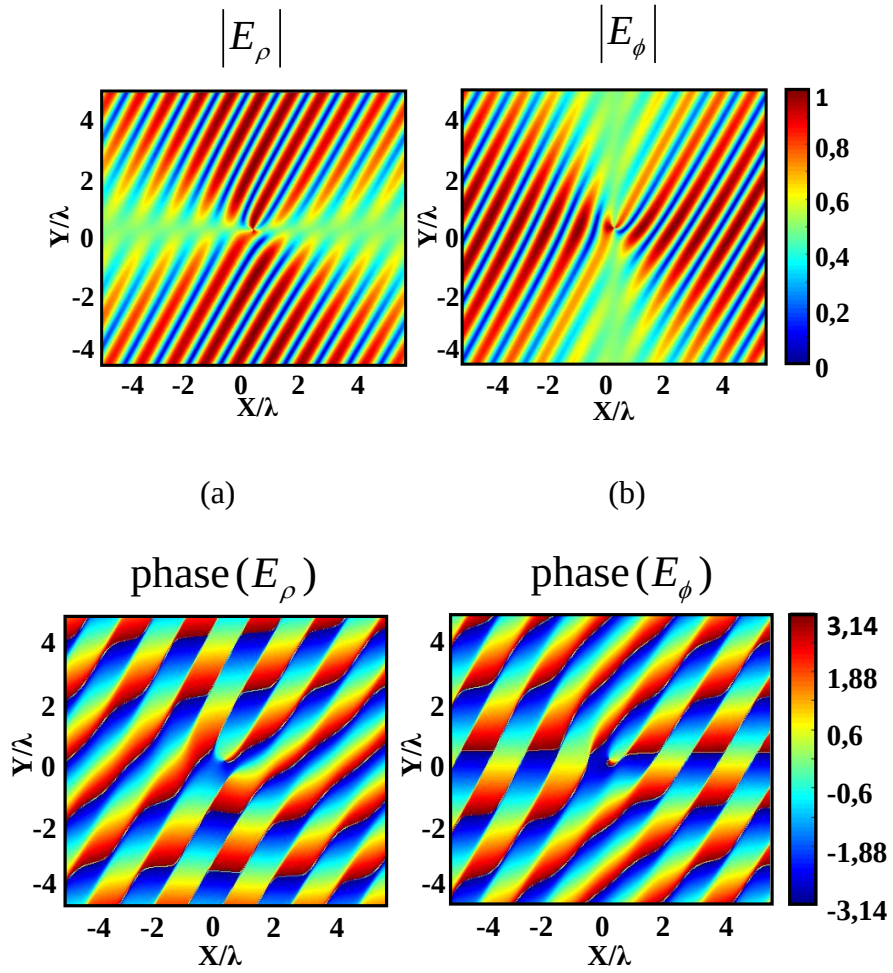

Figure 54: Aperture field distribution giving a two beams radiation pattern. a) $\left|E_\rho^{obj}\right|$; (b) $\left|E_\phi^{obj}\right|$ (c) $\arg(E_\rho^{obj})$; (d) $\arg(E_\phi^{obj})$.

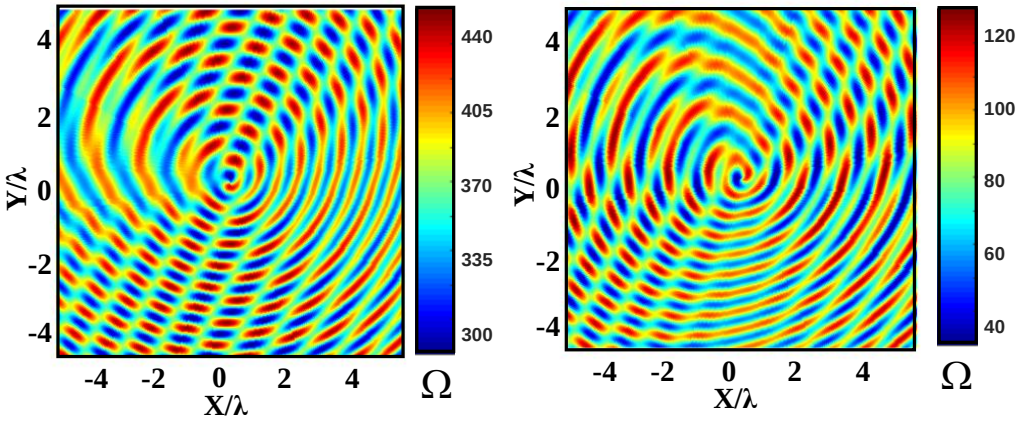

(a) (b)

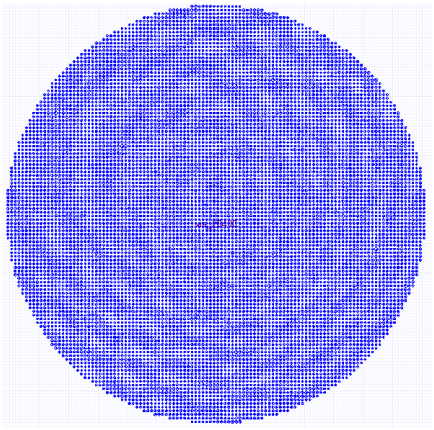

(c)

Figure 55: Generation of the two beams metasurface using the MATLAB Algorithm: (a) Variations of $X_{11}^{loc}(\boldsymbol{\rho}')(\Omega)$ (b) Variations of $X_{12}^{loc}(\boldsymbol{\rho}')(\Omega)$ (c) Structure of the metasurface imported in ANSYS Desinger.

It can be seen from the figure 56 that the radiation pattern corresponds to the desired multi-beam behavior. The two radiated beams propagates in the expected directions ($(\theta_1,\phi_1)=(30°,0°)$ and $(\theta_2,\phi_2)=(45°,135°)$) and have the desired linear and circular polarizations respectively. The beamwidths are equal to 8° and 13° for the first and the second beams respectively. The SLL is lower than -20dB. This example validates the idea of superposing multiple aperture distributions (one for each beam) in order to obtain the multi-beam behavior.

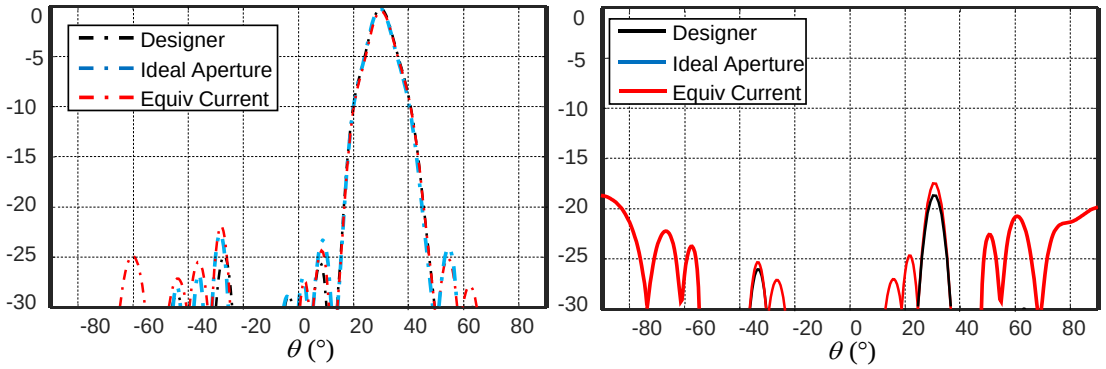

(a)

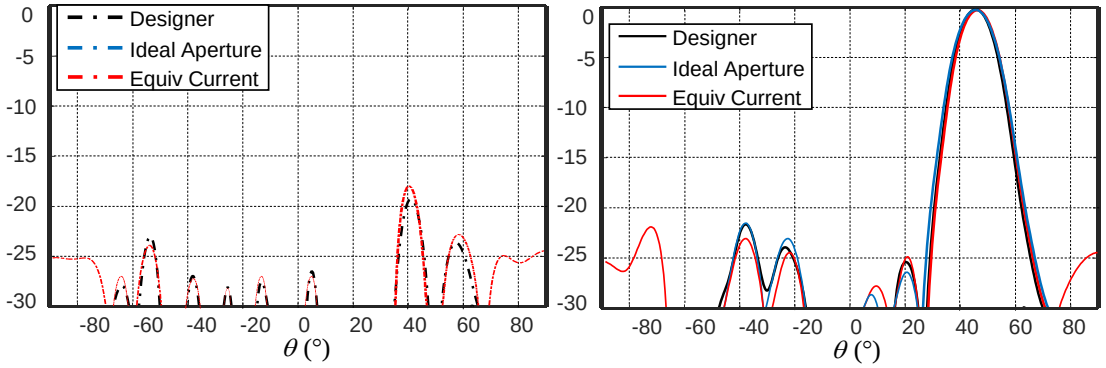

(b)

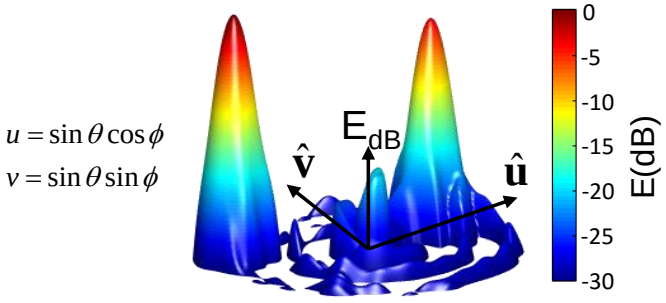

(c)

Figure 56: Far field radiation pattern (normalized) results for the two beams metasurface [29]-[30]: (a) Linear components in the $\phi = 0$ cut-plane. The theta components are represented in solid lines while the phi components are represented in solid lines (b) Circular components in the $\phi = 135$ cut-plane. The RHCP components are represented in solid lines while the LHCP components are represented in dashed lines (c) 3D representation of the radiation pattern.

4.3.3.2 Four beams antenna

As a further validation of the multi-beam design approach, a more complex objective radiation pattern is considered (Figure 57). In this example, the considered metasurface radiates four beams with the following characteristics [27]:

- Beam 1: A LP beam along the phi axis radiating in the direction $(\theta_1, \phi_1) = (30°, 0°)$.
- Beam 2: A LP beam along the theta axis radiating in the direction $(\theta_2, \phi_2) = (45°, 180°)$.
- Beam 3: A RHCP beam radiating in the direction $(\theta_3, \phi_3) = (45°, 270°)$.
- Beam 4: A LHCP beam radiating in the direction $(\theta_4, \phi_4) = (30°, 90°)$.

This choice is motivated by the fact that the four beams have all the possible polarization states. In addition, the different directions of the beams add up to the complexity of the problem.

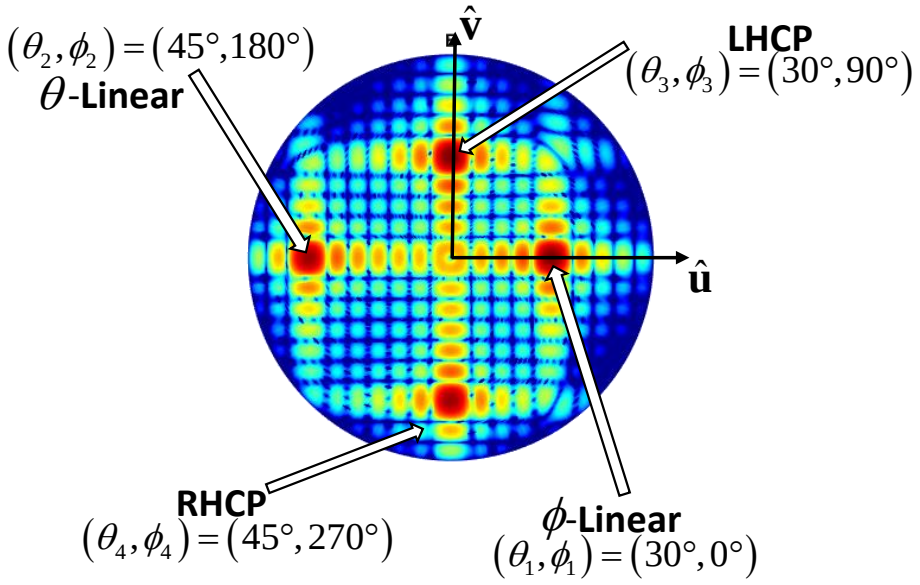

Figure 57: Objective far field radiation pattern: four beams radiation pattern with different directions and polarizations.

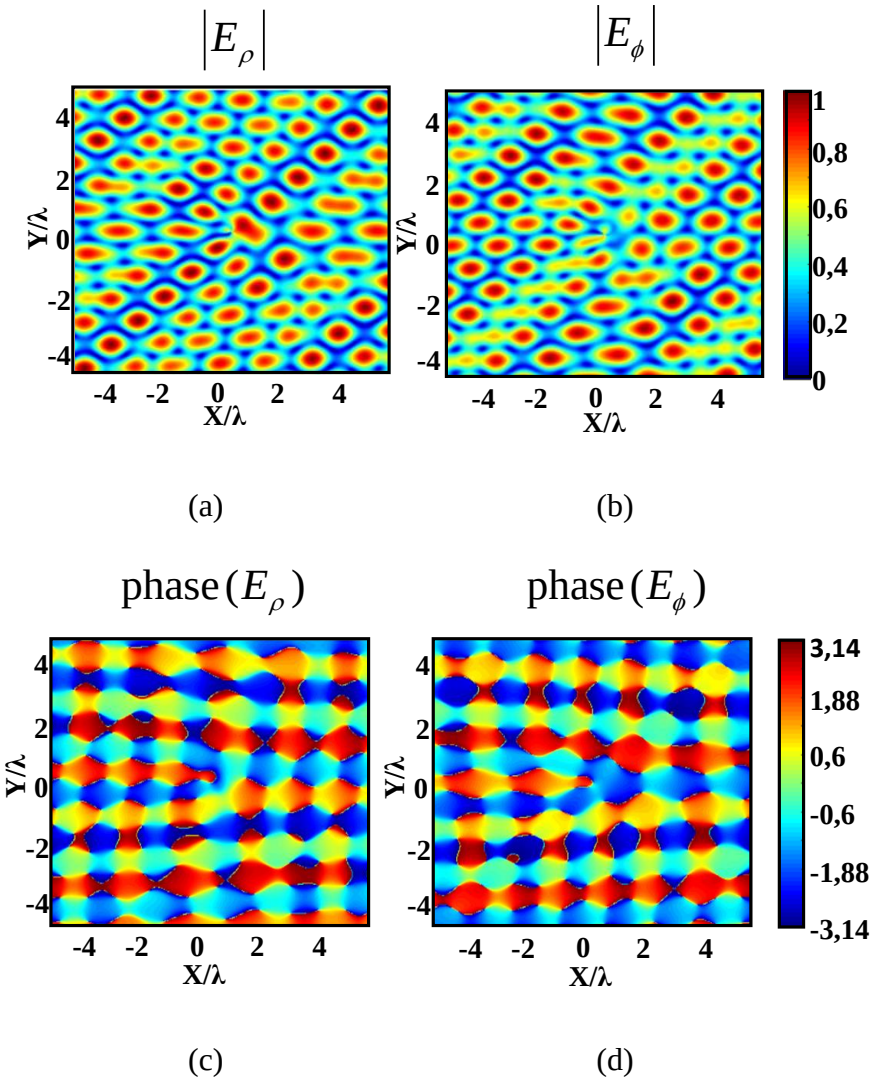

Figure 58: Aperture field distribution giving a four beams radiation pattern. a) $\left|E_\rho^{obj}\right|$; (b) $\left|E_\phi^{obj}\right|$ (c) $\arg(E_\rho^{obj})$; (d) $\arg(E_\phi^{obj})$.

As for the two beams case, the aperture field generating the four beam radiation pattern was calculated using equation (58). The phase and amplitude of the aperture distribution in the cylindrical coordinates are depicted in figure 58. The metasurface design algorithm was then used in order to calculate the reactance component variation in the local framework (figure 59.(a)-(b)). The corresponding metasurface structure is represented in figure 59.(c). From figures 58 and 59, it is noteworthy that a strict control of the amplitude and phase distribution is needed to obtain the desired multi-beam radiation.

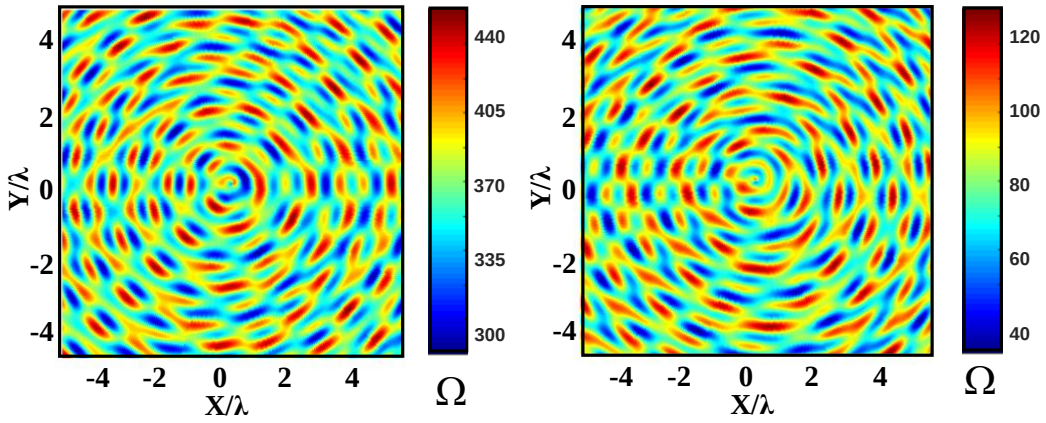

(a) (b)

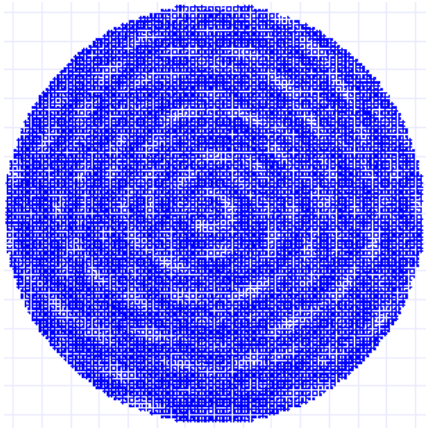

(c)

Figure 59: Generation of the four beams metasurface using the MATLAB Algorithm: (a) Variations of $X_{11}^{loc}(\boldsymbol{\rho}')(\Omega)$ (b) Variations of $X_{12}^{loc}(\boldsymbol{\rho}')(\Omega)$ (c) Structure of the metasurface imported in ANSYS Desinger.

Figure 60 presents the results of the far field radiation pattern provided by Designer. The figure 60.(a) presents the linear components in the $\phi = 0°$ cut-plane. The theta components are represented in dashed lines while the phi components are represented in solid lines. Figure 60.(b) gives the circular components in the $\phi = 90°$ cut-plane. The RHCP components are represented in solid lines while the LHCP components are represented in dashed lines. The 3D representation of the total field is given in figure 60.(c).

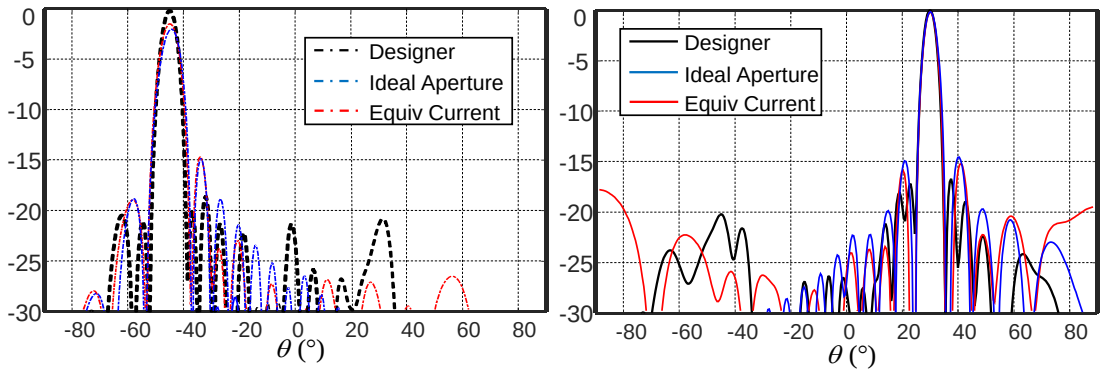

(a)

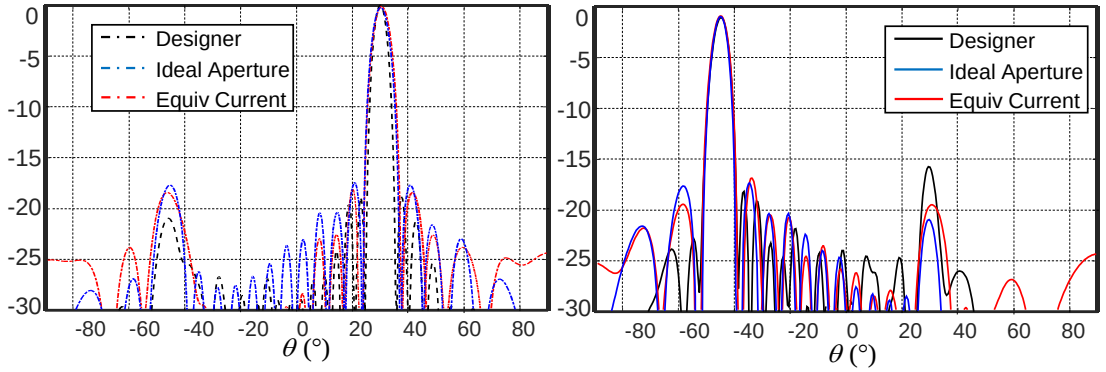

(b)

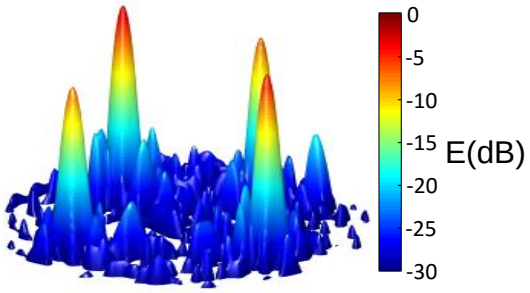

(c)

Figure 60: Far field radiation pattern (normalized) results for the four beam metasurface [27]-[28]: (a) Linear components in the $\phi = 0°$ cut-plane. The theta components are represented in dashed lines while the phi components are represented in solid lines (b) Circular components in the $\phi = 90°$ cut-plane. The RHCP components are represented in solid lines while the LHCP components are represented in dashed lines (c) 3D representation of the radiation pattern.

It can be seen from the figure 60 that the radiated pattern corresponds to the desired multi-beam behavior. In the in the $\phi = 0°$ cut-plane, two beams with the desired linear polarizations are radiated in the expected directions ($(\theta_1, \phi_1) = (30°, 0°)$ and $(\theta_2, \phi_2) = (45°, 180°)$) with a beamwidth equal to 8° for both beams. In the $\phi = 90°$ cut-plane, two beams with the desired circular polarizations are radiated in the expected directions ($(\theta_3, \phi_3) = (45°, 270°)$ and $(\theta_4, \phi_4) = (30°, 90°)$) with a beamwidth equal to 8° for both beams. The cross-polarization levels and the side lobe levels are smaller than -15dB for all the four beams.

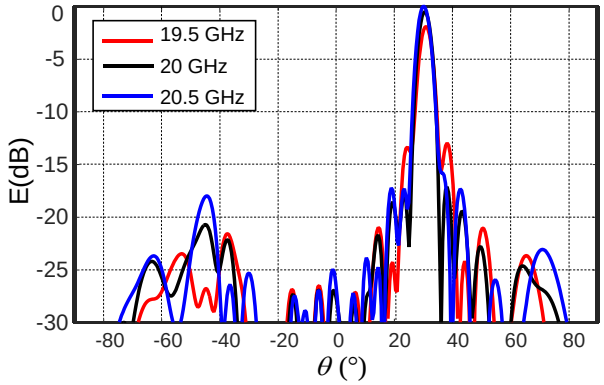

(a)

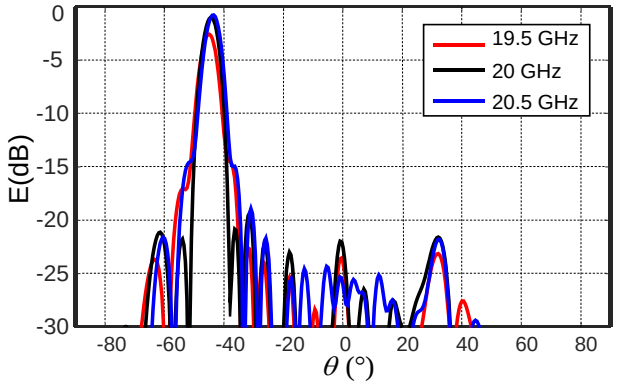

(b)

Figure 61: Variations of the multi-beam radiation pattern with respect to frequency for the $\phi = 0°$ cut-plane [27]. (a) Theta components. (b) Phi components. The considered frequencies are: 19.5 GHz (in red), 20GHz (in black) and 20.5GHz (in blue). The radiation pattern was normalized with respect to the maximum beam amplitude.

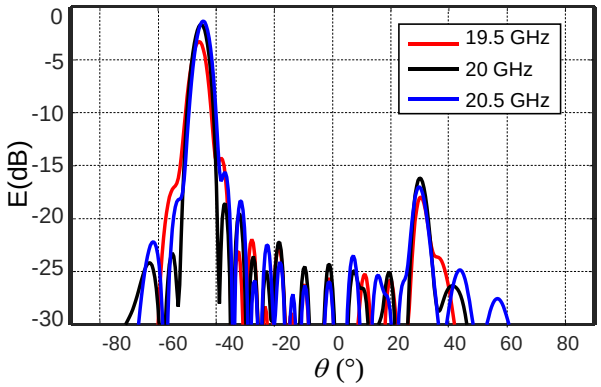

(a)

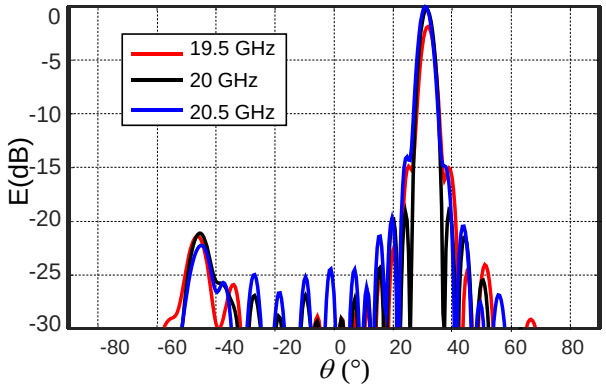

(b)

Figure 62: Variations of the multi-beam radiation pattern with respect to frequency for the $\phi = 90°$ cut-plane [27]. (a) RHCP components. (b) LHCP components. The considered frequencies are: 19.5 GHz (in red), 20GHz (in black) and 20.5GHz (in blue). The radiation pattern was normalized with respect to the maximum beam amplitude.

For this complex radiation pattern, the metasurface was simulated for different frequencies. Figure 61 shows the frequency behavior of the two linearly polarized beams presents in the $\phi = 0°$ cut-plane. Figure 62 gives the frequency behavior of the two circularly polarized beams presents in the $\phi = 90°$ cut-plane. The radiation patterns were simulated for the frequencies 19.5 GHz (in red), 20GHz (in black) and 20.5 GHz (in blue). It can be seen from the figure that the radiation performances (side lobe levels and cross polarization levels) are stable in the considered frequency band.

In view of the diversity of the realized radiation pattern and the complexity of the

achieved multi-beam radiation patterns, these results confirm that the proposed method is able to implement general radiating aperture field distributions.

4.3.4 Flat top circularly polarized antenna

In this section, we implement a flat-top RHCP radiation pattern. For this kind of antennas, often used in satellite applications, the normalized radiation pattern F_n is relatively constant within a desired angle range while it is below a certain threshold outside of this region.

The desired radiation pattern can then be described by the following equation

$$\left\| F_n(\theta) \right\| = \begin{cases} 1 \pm \delta & \text{if } |\theta| < \theta_f \\ < \tau & \text{if } |\theta| > \theta_f \end{cases} \tag{59}$$

where

δ is the maximum oscillation with respect to the desired level.

$\tau < 1$ is the threshold.

θ_f defines the angular region of interest.

To generate the radiation pattern of the form (59) with RHCP, we proposed a new aperture distribution consisting of multiplying the bi-dimensional inverse Fourier transform of characteristic function of a circular disc [40] by the term $(\hat{\mathbf{x}} + i\hat{\mathbf{y}})$. The final objective aperture field distribution is given by [27]:

$$\mathbf{E}_t^{obj}(\boldsymbol{\rho}') = \frac{1}{\sqrt{2}}(\hat{\mathbf{x}} + i\hat{\mathbf{y}}) \frac{J_1(k_0 \rho' \sin\theta_f)}{k_0 \rho' \sin\theta_f} \tag{60}$$

where

J_1 is the first order Bessel function of the first kind.

For a flat top of angle $\theta_f = 20°$, the metasurface design algorithm produces the reactance component variation shown in figure 63.(a)-(b) (local framework). The corresponding geometry is represented in figure 63.(c). The far field radiation pattern was simulated using Designer and the results are represented in figure 64. Figures 64.(a)

and (b) show the far field radiation pattern for the RHCP and LHCP components in the $\phi = 0°$ cut-plane, where figure 64.(c) presents the 3D radiation pattern. It can be seen from the figure 64 that, for angles $\theta < \theta_f$, a RHCP radiation pattern is obtained with a relatively constant amplitude of oscillations $\delta = \pm 1\text{dB}$. In addition, the simulation results are in close agreement with the theoretical results. As a result, we can consider that beam shaping is achievable using the proposed design procedure.

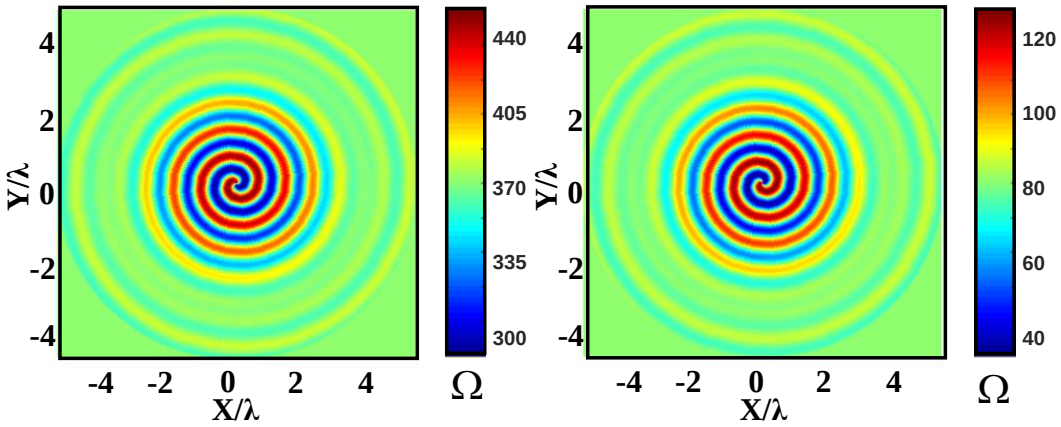

(a) (b)

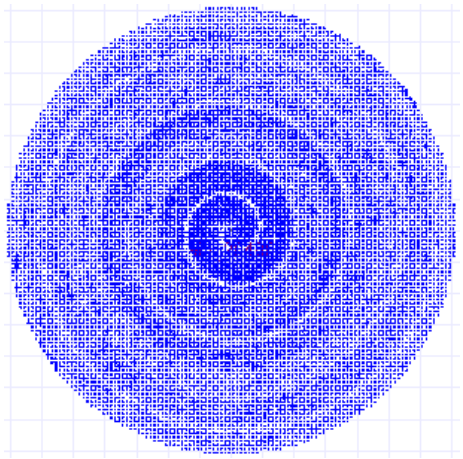

(c)

Figure 63: Generation of the two beam metasurface using the MATLAB Algorithm: (a) Variations of $X_{11}^{loc}(\boldsymbol{\rho}')(\Omega)$ (b) Variations of $X_{12}^{loc}(\boldsymbol{\rho}')(\Omega)$ (c) Structure of the metasurface imported in ANSYS Desinger.

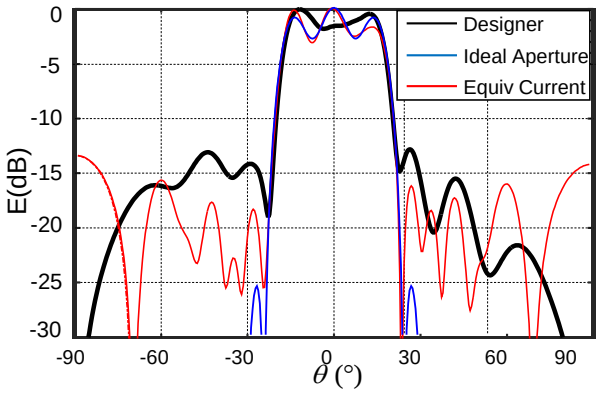

(a)

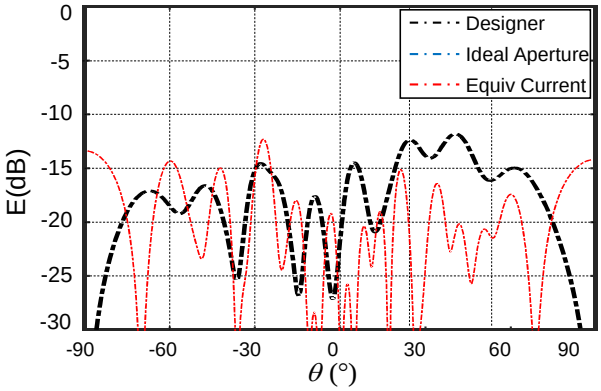

(b)

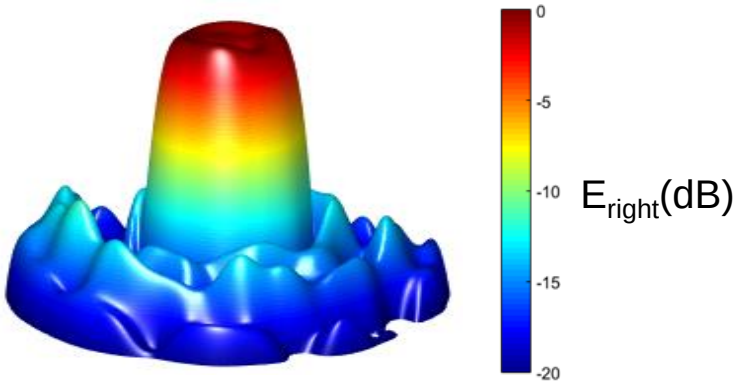

(c)

Figure 64: Far field radiation pattern (normalized) results for the broadside RHCP metasurface [27]: (a) RHCP component in the $\phi = 0°$ cut-plane. (b) LHCP component in the $\phi = 0°$ cut-plane. (c) 3D representation of the radiation pattern.

4.3.5 Near field multi-beam focusing antenna

After validation of the design procedure for far field patterns, the control of the near field is investigated. As our design procedure allows the control of the aperture field distributions, it can be used for near-field applications using appropriate objective aperture distributions. In this section, an example of near field multi-beam focusing antenna is presented.

4.3.5.1 Metasurface design

We consider a metasurface that focuses four beams in a horizontal plane parallel to the antenna placed at a distance of $z = 5\lambda$ (see figure 65).

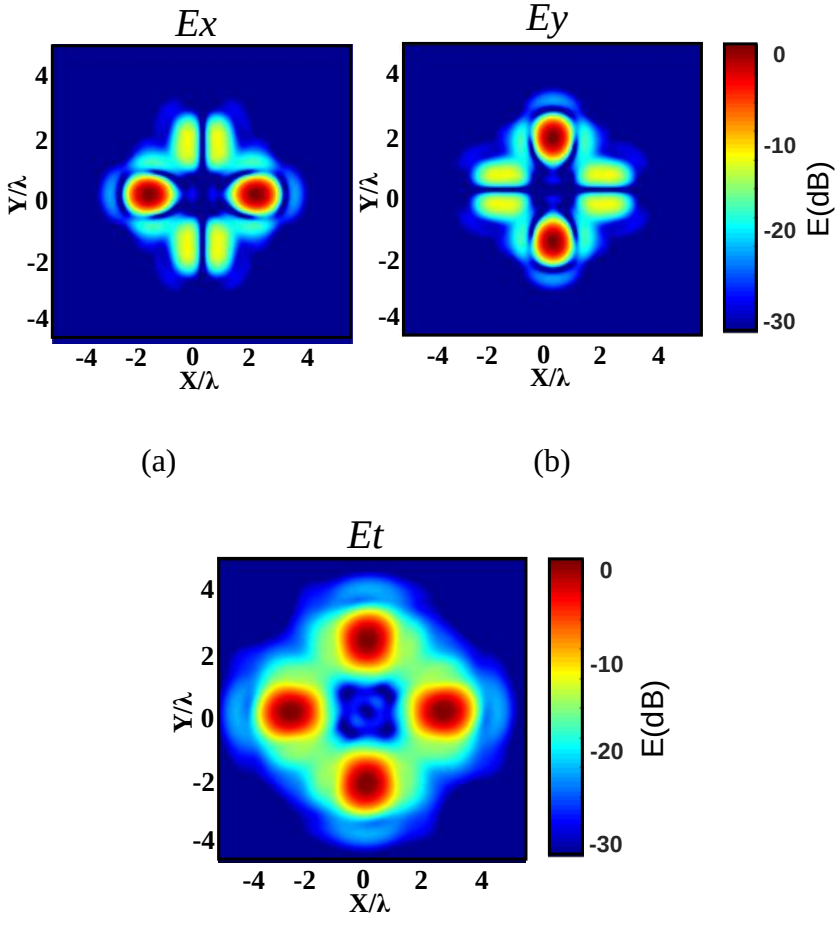

(a) (b)

(c)

Figure 65: Objective near field radiation pattern at the height $z = 5\lambda$. (a) Ex component. (b) Ey component. (c) Total field Et.

The metasurface was designed in collaboration with the IETR laboratory of the University of Rennes1. The objective aperture field distribution was calculated by our partners from the IETR laboratory [41]-[42]. The Cartesian components of the aperture field are represented in figure 66.

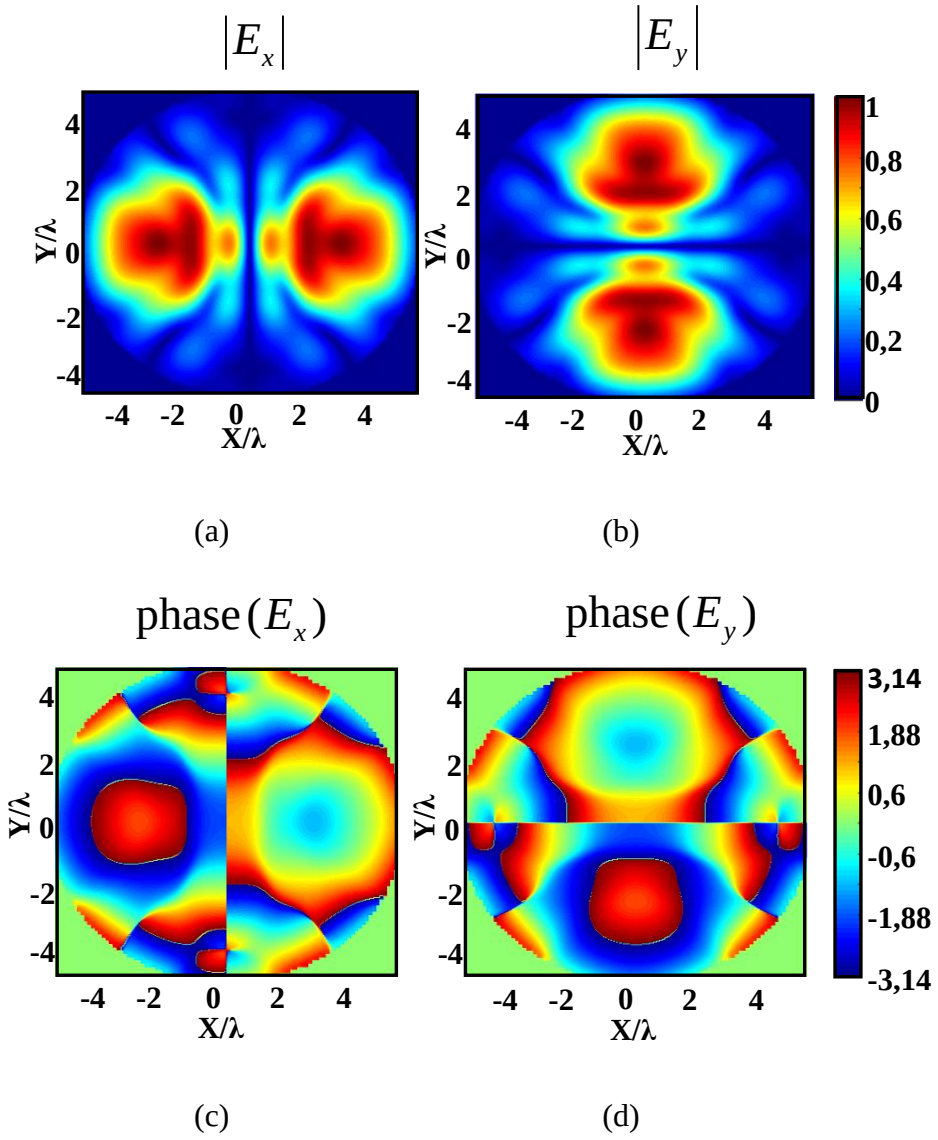

Figure 66: Aperture field distribution giving the four beams near field focusing [41] - [42]. a) $\left|E_x^{obj}\right|$; (b) $\left|E_y^{obj}\right|$ (c) $\arg(E_x^{obj})$; (d) $\arg(E_y^{obj})$.

The aperture field distribution given in figure 66 was then imported in the metasurface design algorithm to generate the corresponding reactance component variation in the local framework (figure 67.(a)-(b)). The corresponding metasurface structure is represented in figure 67.(c).

The near field radiation pattern was then simulated in Designer. In figure 68 a horizontal cut at a height $z = 5\lambda$ is represented. It can be seen from the figure that the beam focusing behavior is obtained at the desired height with the expected polarization (along x for two beams and along y for the two other beams). The beamwidth is equal to 0.63λ with side lobe levels around -15dB.

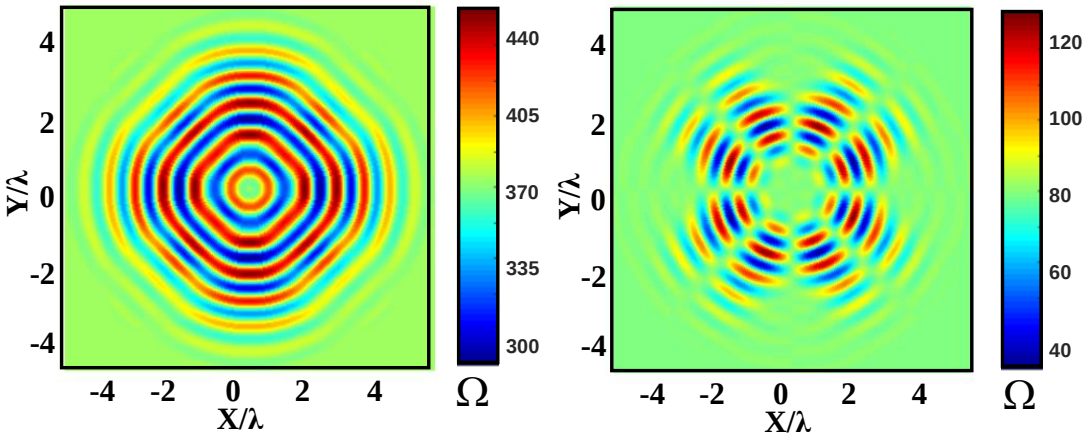

(a) (b)

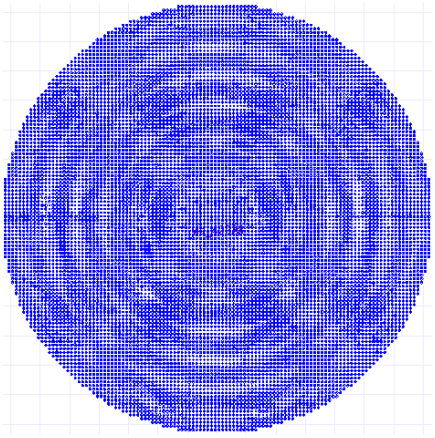

(c)

Figure 67: Generation of the four-beams near field focusing metasurface using the MATLAB Algorithm: (a) Variations of $X_{11}^{loc}(\boldsymbol{\rho}')(\Omega)$ (b) Variations of $X_{12}^{loc}(\boldsymbol{\rho}')(\Omega)$ (c) Structure of the metasurface imported in ANSYS Desinger.

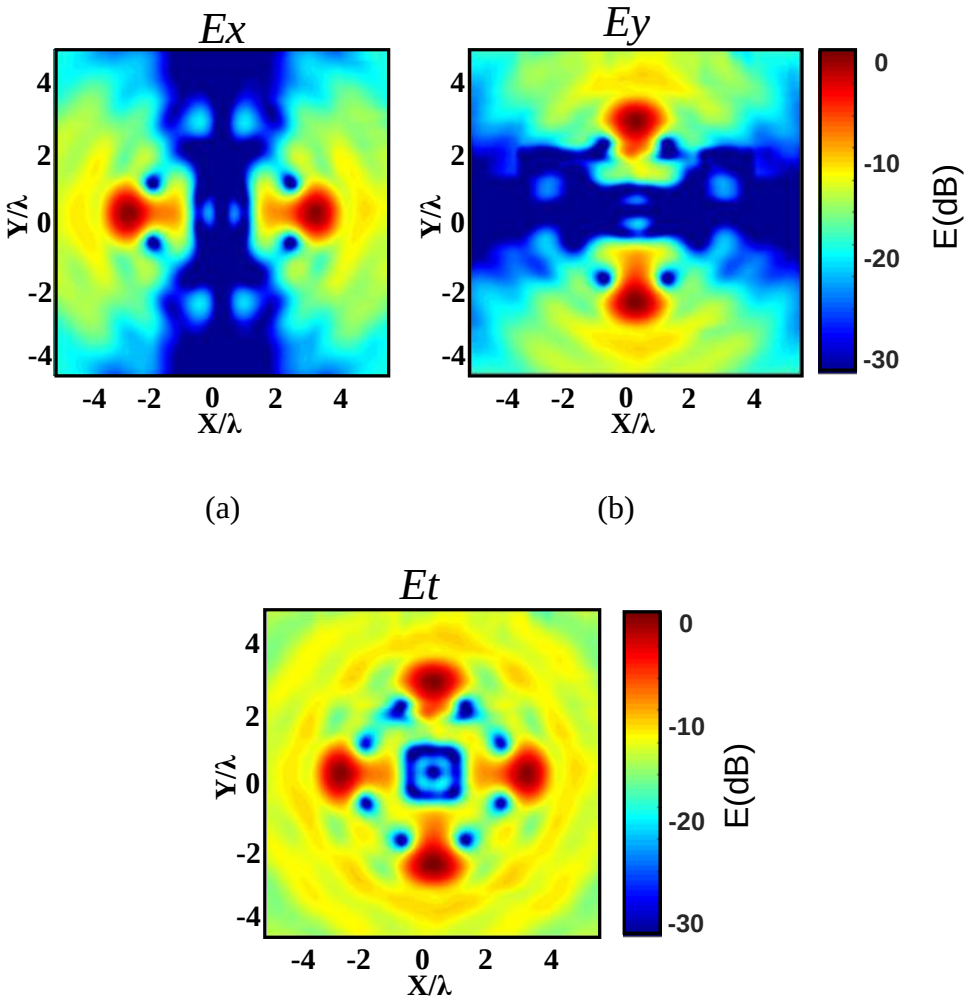

(a) (b)

(c)

Figure 68: Simulated near field horizontal cut-plane in ANSYS Designer at the height $z = 5\lambda$. (a) Ex component. (b) Ey component. (c) Total field Et.

In figure 69, the vertical cut-planes of the near field pattern are presented. Figure 69.(a) gives the Ex component in the XZ plane while figure 69.(b) gives the Ey component in the YZ plane. It can be seen from the figures that the field is focused in the two planes when propagating away from the metasurface. In addition, we notice high level of the field near the metasurface, especially at its center. These elevated levels of the field are probably due near field radiated by the feeder. This is due to the fact that not all the energy injected in the feeder is converted into surface waves.

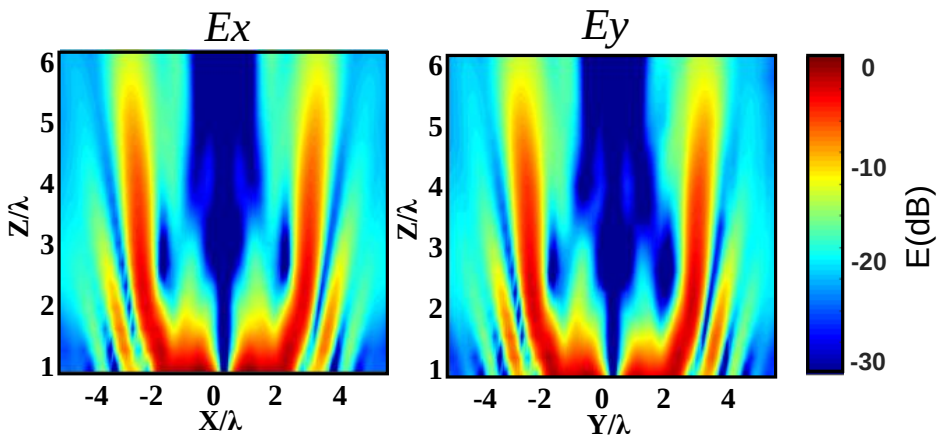

Figure 69: Simulated near field vertical cut-plane in ANSYS Designer. (a) Ex component in the XZ plane. (b) Ey component in the YZ plane.

4.3.5.2 Feeder effect cancellation

In order to investigate the effect of the feeder on the radiation pattern, a non-modulated metasurface is designed and imported on Designer. As the metasurface is not modulated, no leaky wave component is radiated. Thus, the radiated field above the metasurface is mainly due to the effect of the feeder in presence of the metasurface. The near field corresponding to this non-modulated metasurface is simulated and then subtracted from the field of the near field multi-beam focusing metasurface. Even though this approach is not exact, it can give an idea about the radiation resulting from the leaky wave and the perturbation caused by the feeder radiation.

In figure 70, the horizontal cut corresponding to figure 68 is represented with the suppression of the feeder effect. The four desired beams are present in this figure with the expected polarization with significantly lower side lobe level (smaller than -20dB). The beamwidth is still equal to 0.63λ. The undesired residual fields present in the figure (especially the Ey components) are probably artifacts caused by the considered approach. Indeed, the field radiated by the feeder in presence of a non-modulated metasurface is not exactly the same as the one radiated in presence of a modulated metasurface.

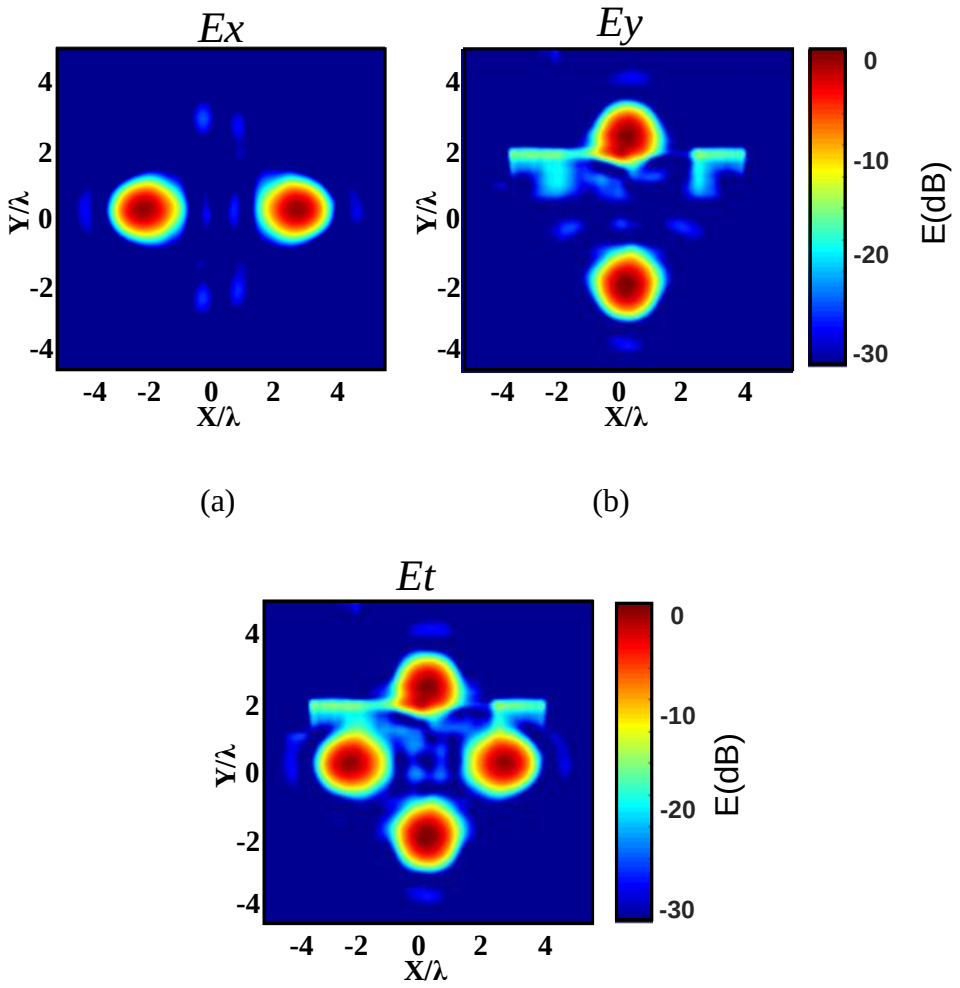

Figure 70: Simulated near field horizontal cut-plane in ANSYS Designer at the height $z = 5\lambda$ with feeder effect cancellation. (a) Ex component. (b) Ey component. (c) Total field Et.

In figure 71, the vertical cut corresponding to figure 69 is represented with a cancellation of the feeder effect. It can be seen from this figure that the four beams are effectively focused away from the metasurface. From figures 70 and 71, we can conclude that the feeder significantly deteriorates the field radiated by the metasurface. A solution should then be investigated in order to reduce the effect of the feeder on the radiated field and maximize the energy conversion into surface wave. The results of section 4.3.5 prove that the proposed design procedure can also be used for near-field control.

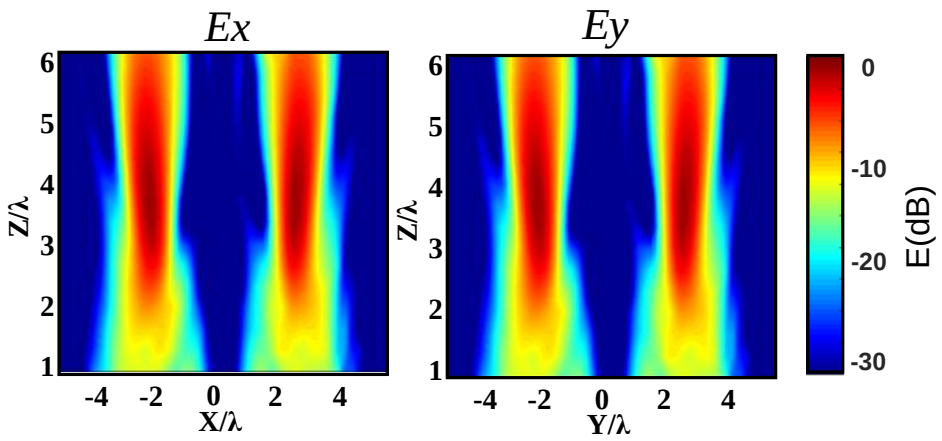

(a) (b)

Figure 71: Simulated near field vertical cut-plane in ANSYS Designer with feeder effect cancellation. (a) Ex component in the XZ plane. (b) Ey component in the YZ plane.

4.4 Conclusion of the chapter

In this chapter, several numerical results are presented in order to validate the proposed design procedure.

In the first part of the chapter, we studied in HFSS the effects of the geometrical parameters of the feeder on the antenna adaptation by varying the latter in different simulations on HFSS. We concluded from the parameter study that the resonant frequency was mainly affected by the outer radius parameter r_2 while the two remaining parameters r_1 and e mainly affected the level of the scattering parameter at the resonant frequency. Finally, a step by step algorithm for the adaptation of a metasurface antenna using the considered feeding structure was presented.

After that, several far field radiation patterns were implemented and validated with numerical software. At first a 3λ radius metasurface radiating a linearly polarized tilted beam was designed and simulated with FEKO and DESIGNER. The results were in close agreement with the theoretical results and corresponded to the objective radiation pattern. Then, several 5λ radius metasurfaces were designed. Using these

metasurfaces, a large variety of far field radiation patterns were achieved, ranging from multi-beam antennas to a flat top circularly polarized antenna. The simulations were in close agreement with the theoretical results. In light of the variety and complexity of the achieved radiation patterns, we concluded that arbitrary aperture field distributions could be implemented using the proposed method.

Finally, an example of near field control using metasurfaces is presented. In the considered example, a metasurface focusing four beams at a desired height is designed in collaboration with the IETR laboratory of the University of Rennes1. The simulation of the metasurface presented satisfactory results of near field beam focusing.

The study of last example led to the conclusion that the feeder significantly affects the near field radiation pattern of metasurface antennas. In fact, subtracting the contribution of the feeder from the simulated near field led to a significant improvement of the results. A future study should be performed in order to reduce this effect and maximize the surface wave energy conversion achieved by the feeder.

The simulation software HFSS is good at describing the feeding structure. However, it cannot simulate large size antennas. On the other hand, larger metasurfaces can be simulated using Designer. However, it does not give a good analysis of the feeding structure. As a result, HFSS is used in order to simulate the scattering parameter while Designer is used for the radiation pattern simulation. In addition, both Commercial software simulation cannot separate the different mechanism governing metasurface radiation. It can be very useful to develop an in-house code for the analysis of these structures as it allows the separation of the different radiation components such as: leaky waves, surface waves, radiation of the feeder, radiation at the edge of the metasurface…

In the next chapter, several metasurface antennas are manufactured and measured as a further validation of the proposed design procedure.

Chapter 5. Experimental results

5.1 Introduction

In this chapter, measurement results are presented as a validation of the proposed metasurface design procedure. At first, the manufacturing mechanical limitations are presented leading into a condition on the impedance database generation. Then a first prototype is manufactured on a substrate FR4 in order to check the precision obtained with the considered manufacturing process. The designed prototype radiation pattern is then measured to asses the validity of the simulation results. In the last part of this chapter, several examples of metasurface antennas are manufactured and measured. The masurements of the scattering parameter are compared with the results of HFSS while the radiation patterns are compared with the results of Designer.

5.2 Manufacturing limitations

As the metasurface consists of small patches printed over a grounded dielectric substrate, the main manufacturing limitation is the gap dimension between two conducting elements. Depending on the manufacturing technique (chemical, laser etching,...) this gap cannot be smaller than a certain minimum value. In the following, we denote this minimum gap by the variable $g_{\min}$.

Figure 72 shows two adjacent unit cells of the metasurface with identical shape. The figure is used to show how the typical geometry of our metasurface looks like. Judging from the figure, two type of gaps can be distingished:

- The gap g due to the presence of a v-shaped slot in the unit cell design.
- The gap g_p present between two adjacent patches. This gap results from the spacial periodicity.

By imposing the limitation condition on these two gaps, we will derive a condition on the variation range of the filling factor defined as $a_{\%} = \frac{d}{d'}$.

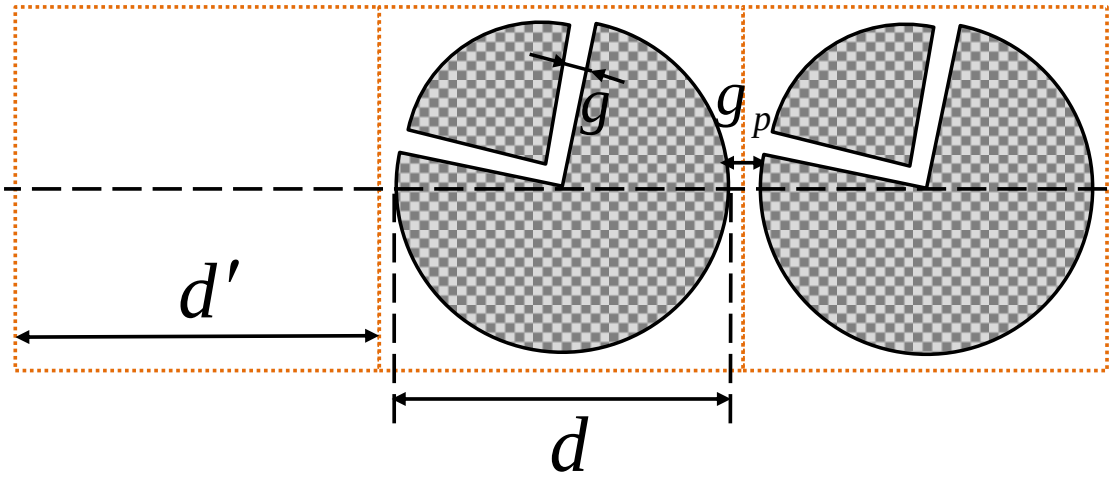

Figure 72: Description of the two gaps present in the structure: The gap g due to the v-shaped slot and the gap g_p due to the periodicity of the structure.

- **Condition on the slot gap :**

In our study, we considered unit cells with a v-shaped slot of width equal to 20% of the unit cell dimension. As a result, we can write :

$$g = 0.2d = 0.2\frac{d}{d'}d' = 0.2\,a_{\%}\,d' \tag{61}$$

Imposing that $g > g_{\min}$, namely:

$$0.2\,a_{\%}\,d' > g_{\min} \tag{62}$$

leads to the condition:

$$a_{\%} > 5\frac{g_{\min}}{d'} \tag{63}$$

- **Condition on the distance between two adjacent cells :**

The distance between two adjacent patches is minimal when the considered patches dimension is maximal. By considering two adjacent patches with the same dimension we can express the gap g_p as a function of the filling factor $a_{\%}$ as follows:

$$g_p = 2\left(d' - d\right) = 2\left(1 - \frac{d}{d'}\right)d' = 2\left(1 - a_{\%}\right)d' \tag{64}$$

Then by imposing that $g_p > g_{\min}$ we obtain

$$2\left(1-a_{\%}\right)d' > g_{\min} \tag{65}$$

And thus

$$a_{\%} < \left(1-\frac{g_{\min}}{2d'}\right) \tag{66}$$

By combining the inequalities (63) and (66) we obtain the following condition on the filling factor:

$$5\frac{g_{\min}}{d'} < a_{\%} < \left(1-\frac{g_{\min}}{2d'}\right) \tag{67}$$

Depending on the manufacturing process (the minimum achievable gap $g_{\min}$), equation (67) is used in order to limit the variation range of the filling factor $a_{\%}$ when generating the impedance database. Using this condition, we can ensure that the final metasurface geometry can be manufactured. For example, if we consider a practical case of a mimimum achievable gap $g_{\min} = 150\mu m$ and a periodicity $d' = 2.5mm$, we obtain that the filling factor has to satisfy: $0.3 < a_{\%} < 0.97$.

It can be seen from the Figure 35 (section 3.3.4) that the filling factor affects the variation range of the impedance components (in particular for the cross polarization elements). As a result, we must check the variation range of the impedance tensor elements when equation (67) is satisfied.

Another important limitation of the manufacturing process is related to the opening angle θ of the v-shapet slot of the unit cell. When this angle is too small, the triangular part of the unit cell is so small that it can detache during the manufacturing process. To avoid this problem, we only considered slot opening angles θ that are greater than 60°.

5.3 Mechanical validation test

High performance dielectric substrates used for space application are generally expensive and may have a long delivery time. In order to test the precision of the manufacturing process and avoid wasting expensive substrates, a metasurface prototype has been printed on a commun cheaper substrate (FR4 in our case).

The metasurface prototype have the following specifications:

- **Substrate :** FR4 of thickness h=1.6mm and relative permittivity ϵ_r=4,4. The dissipation factor of this substrate is $\tan\delta = 0.017$.
- **Working frequency :** 12.25GHz.
- **Dimension :** circular metasurface of diameter 38cm.
- **Unit cell dimension :** $d' = 2.5\text{mm}$ this dimension is also adequate for a working frequency of 10GHz.
- **Feeder :** the following geometrical parameters $(r_1; r_2; e) = (1.45; 6.6; 0.35)\,\text{mm}$ have been used to match the input impedance.
- **Objective radiation pattern :** broadside RHCP.

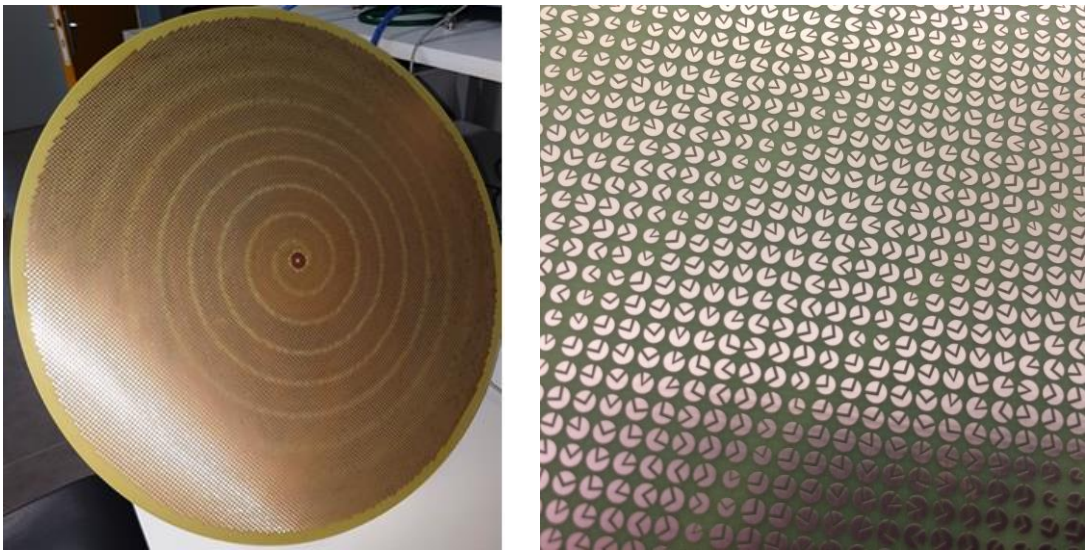

(a) (b)

Figure 73: Manufactured prototype for mechanical validation. (a) Whole structure. (b) Zoom on the metasurface.

The prototype was manufactured by the company INOVEOS [43] based in Brive-la-Gaillarde in France using a chemical process. Figure 73 shows the manufactured structure. The spiral shape of the resulting metasurface is due to the objective broadside RHCP radiation pattern. The unit cell of the structure was checked using a microscope as shown in figure 74. It can be seen from the two figures that the unit cell and the metasurface structure do not present visible imperfections.

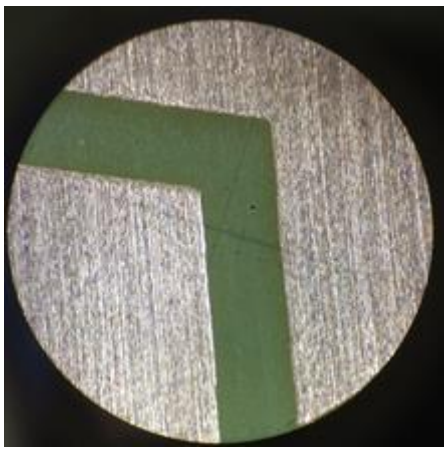

Figure 74: Microscopic view of the unit cell.

(a) (b)

Figure 75: Feeding structure on the manufactured prototype. (a) Without the coaxial cable. (b) With the coaxial cable

Figure 75 shows the feeding structure with and without a soldered coaxial cable. The feeding structure was also checked in the microscope and did not present undesired defaults. In light of these results, we decided to proceed with the manufacturing of practical metasurface antennas on an adequate substrate as a validation of the proposed metasurface design procedure.

5.4 Measurement of metasurface antennas

In this section, the measurement results for the different manufactured metasurface antennas are presented.

5.4.1 Measurement of the test prototype

Before measuring functional metasurfaces, the previously manufactured test prototype is measured. The measurement results are then compared with simulations in order to check the validity of our approach and explore the limitations of the simulation tools.

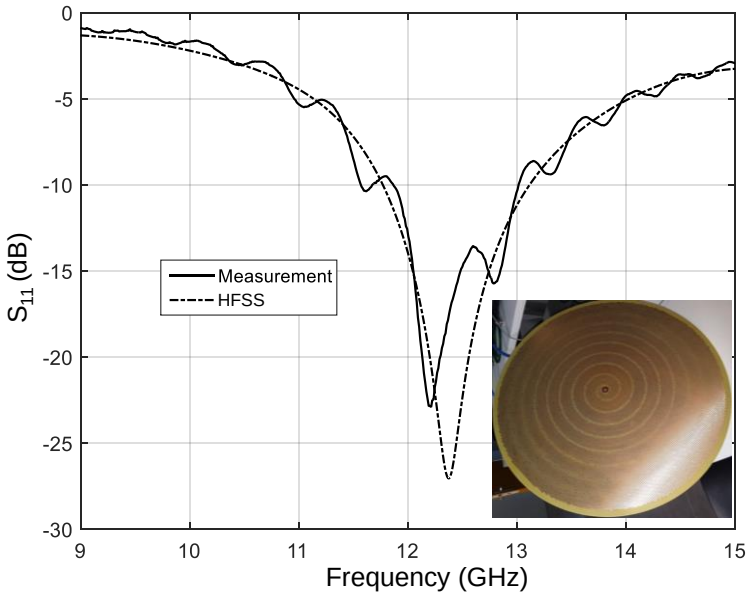

Figure 76: Variations of the scattering parameter S_{11} (in dB) of the metasurface prototype with respect to frequency (in GHz). The solid line gives the measurement results while the dashed line shows the simulation results obtained using HFSS.

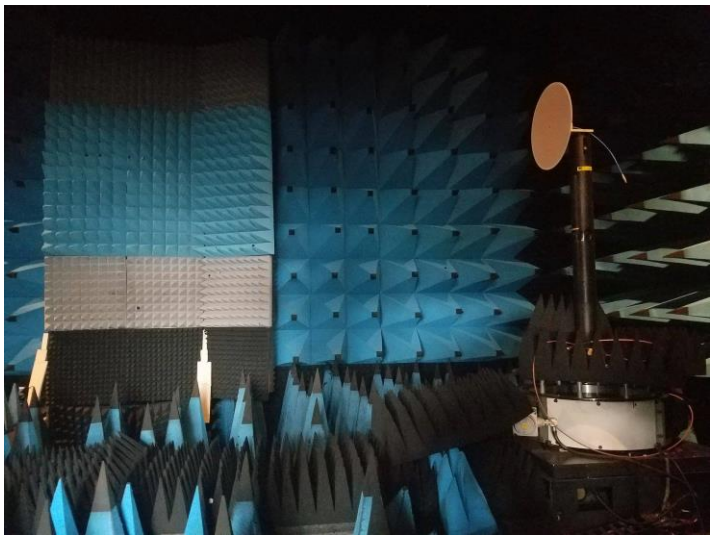

(a)

(b)

(c)

Figure 77: Measurement of the far field radiation pattern in the GeePs Laboratory. (a) Anechoic chamber. (b) Standard Gain Horn Antenna (reference). (c) Measured antenna.

The first step was the measurement of the antenna reflection parameter (S_{11}) of the antenna prototype. Figure 76 shows the comparison between measurements and HFSS simulations. It can be seen from the figure that the antenna is matched (S_{11}<-10dB) in

the frequency band [11.5-13]GHz. Therefore, the antenna is properly working at the desired frequency of 12.25GHz. In addition, a close agreement is obtained between the simulation and the measurement.

As second step, we measured the radiation pattern of the prototype at the GeePs Laboratory in France. Figure 77 shows the measurement setup for the far field radiation pattern. It consists of an anechoic chamber containing a reference antenna (figure 77.(b)) and the Antenna Under Test (AUT, figure 77.(c)) placed at a distance of 7m from each other. Before proceeding with the measurement, the AUT is aligned with the reference antenna using laser alignment as shown in figure 78.

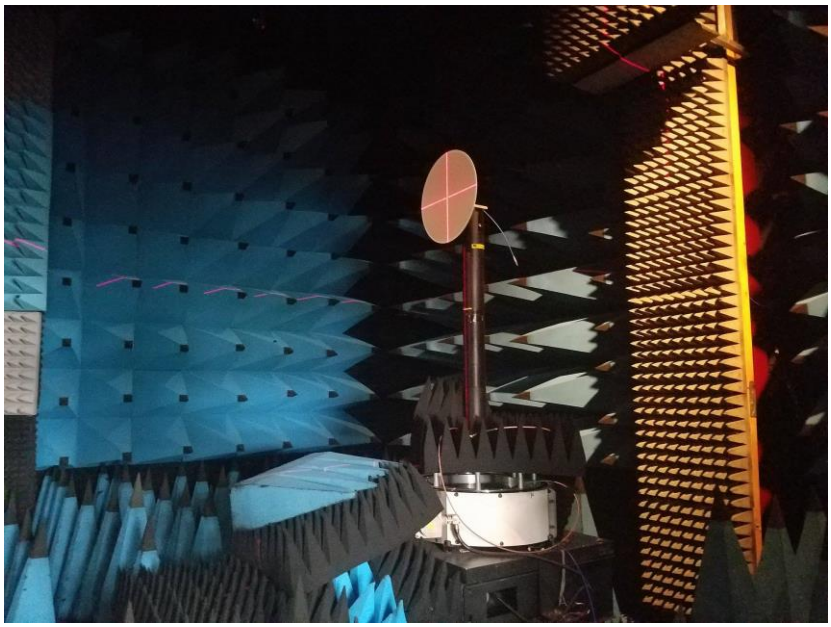

Figure 78: Laser alignment of the measurement antenna with the reference antenna.

Two orthogonal linear components were measured using the described setup in order to obtain the right hand and the left hand circular components of the radiated field. Figure 79 shows the measurement results (in black) of the far field radiation pattern in the $\phi = 0°$ cut-plane at 12.25GHz. The measurements are compared with the simulation results (in red) obtained using Ansys Designer. The RHCP components are represented by solid lines while the LHCP components are represented with dashed lines. The measured radiation pattern corresponds to the expected broadside RHCP beam. The measured cross-polarization level is equal to -20 dB and the side lobe level is equal to -27 dB. The beamwidth is equal to 5.3°. A close agreement is obtained be-

tween the simulation results and the measurements in the region of the main lobe. The discrepancy outside of this region is probably due to the fact the dielectric substrate is considered infinite in the simulation. There is therefore a discontinuity in the end of the metasurface that can lead to undesired radiations. In addition, due to the complexity of the structure, the mesh quality was significantly limited by the available computer memory. The measured gain is equal to 18dBi. The same gain value was obtained in the simulation. The low value of the gain is due to the high dissipation factor of the FR4 substrate ($\tan\delta = 0.017$ **)**.

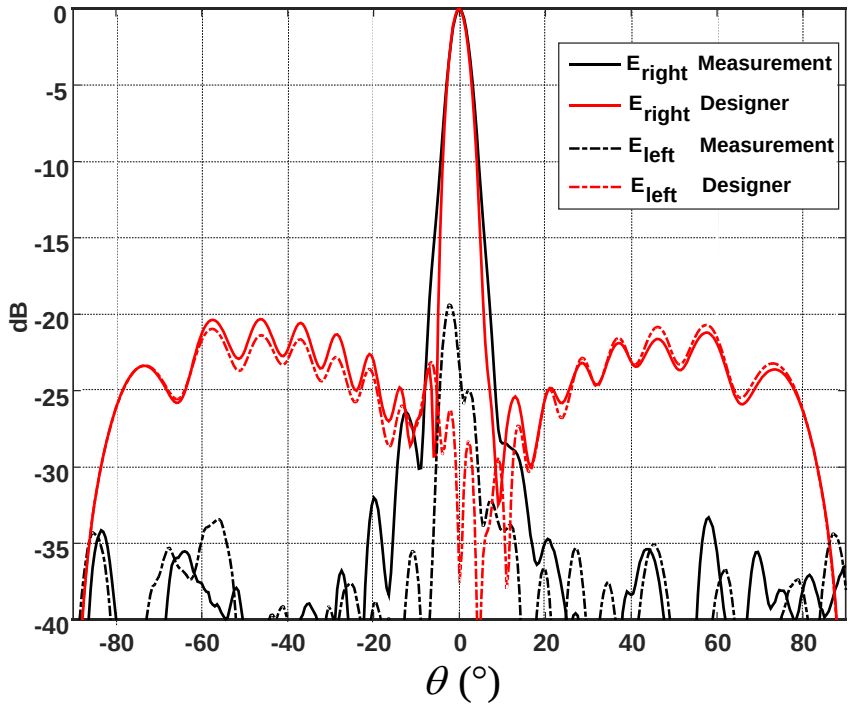

Figure 79: Measurement (in black) and simulation (in red) of the circular components of the far field radiation pattern for the $\phi = 0°$ cut-plane [30]. Solid lines represent RHCP components and dashed lines represent LHCP components. The working frequency is 12.25GHz.

5.4.2 Broadside RHCP Antenna

After measuring the radiation pattern of the test prototype, a similar antenna was manufactured on a substrate more suitable for space applications. The considered antenna has the following specifications:

- **Substrate :** Rogers TMM6 of thickness h=2.54mm and relative permittivity ϵ_r=6. The dissipation factor of this substrate is $\tan\delta = 0.0023$.
- **Working frequency :** 10GHz.
- **Dimension :** circular metasurface of diameter 38cm.
- **Unit cell dimension :** $d' = 2.5\text{mm}$.
- **Feeder :** $(r_1; r_2; e) = (1.45; 6.6; 0.35)\,\text{mm}$.
- **Objective radiation pattern :** broadside RHCP.
- **Amplitude distribution law:** in order to minimize the side lobe levels, a Hamming amplitude distribution was used [44].

As for the first prototype, the metasurface was manufactured by the company INOVEOS and is represented in figure 80. Also this metasurface exhibits the spiral shape associated to the circular polarization.

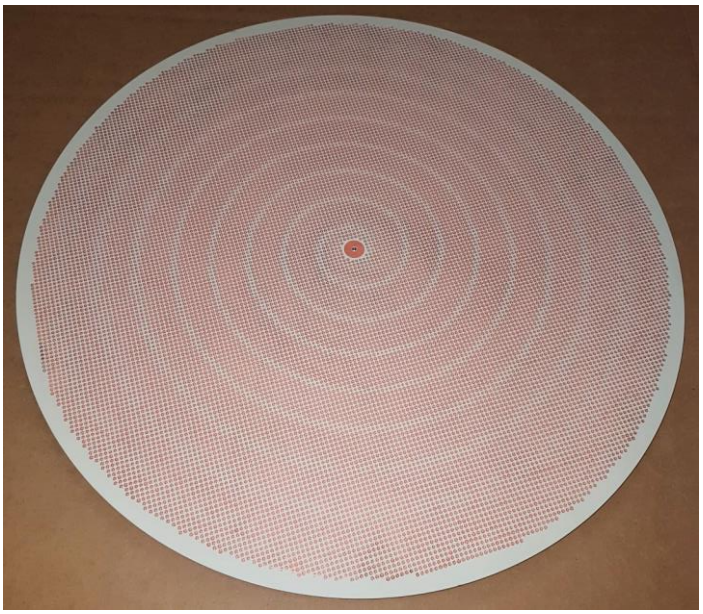

Figure 80: Manufactured broadside RHCP metasurface (printed on a substrate ROGERS TMM6).

In figure 81, measurement and the simulations of the scattering parameter S_{11} with respect to frequency are presented. The solid line corresponds to measurements while the dashed lines are simulations results obtained using HFSS. The effective relative permittivity of the substrate for the considered frequency (equal to 6.3) is different from the value used for the metasurface design. As a result, the simulation results are

presented in the case of ϵ_r=6 (in black) and ϵ_r=6.3 (in red). As it can be seen from the figure, measurements are closer to the simulations obtained with ϵ_r=6.3 (value given by Rogers). In addition, we noticed undesired oscillations in the measured scattering parameter. In our opinion, these oscillations are caused by the reflection of the surface wave at the edge of the metasurface. The reflected surface wave generates the oscillations when it returns to the feeder. This effect is less visible in the case of the FR4 because the propagating surface wave is attenuated by the high level of dielectric losses ($\tan\delta = 0.017$ **).** The level of the undesired oscillations can be reduced by increasing the metasurface dimensions. Thus, the propagating surface wave will either be converted into leaky waves or attenuated through propagation.

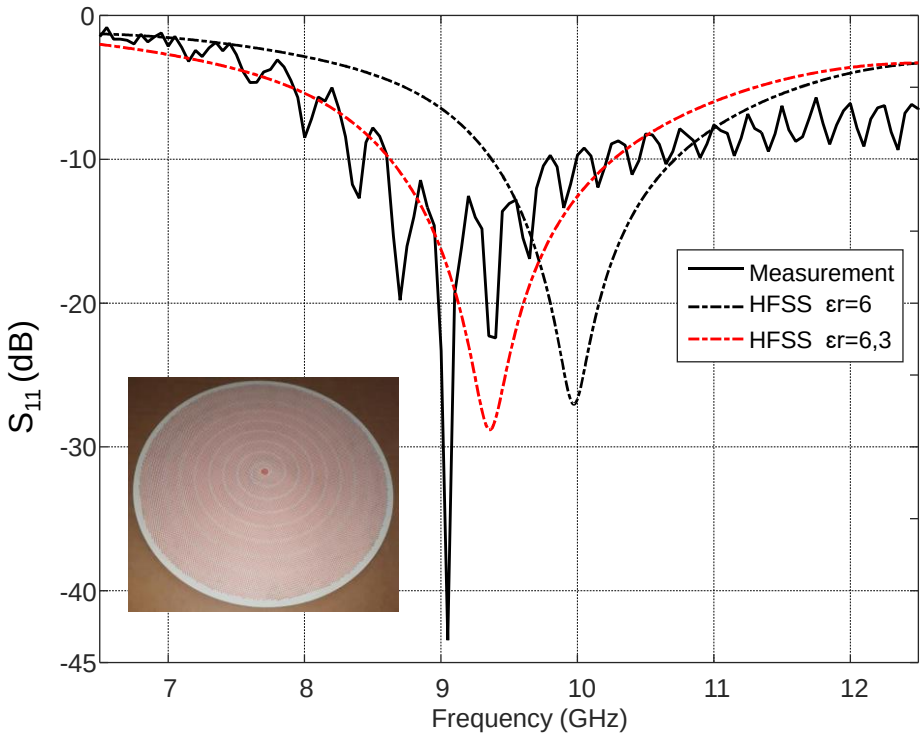

Figure 81: Variations of the scattering parameter S_{11} (in dB) of the manufactured broadside RHCP metasurface with respect to frequency (in GHz). The solid line gives the measurement results while the dashed line shows the simulation results obtained using HFSS.

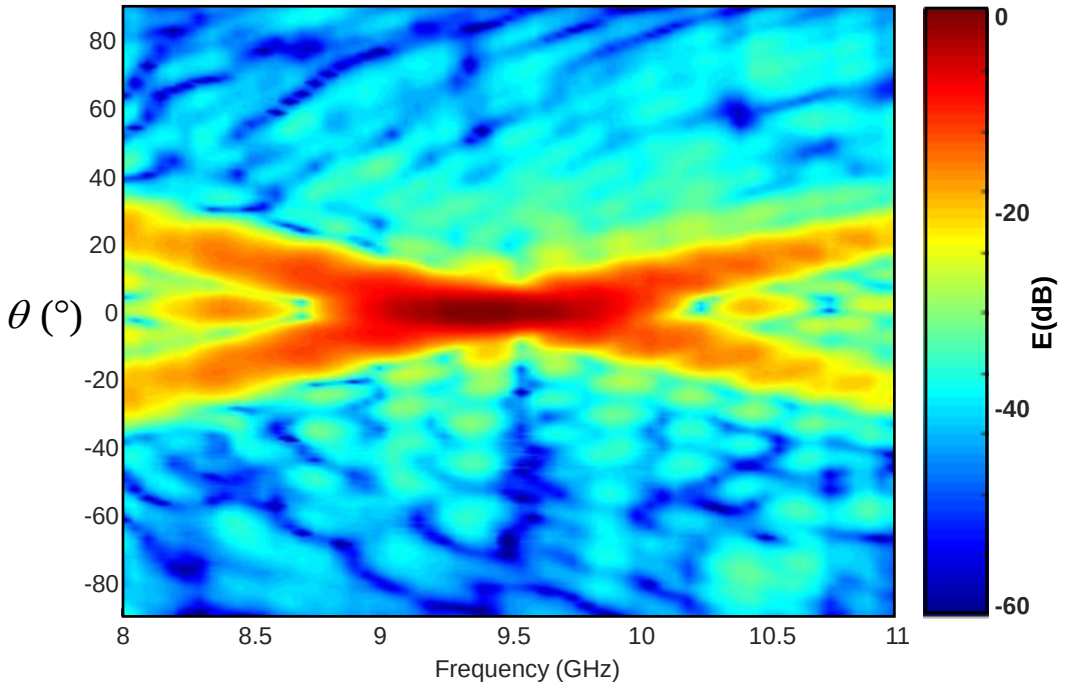

Figure 82: Variations of the RHCP component (normalized) in the $\phi = 0°$ cut-plane with respect to the frequency and the incident angle θ.

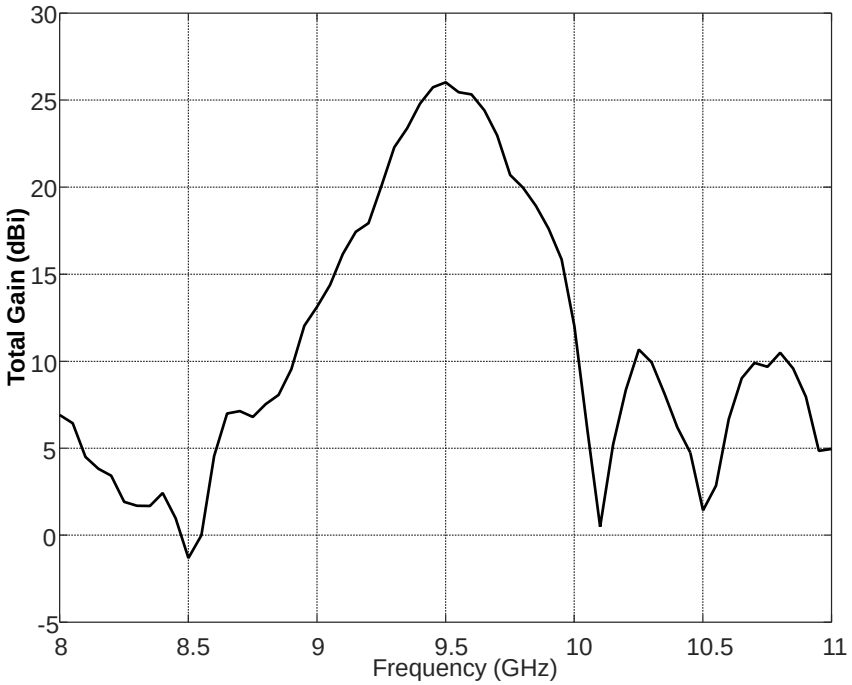

Figure 83: Variations of the gain at broadside in dBi with respect to the frequency.

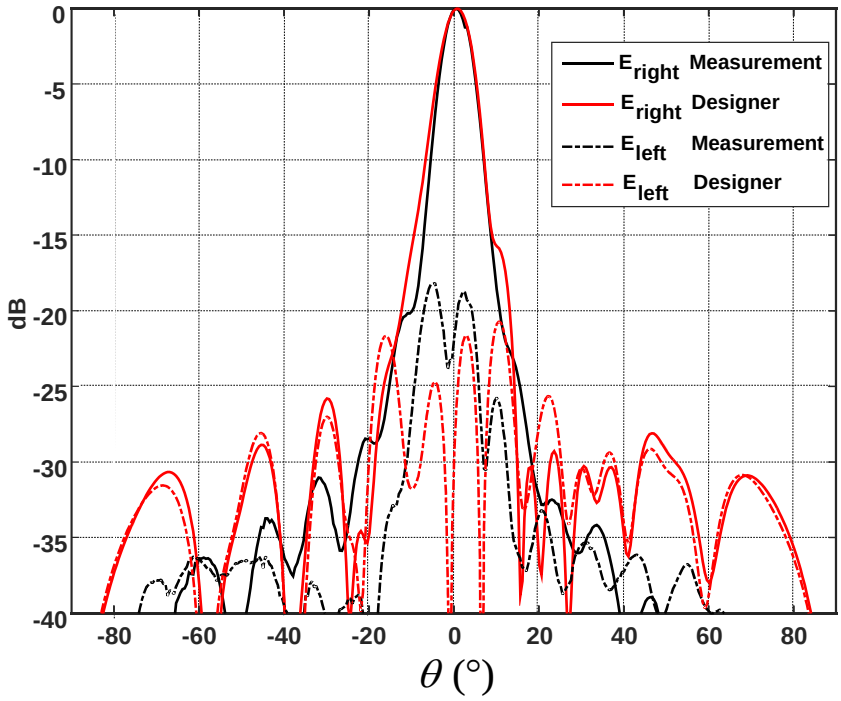

Figure 84: Measurement (in black) and simulation (in red) of the circular components of the far field radiation pattern of the broadside RHCP metasurface for the $\phi = 0°$ cut-plane. Solid lines represent RHCP components and dashed lines represent LHCP components. The working frequency for the simulations and the measurements is 9.5GHz.

As the scattering parameter curve does not correspond to the simulation, we considered the frequency of maximum broadside gain as the working frequency. In order to measure the gain, the radiation pattern of the metasurface is compared to the radiation pattern of a standard gain horn antenna. Figure 83 gives the variations of the total gain at broadside with respect to the frequency. The maximum gain value is equal to 26dBi at the frequency of 9.5GHz. For this antenna size, this corresponds to a total efficiency $e_0 = 30\%$. This value is not far from the theoretical aperture efficiency for a hamming distribution and for this dimension ($e_{ap} = 36\%$). This two values leads to a product $e_r e_{cd} = 83.33\%$. This product is high due to the low level of the dielectric losses introduced by the TMM6 ($\tan\delta = 0.0023$**).**

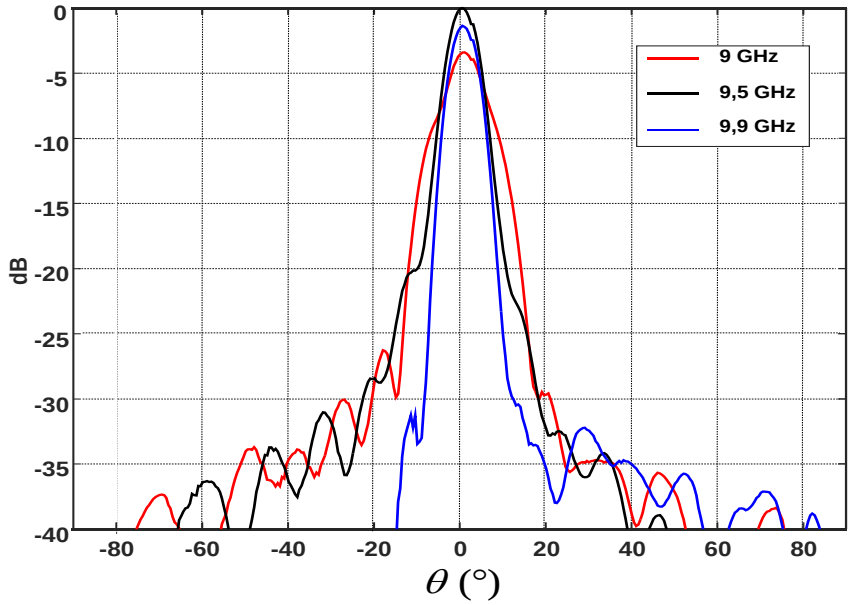

(a)

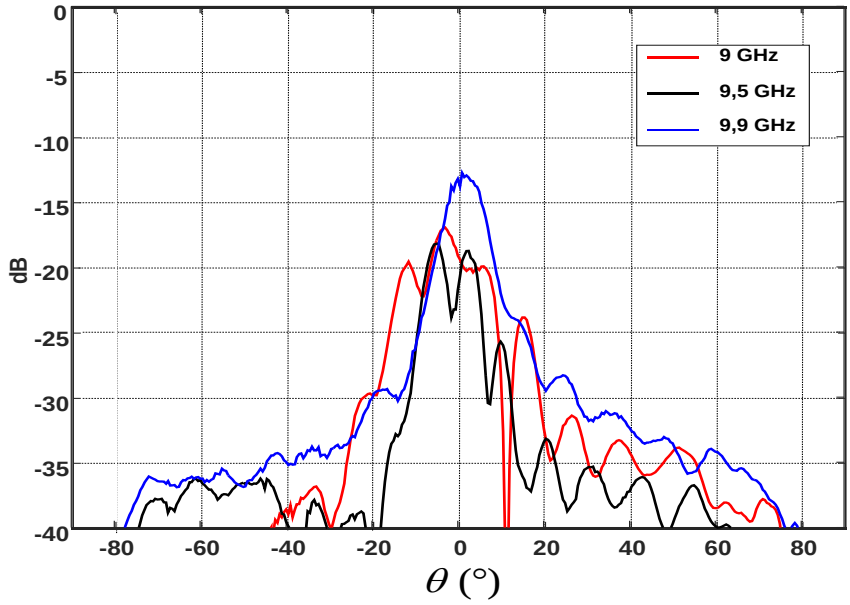

(b)

Figure 85: Variations of the measured radiation pattern with respect to frequency at the $\phi = 0°$ cut-plane for the broadside RHCP antenna. (a) RHCP components. (b) LHCP components. The considered frequencies are: 19.5 GHz (in red), 20GHz (in black) and 20.5GHz (in blue). The radiation pattern was normalized with respect to the maximum beam amplitude.

In figure 84, the measurement and the simulation results for the broadside RHCP metasurface radiation pattern are presented for the $\phi = 0°$ cut-plane. The antenna radiates the expected RHCP beam at broadside with cross-polarization smaller than -18 dB and side lobe levels smaller than -30dB. The measured beamwidth is equal to 4.6°. At the working frequency of 9.5GHz, the simulation results are pretty similar to the measurement results.

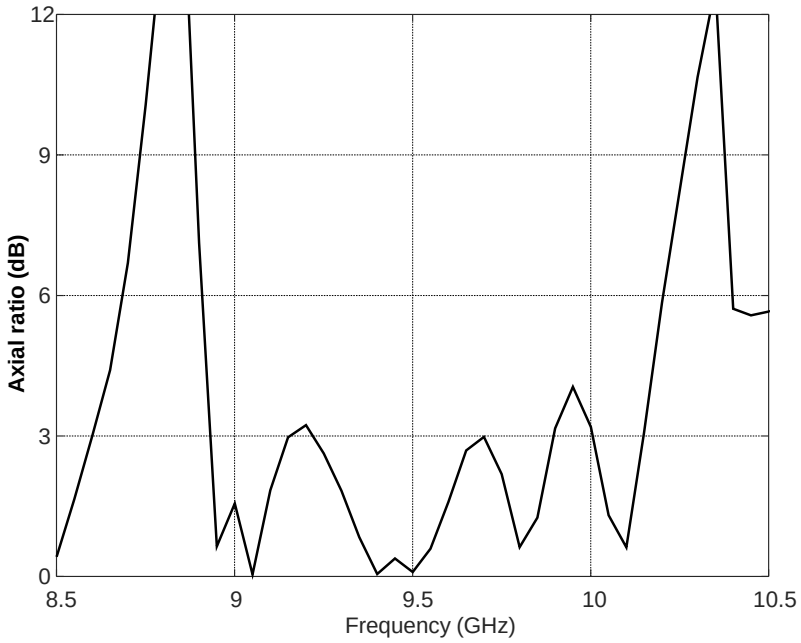

Figure 86: Variations of the axial ratio at broadside in dB with respect to the frequency.

Figure 85 shows the variation of the radiation pattern of the manufactured metasurface with respect to the frequency. The figure gives the circular components of the radiated field at the $\phi = 0°$ cut-plane for the frequencies 9 GHz (in red), 9.5GHz (in black) and 9.9GHz (in blue). We can see from the figure that the cross-polarization level and the side-lobe level are relatively stable in the considered bandwidth. In addition, by calculating the variation of the axial ratio in dB with respect to the frequency (see Figure 86), we can see that the axial ratio is smaller than 3dB for the bandwidth between 9GHz and 9.9 GHz. In light of the figures 84-86 we can see that, despite the frequency shift of the working frequency, the performances of the manufactured metasurface are quite promising and represent a first validation of the design procedure.

5.4.3 Four-beams metasurface antenna

The second antenna to be manufactured is the four-beam metasurface. This antenna is similar to the one presented in the previous chapter (Numerical Results). However, it was designed for a working frequency of 10GHz and manufactured on substrate ROGERS TMM6 of relative permittivity ϵ_r=6 and thickness h=2.54mm. The antenna parameters are the same as those of the manufactured broadside RHCP metasurface. A Hamming amplitude distribution was also applied in order to reduce the side lobes level. The metasurface was manufactured by INOVEOS and is represented in figure 87. The corresponding radiation pattern will be measured soon at the GeePs laboratory.

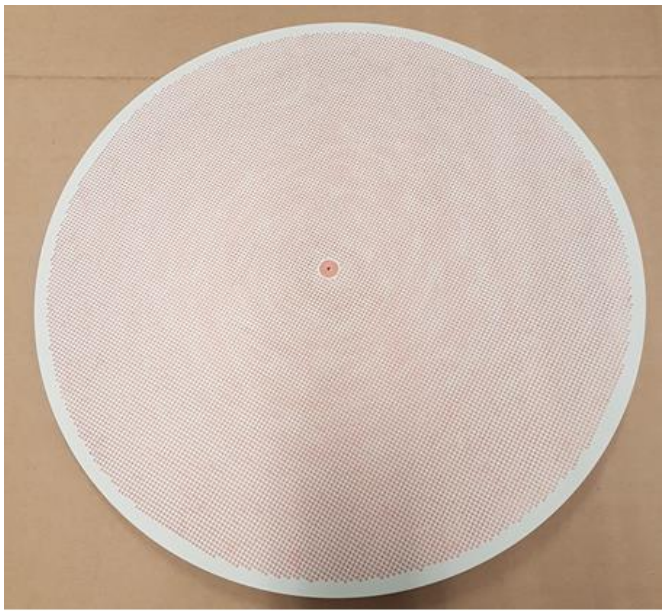

Figure 87: Manufactured four-beams metasurface (printed on a substrate ROGERS TMM6).

5.4.4 Near field multi-beam focusing metasurface antenna

In this last example, measurement results for a Near-Field beam focusing metasurface are presented. The metasurface designed in the previous chapter (in collaboration with the IETR laboratory of the University of Rennes1) have the following specifications:

- **Substrate :** Rogers TMM6 of thickness h=1.27mm and relative permittivity ϵ_r=6. The dissipation factor of this substrate is $\tan\delta = 0.0023$.

- **Working frequency :** 20GHz.
- **Dimension :** circular metasurface of diameter 15cm printed on a square substrate.
- **Unit cell dimension :** $d' = 1.25\text{mm}$.
- **Feeder :** $(r_1; r_2; e) = (0.8; 3.5; 0.25)\,\text{mm}$.
- **Objective radiation pattern :** near-field multi-beam focusing.

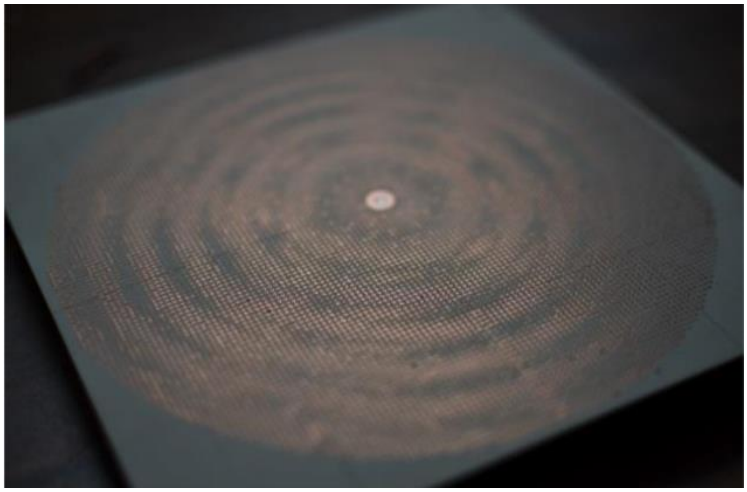

Figure 88: Manufactured near-field multi-beam focusing antenna [41] -[42].

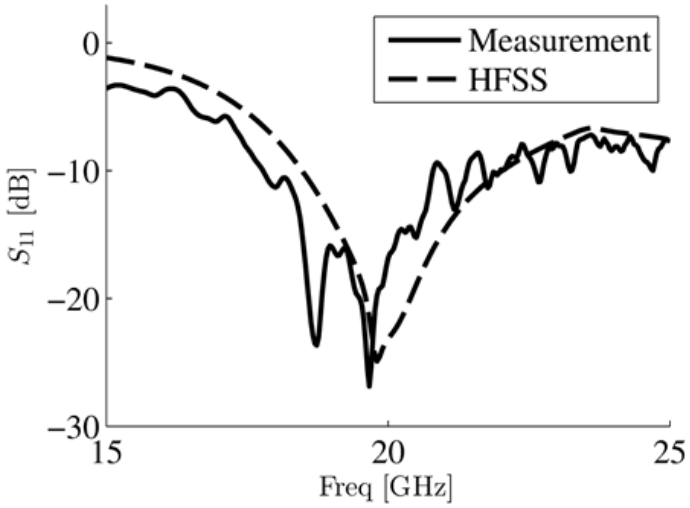

Figure 89: Variations of the scattering parameter S_{11} (in dB) of the near-field multi-beam focusing antenna [41]-[42]. The solid line gives the measurement results while the dashed line shows the simulation results obtained using HFSS.

The antenna was manufactured using laser etching technique and is represented in the figure 88. The scattering parameter S_{11} were measured at the IETR in the frequency band [15-25]GHz. The comparison between measurements and simulations results obtained using HFSS is represented in figure 89. The figure shows that the antenna is matched at the working frequency of 20GHz. In addition, a similar behaviour of the scattering parameter (frequency shift + oscillations) as in the previous examples is noticed.

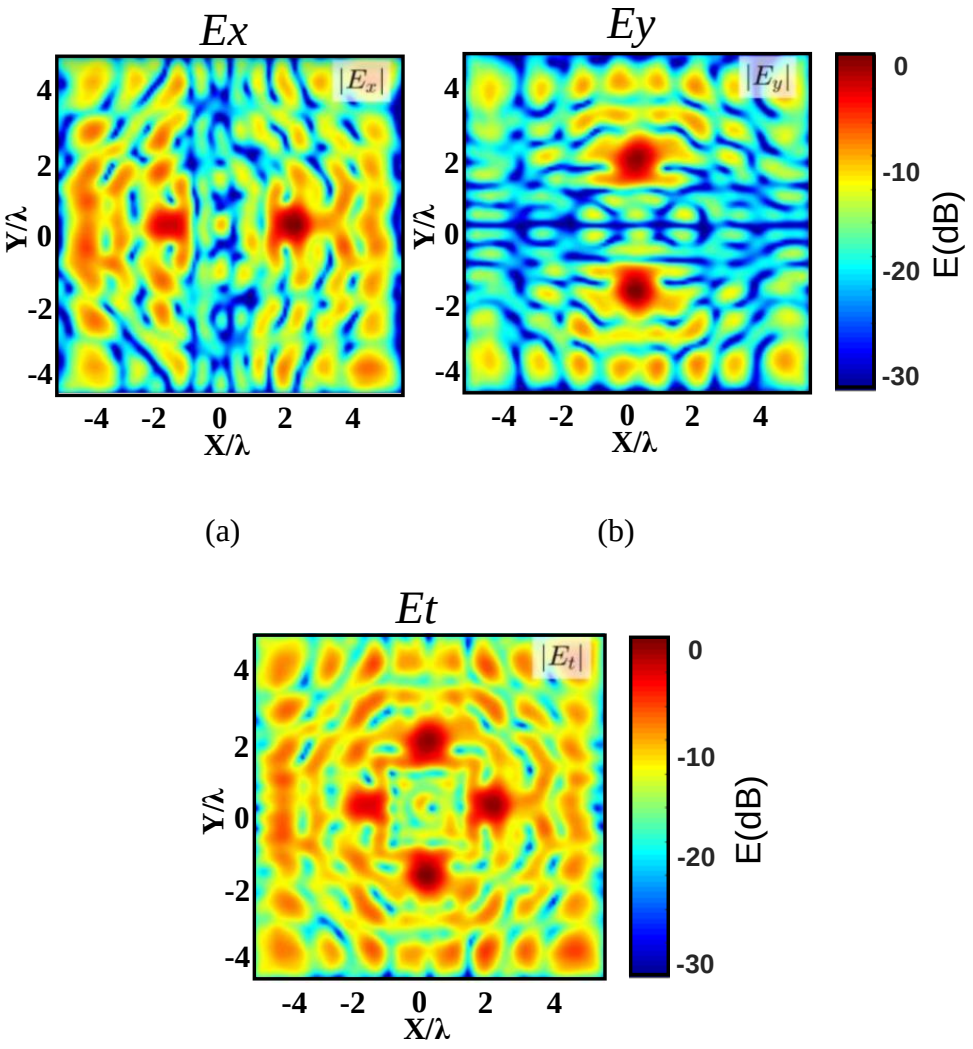

(a) (b)

(c)

Figure 90: Measured near field radiation pattern at the height $z = 5\lambda$ [41]-[42]. (a) Ex component. (b) Ey component. (c) Total field Et.

The near field was then measured at the IETR. Figure 90 gives the measurement results for the horizontal cut at a height of $z = 5\lambda$. The figures 90.(a) and (b) show the linear components of the electric field while the figure 90.(c) shows the total field. It can be seen from the figure that the radiated near field exhibits the desired near field focusing behavior. The obtained beams have the expected polarizations (two beams polarized along the x axis and two beams along the y axis). The beamwidth is equal to 0.6λ with side-lobe levels about -12dB. In light of the results obtained in the previous chapter, we assume that they are mainly caused by the spatial radiation of the feeder. Indeed, this effect should be more predominant in near-field applications.

5.5 Conclusion of the chapter

In this chapter, an experimental validation of the metasurface design procedure is presented. In the first part, the limitations of the metasurfaces manufacturing were presented. The main limitation is the minimum distance between the conductors composing the structure. This limitation emerges in two parameters of the structure : (1) The gap g due to the v-shaped slot present in the unit cell. (2) The gap g_p between two adjacent unit cells that is due to the spatial periodicity of the structure. This constraint led to a condition on the filling factor ($a_{\%}$) variation range. By satisfying this condition during the impedance database generation, one can insure that the designed metasurface respects that manufacturing limitations.

Then, a metasurface prototype design was manufactured on a substrate FR4 to assess the manufacturing precision of the metasurface geometry. This step was performed in order to check if the unit cells shapes were manufactured with a satisfying level of precision. The prototype was designed for a metasurface radiating a broadside RHCP beam at the frequency of 12.25GHz. The structure was manufactured by the company INOVEOS based in Brive-la-Gaillarde in France with a chemical process giving a very good level of precision. The prototype radiation pattern was then measured at the GeePs laboratory giving results in good agreement with the simulation.

After that, a broadside RHCP metasurface was manufactured on a substrate ROGERS TMM6 that is more suitable for space applications. The metasurface is similar to the one presented in the simulation chapter but with an objective working frequency of 10GHz. However, a frequency shift of the adaptation bandwidth as well as undesired oscillations were noticed when measuring the scattering parameter S_{11}. In our opinion,

this is probably due to undesired reflections at the edge of the metasurface and to a difference in the relative permittivity of the substrate. The far field radiation pattern of the metasurface antenna was measured in the GeePs laboratory giving the desired broadside RHCP beam with a cross polarization level of –18 dB and side lobe level smaller than of –30 dB. In addition, the antenna parameters (cross polarization level, side lobe level and axial ration) are relatively stable over a bandwidth between 9GHz and 9.9GHz. The maximum gain is equal to 26dB at a frequency of 9.5GHz. This corresponds to total efficiency $e_0 = 30\%$. A four-beam metasurface was also manufactured for an objective working frequency of 10GHz and is ready to be measured at the same laboratory.

Finally, a near-field multi-beam focusing metasurface was manufactured in collaboration the IETR laboratory of the University of Rennes1. The metasurface of working frequency 20GHz was measured at the IETR. A horizontal cut of the Cartesian components of the electric field for a height of $z = 5\lambda$ was presented. The measured near field comported the desired four focused beams with the expected polarization. The side-lobe levels of the manufactured metasurface are equal to -12dB. This is probably caused by the spatial radiation of the feeder. Indeed, as stated in the previous chapter, not all the energy injected in the feeder is converted into surface wave. This leads to undesired radiations by the feeding structure.

Despite the undesired oscillations in the scattering parameters, the manufactured metasurfaces presented the desired radiation pattern in all the presented examples. In addition, the TMM6 antennas (broadside RHCP and near-field focusing) presented good performances and they represent a first experimental validation of the proposed metasurface design procedure. In future work, additional sets of metasurfaces will be manufactured in order by improve their performances such as : side lobe levels reduction, efficiency enhancement, edge reflections reductions...

Chapter 6. Conclusions and Prospective

6.1 Summary of the contribution

In this thesis, a method for the generation of arbitrary aperture field distribution using modulated tensorial metasurfaces is presented. Chapter 2 gives the formulation of the method as well as some theoretical background about scalar and tensorial metasurfaces. When a surface wave propagates through a sinusoidally modulated metasurface, leaky waves that propagates away from the surface are generated. The phase of these waves can be controlled by acting on the periodicity of the modulation using a holographic principle. On the other hand, the amplitude is controlled using modulation indices and average impedances that vary depending on the position on the metasurface. A new local framework formulation is introduced in order to simplify the different calculations. The idea is to control these leaky waves in order to generate the desired aperture distribution. By modulating the different impedance elements separately, the aperture field components can be controlled independently.

In chapter 3, the different aspects of the metasurface implementation are presented. The previous formulation is written in the case of a cylindrical surface wave excitation. The metasurface is implemented using sub-wavelength patches printed over a grounded dielectric substrate. The chapter also describes the unit cell design as well as the impedance database generation. Finally, the different steps of the metasurface design algorithm are described, from the specification of the objective aperture field to the generation of the antenna DXF file.

In chapter 4, numerical results obtained using simulation software are presented. At first, the effects of the parameters of the feeder on the adaptation of the antenna are studied. Each parameter was investigated separately leading to the development of a step-by-step adaptation algorithm. After that, several metasurface designs for far field radiation pattern control were simulated: broadside RHCP metasurface, tilted beam linearly polarized metasurface, multi-beam metasurface and flat top RHCP metasurface. For this wide range of examples, the simulated radiation pattern was in close agreement with the field radiated by the ideal aperture field distribution and by the estimated magnetic field currents above the metasurface. Finally, a near-field multi-

beam focusing design was generated in collaboration with the IETR laboratory of the University of Rennes1. The theoretical aperture field distribution was calculated by our partners and was then injected in our algorithm in order to generate the metasurface structure. The simulated near field corresponded to the objective radiation but was significantly affected by the radiation of the feeder.

Chapter 5 was dedicated to the presentation of the manufacturing process as well as some initial experimental results. A metasurface prototype as well as two metasurfaces structures (broadside RHCP and four-beams) were manufactured by the company INOVEOS that is based in Brive-la-Gaillarde in France. The prototype was manufactured on a FR4 substrate for mechanical validation of the manufacturing process. On the other hand, the two other metasurfaces were manufactured on a ROGERS TMM6 substrate that is more suitable for space applications. The prototype and the broadside RHCP metasurfaces were measured in the GeePs laboratory. The measured radiation pattern was in good agreement with the simulation results. However, a frequency shift was present in the TMM6 metasurface. In the final part of the chapter, a near field multi-beam focusing metasurface was manufactured and measured in the IETR laboratory. The measured near field exhibits the expected four beams with the desired polarizations.

6.2 Future work

The obtained simulation and the experimental results are very promising and prove that a good control of the aperture field distribution is achieved with the proposed procedure. However, several aspects need to be considered in order to improve the performance of these metasurfaces:

- The feeder affects the field radiated by the metasurface, especially in the case of near field application. As a result, it is important to optimize the feeding structure in order to maximize the energy that is converted into surface wave (and therefore minimize the energy that is radiated by the feeder).
- The considered aperture field distributions were used as a first validation of the method. They have to be optimized in order to improve the antenna performances such as side lobe levels and directivity.

- Undesired edges reflections should be reduced by increasing the antenna dimension and maximizing the surface wave to leaky wave conversion.
- Metasurface antennas are narrow band. It is then important to improve their bandwidth and find a compromise between the bandwidth and the efficiency. A possible solution is to use multi-layered substrate.
- The reconfigurability of the metasurface should also be investigated.
- Commercial simulation software are pretty limited when it comes to analyzing metasurfaces. It can be very useful to develop an in-house code for the analysis of these structures as it allows the separation of the different radiation mechanisms such as: leaky waves, surface waves, radiation of the feeder, radiation at the edge of the metasurface…

6.3 List of publications

The work in this thesis has been published in the following peer-reviewed journals and conference proceedings.

Peer-reviewed journal articles:

2017 **M.Teniou**, H.Roussel, M. Serhir, N.Capet, G-P.Piau, M Casaletti, "Tensorial Metasurface Antennas Radiating Polarized Beams Based on Aperture Field Implementation" *International Journal of Microwave and Wireless Technologies.* **Under review**

2016 **M.Teniou**, H.Roussel, N.Capet, G-P.Piau, M Casaletti, "Implementation of radiating aperture field distribution using tensorial metasurface" *IEEE Trans. Antennas Propagat.*

International conferences:

2017 I.Iliopoulos, M.Ettorre, R.Sauleau, **M.Teniou**, M.Casaletti, P.Potier, P.Pouliguen, **"**Microwave multi-beam generation using an aniso-

tropic metasurface**"** ***APS/URSI 2017.***

2017 **M.Teniou**, H.Roussel, N.Capet, G-P.Piau, M Casaletti, "Modulated Tensorial Metasurfaces for Aperture Field Generation" ***Eucap 2017***. **Best paper awards finalist in Antenna Design and Applications**

2016 **M.Teniou**, H**.**Roussel, N**.**Capet, G-P**.**Piau, M Casaletti**, "**Complex aperture field generation using tensorial metasurfaces**"** ***APS/URSI 2016.***

National conferences:

2017 **M.Teniou**, H.Roussel, N.Capet, G-P.Piau, M Casaletti, "Méthode de conception d'antennes à métasurfaces pour la génération de distribution arbitraire de champs d'ouvertures" ***JNM 2017***. **Best paper awards finalist**

REFERENCES

[1] A. Alù and N. Engheta, “Pairing an epsilon-negative slab with a mu-negative slab: Resonance, tunneling and transparency,” *IEEE Trans. Antennas and Propagation (Special Issue)*, vol. 51, pp. 2558–2571, Oct. 2003

[2] A. Alù and N. Engheta, “Mono-modal waveguides filled with a pair of parallel epsilonnegative (ENG) and mu-negative (MNG) metamaterial layers,” *in IEEE MTT-S Int. Microwave Symp. Dig*., Philadelphia, PA, June 8–13, 2003, pp. 313–316

[3] D. R. Smith, W. J. Padilla, D. C. Vier, S. C. Nemat-Nasser, and S. Schultz, “Composite medium with simultaneously negative permeability and permittivity,” *Phys. Rev. Lett*., vol. 84, no. 18, pp. 4184–4187, May 2000.

[4] D. R. Smith and N. Kroll, “Negative refractive index in left-handed materials,” *Phys. Rev. Lett*., vol. 85, no. 14, pp. 2933–2936, Oct. 2000.

[5] J. B. Pendry, “Negative refraction makes a perfect lens,” *Phys. Rev. Lett*., vol. 85, no. 18, pp. 3966–3969, Oct. 2000.

[6] C. Holloway, E. Kuester, J. Gordon, J. O'Hara, J. Booth and D. Smith, "An Overview of the Theory and Applications of Metasurfaces: The Two-Dimensional Equivalents of Metamaterials", *IEEE Antennas and Propagation Magazine*, vol. 54, no. 2, pp. 10-35, 2012.

[7] F. O’Nians and J. Matson, “Antenna Feed System Utilizing Polarization Independent Frequency Selective Intermediate Reflector,” U.S. patent 3,231,892, Jan. 25, 1966.

[8] B. A. Munk, *Frequency Selective Surfaces: Theory and Design.* New York: Wiley-Interscience, 2000.

[9] S. Maci, G. Minatti, M. Casaletti and M. Bosiljevac, "Metasurfing: Addressing Waves on Impenetrable Metasurfaces", *IEEE Antennas and Wireless Propagation Letters*, vol. 10, pp. 1499-1502, 2011.

[10] C. Pfeiffer and A. Grbic, "A Printed, Broadband Luneburg Lens Antenna", *IEEE Transactions on Antennas and Propagation*, vol. 58, no. 9, pp. 3055-3059, 2010.

[11] M. Bosiljevac, M. Casaletti, F. Caminita, Z. Sipus, and S. Maci, “Nonuniform metasurface Luneburg lens antenna design,” *IEEE Transactions on Antennas and Propagation*, vol. 60, no. 9, pp. 4065–4073, Sep. 2012

[12] C. Pfeiffer and A. Grbic, "Metamaterial Huygens’ Surfaces: Tailoring Wave Fronts with Reflectionless Sheets", *Physical Review Letters*, vol. 110, no. 19, 2013.

[13] M. Selvanayagam and G. Eleftheriades, “Discontinuous electromagnetic fields using orthogonal electric and magnetic currents for wavefront manipulation,” *Opt. Expr*., vol. 21, no. 12, pp. 14409–14429, Jun. 2013.

[14] Nanfang Yu, P. Genevet, F. Aieta, M. Kats, R. Blanchard, G. Aoust, J. Tetienne, Z. Gaburro and F. Capasso, "Flat Optics: Controlling Wavefronts With Optical Antenna Metasurfaces", *IEEE Journal of Selected Topics in Quantum Electronics*, vol. 19, no. 3, pp. 4700423-4700423, 2013.

[15] Oliner, A. A., & Hessel, A. (1959). Guided waves on sinusoidally-modulated reactance surfaces. *Antennas and Propagation, IRE Transactions on*, *7*(5), 201-208.

[16] Patel, A. M., & Grbic, A. (2011). A printed leaky-wave antenna based on a sinusoidally-modulated reactance surface. *Antennas and Propagation, IEEE Transactions on*, *59*(6), 2087-2096.

[17] Fong, B. H., Colburn, J. S., Ottusch, J. J., Visher, J. L., & Sievenpiper, D. F. (2010). Scalar and tensor holographic artificial impedance surfaces. *Antennas and Propagation, IEEE Transactions on*, *58*(10), 3212-3221.

[18] G. Minatti, F. Caminita, M. Casaletti and S. Maci, "Spiral Leaky-Wave Antennas Based on Modulated Surface Impedance", *IEEE Transactions on Antennas and Propagation*, vol. 59, no. 12, pp. 4436-4444, 2011.

[19] S. Pandi, C. Balanis and C. Birtcher, "Design of Scalar Impedance Holographic Metasurfaces for Antenna Beam Formation With Desired Polarization", *IEEE Transactions on Antennas and Propagation*, vol. 63, no. 7, pp. 3016-3024, 2015.

[20] M. Casaletti, M. Smierzchalski, M. Ettorre, R. Sauleau and N. Capet, "Polarized Beams Using Scalar Metasurfaces", *IEEE Transactions on Antennas and Propagation*, vol. 64, no. 8,

pp. 3391-3400, 2016.

[21] A. Martinez-Ros, J. Gomez-Tornero, V. Losada, F. Mesa and F. Medina, "Non-Uniform Sinusoidally Modulated Half-Mode Leaky-Wave Lines for Near-Field Focusing Pattern Synthesis", *IEEE Transactions on Antennas and Propagation*, vol. 63, no. 3, pp. 1022-1031, 2015.

[22] G. Minatti, S. Maci, P. De Vita, A. Freni and M. Sabbadini, "A Circularly-Polarized Isoflux Antenna Based on Anisotropic Metasurface", *IEEE Transactions on Antennas and Propagation*, vol. 60, no. 11, pp. 4998-5009, 2012.

[23] G. Minatti, M. Faenzi, E. Martini, F. Caminita, P. De Vita, D. Gonzalez-Ovejero, M. Sabbadini and S. Maci, "Modulated Metasurface Antennas for Space: Synthesis, Analysis and Realizations", *IEEE Transactions on Antennas and Propagation*, vol. 63, no. 4, pp. 1288-1300, 2015.

[24] G. Minatti, F. Caminita, E. Martini and S. Maci, "Flat Optics for Leaky-Waves on Modulated Metasurfaces: Adiabatic Floquet-Wave Analysis", *IEEE Transactions on Antennas and Propagation*, vol. 64, no. 9, pp. 3896-3906, 2016.

[25] G. Minatti, F. Caminita, E. Martini, M. Sabbadini and S. Maci, "Synthesis of Modulated-Metasurface Antennas With Amplitude, Phase, and Polarization Control", *IEEE Transactions on Antennas and Propagation*, vol. 64, no. 9, pp. 3907-3919, 2016.

[26] M. Faenzi, F. Caminita, E. Martini, P. De Vita, G. Minatti, M. Sabbadini and S. Maci, "Realization and Measurement of Broadside Beam Modulated Metasurface Antennas", *IEEE Antennas and Wireless Propagation Letters*, vol. 15, pp. 610-613, 2016.

[27] M.Teniou, H.Roussel, N.Capet, G-P.Piau, M Casaletti, “Implementation of radiating aperture field distribution using tensorial metasurface” *IEEE Trans. Antennas Propagat.*

[28] M.Teniou, H.Roussel, N.Capet, G-P.Piau, M Casaletti, “Complex aperture field generation using tensorial metasurfaces” *Conference IEEE APS 2016, AP-S/URSI 2016,* Jun 2016, Fajardo (Porto-Rico), United States. 2016

[29] M.Teniou, H.Roussel, N.Capet, G-P.Piau, M Casaletti, “Modulated Tensorial Metasurfaces for Aperture Field Generation” *2017 11th European Conference on Antennas and Propagation (EUCAP),* Paris, 2017, pp. 3405-3407.

[30] M.Teniou, H.Roussel, M.Serhir, N.Capet, G-P.Piau, M Casaletti, “Tensorial Metasurface Antennas Radiating Polarized Beams Based on Aperture Field Implementation” *International Journal of Microwave and Wireless Technologies*. *submitted*

[31] C. Balanis, *Antenna theory*, 1st ed. Hoboken, NJ: John Wiley, 2005.

[32] C. Parini, A. Olver, K. Raghavan, D. Brain and Y. Kalatizadeh, "Design aspects and tolerances in array fed contour beam antennas of INTELSAT VI type", *IEE Proceedings H Microwaves, Antennas and Propagation*, vol. 135, no. 6, p. 408, 1988.

[33] A. Cherrette, S. Lee and R. Acosta, "A method for producing a shaped contour radiation pattern using a single shaped reflector and a single feed", *IEEE Transactions on Antennas and Propagation*, vol. 37, no. 6, pp. 698-706, 1989.

[34] N. H. Abd Rahman, M. T. Islam, N. Misran, Y. Yamada and N. Michishita, “Design of a satellite antenna for Malaysia beams by ray tracing method,” *International Symposium on Antennas and Propagation*, pp. 1385-1388, 2012.

[35] M. Mahajan, R. Jyoti, K. Sood and S. Sharma, "A Method of Generating Simultaneous Contoured and Pencil Beams From Single Shaped Reflector Antenna", *IEEE Transactions on Antennas and Propagation*, vol. 61, no. 10, pp. 5297-5301, 2013.

[36] C. Soukoulis, *Photonic crystals and light localization in the 21st century*. Dordrecht: Kluwer Academic Publishers, 2001.

[37] D. Hoppe and Y. Rahmat-Samii, *Impedance boundary conditions in electromagnetics*. Washington, DC: Taylor & Francis, 1995.

[38] H. Bilow, "Guided waves on a planar tensor impedance surface", *IEEE Transactions on Antennas and Propagation*, vol. 51, no. 10, pp. 2788-2792, 2003.

[39] M. Casaletti, “Guided Waves on Periodically Modulated Scalar and Tensorial Reactance Surfaces: a Circuital Approach,” *arXiv preprint arXiv:*1703.01294, 2017

[40] S. J. Orfanidis. (2013). *Electromagnetic Waves and Antennas* [Online]. Available: http://eceweb1.rutgers.edu/~orfanidi/ewa/

[41] I.Iliopoulos, M.Ettorre, R.Sauleau, M.Teniou, M.Casaletti, P.Potier, P.Pouliguen, "Micro-

wave multi-beam generation using an anisotropic metasurface", *APS/URSI 2017*

[42] I. Iliopoulos, "Engineering the near field of radiating systems at millimeter waves: from theory to applications", *Ph.D. dissertation*, IETR, Univ. Rennes1 1, Rennes1, France, 2017.

[43] INOVEOS SARL http://inoveos.com/

[44] F. J. Harris, "On the use of windows for harmonic analysis with the discrete Fourier transform," in *Proceedings of the IEEE*, vol. 66, no. 1, pp. 51-83, Jan. 1978.